



Titre: Two-Way Fluid-Structure Coupling in Vibration and Damping Analysis
Title: of an Oscillating Hydrofoil

Auteur: Tahereh Liaghat
Author:

Date: 2014

Type: Mémoire ou thèse / Dissertation or Thesis

Référence: Liaghat, T. (2014). Two-Way Fluid-Structure Coupling in Vibration and Damping
Citation: Analysis of an Oscillating Hydrofoil [Mémoire de maîtrise, École Polytechnique de
Montréal]. PolyPublie. <https://publications.polymtl.ca/1410/>

 **Document en libre accès dans PolyPublie**
Open Access document in PolyPublie

URL de PolyPublie: <https://publications.polymtl.ca/1410/>
PolyPublie URL:

**Directeurs de
recherche:** François Guibault, & Jean-Yves Trépanier
Advisors:

Programme: Génie mécanique
Program:

UNIVERSITÉ DE MONTRÉAL

TWO-WAY FLUID-STRUCTURE COUPLING IN VIBRATION AND
DAMPING ANALYSIS OF AN OSCILLATING HYDROFOIL

TAHEREH LIAGHAT

DÉPARTEMENT DE GÉNIE MÉCANIQUE

ÉCOLE POLYTECHNIQUE DE MONTRÉAL

MÉMOIRE PRÉSENTÉ EN VUE DE L'OBTENTION
DU DIPLÔME DE MAÎTRISE ÈS SCIENCES APPLIQUÉES
(GÉNIE MÉCANIQUE))

AVRIL 2014

UNIVERSITÉ DE MONTRÉAL

ÉCOLE POLYTECHNIQUE DE MONTRÉAL

Ce mémoire intitulé :

**TWO-WAY FLUID-STRUCTURE COUPLING IN VIBRATION AND
DAMPING ANALYSIS OF AN OSCILLATING HYDROFOIL**

présenté par : LIAGHAT Tahereh

en vue de l'obtention du diplôme de : Maîtrise ès sciences appliquées

a été dûment accepté par le jury d'examen constitué de :

M. PELLETIER Dominique, Ph. D., président

M. GUIBAUT Francois, Ph. D., membre et directeur de recherche

M. TRÉPANIÉ Jean-Yves, Ph. D., membre et codirecteur de recherche

M. ÉTIENNE Stéphane, Doct., membre

ACKNOWLEDGE

The work put together in this dissertation would not have been possible but for the help, guidance, motivation, supports and faith bestowed by so many people. I would like to thank all the people who have contributed in some way in making this work possible. Without any one of them, the journey would not have been as memorable as it has been.

I would like to express my most sincere gratitude towards my advisor Professor Francois Guibault, whose guidance and supervision has been invaluable. This work was successfully completed thanks to his patience, enthusiasm and passion for science. He has not only been a great leader and supervisor but also a great philosopher, friend and guide. It has always been a great honor to be associated with Professor Guibault. I will remain forever indebted to him for everything that he has done for me.

I would like to thank my co-supervisor Professor Jean-Yves Trepanier for making it possible for me to pursue this research in Mechanical Engineering at Polytechnique and taking the time to review and comment my thesis.

I am also grateful to Bernd Nennemann for his insightful knowledge and keenness in my research work. It has been a wonderful opportunity to learn from him. His guidance was what has allowed me to do this work and understand some of the physics behind it.

I am grateful to my thesis committee Professor Dominique Pelletier and Dr. Stéphane Étienne for serving on my committee and providing valuable inputs and guidance in putting together this dissertation.

A lot of credit goes to all my colleagues from our group (ADOPT), who always helped me in every way they could, at every step. I would like to acknowledge with immense Christopher Devals, Hossein Hosseinimanesh, Salman Bahrami, Tran Tan-Dung and Lukas Allenbach. I would like to thank Christine Monette at ANDRITZ for providing her valuable comments. Last, but definitely not the least by any measure, I would like to acknowledge with deepest gratitude, support from my family. My parents have been a constant source of inspiration throughout my life. I am indebted to my husband, Farhang, who supported my research with his patience and of course for his extensive knowledge on the mechanical vibration. I would like to thank my daughter, Marzieh, for her love and understanding towards the completion of this research work.

RÉSUMÉ

Dès les premières phases de conception des composantes d'une turbine hydraulique, plusieurs facteurs, dont l'amortissement hydrodynamique et son influence sur la vibration des pales, doivent être estimés par les constructeurs afin d'évaluer le comportement dynamique des composantes. L'état de l'art actuel en la matière consiste à déterminer les caractéristiques dynamiques des aubes de turbine à l'aide de simulations numériques du fluide (simulations CFD) en régime stationnaire afin d'estimer le champ de pression induit par le fluide sur les aubes de la turbine. Ce champ de pression est ensuite appliqué en tant que condition limite ou de chargement sur l'aube afin de simuler son comportement mécanique par une méthode d'éléments finis. Une telle approche est appelée couplage unidirectionnel, car aucune déviation de l'aube n'est réinjectée dans la simulation CFD. Pour capturer l'influence de l'aube déformée sur le rendement hydraulique, la déformation doit être ramenée dans la simulation du fluide de telle sorte qu'une nouvelle solution CFD améliorée puisse être calculée et ainsi que la boucle d'interaction entre le comportement du fluide et de la structure puisse être fermée. Une telle boucle d'interaction bidirectionnelle entre les simulations du fluide et de la structure est appelée simulation couplée de l'interaction fluide-structure (ou FSI simulation, en anglais). C'est ce dernier type de simulation qui constitue l'objet du présent mémoire. Cette étude présente une validation des simulations numériques tridimensionnelles de l'interaction fluide-structure d'un profil hydraulique vibrant et examine la contribution de l'amortissement hydrodynamique du fluide à l'amortissement total. Nous utilisons une simulation de l'interaction fluide-structure basée sur deux solveurs distincts, l'un pour le fluide (ANSYS-CFX 13) et l'autre pour la structure (ANSYS Classic 13). Ces solveurs s'exécutent séquentiellement et échangent des informations à des points de synchronisation précis entre les étapes de simulation de chacun des domaines.

Dans un premier temps, afin de valider les étapes de base de l'approche de couplage bidirectionnelle pour la simulation de l'interaction fluide-structure, l'oscillation d'une plaque verticale dans une cavité remplie d'un fluide est examinée. Nous considérons également l'analyse transitoire d'une plaque sèche encastree à une extrémité afin d'évaluer l'effet de l'amortissement numérique sur les résultats de simulation. L'effet du choix du pas de temps et de la valeur d'amortissement visqueux sont également étudiés en détail.

Après validation de l'approche proposée, une attention particulière est accordée à l'évaluation de l'amortissement engendré par l'interaction fluide-structure dans des conditions réaliste d'écoulement fluide, grâce à l'application d'une modélisation bidirectionnelle de l'interaction.

Les capacités d'analyse de l'interaction fluide-structure bidirectionnelle disponible dans le logiciel commercial ANSYS sont utilisées pour prédire les amplitudes de vibration, pour déterminer l'amortissement hydrodynamique et pour évaluer l'importance d'effectuer une modélisation couplée pour un problème de vibration d'une aube dans l'eau. Comme nous observons dans notre analyse, l'amortissement hydrodynamique est influencé par de nombreux paramètres, tels que la distribution de la vitesse d'écoulement autour de l'aube. Pour comparer les résultats de ce travail de recherche avec ceux obtenus à partir de mesures expérimentales, la géométrie de l'aube a été choisie pour être semblable à un profil hydraulique utilisé dans une étude expérimentale effectuée par ANDRITZ. L'effet des maillages, du pas de temps et de la vitesse d'écoulement du fluide sont étudiés et les résultats numériques concordent bien avec les résultats expérimentaux.

ABSTRACT

Several factors in the design and analysis of hydropower structures, the identification of hydrodynamic damping and estimating its influences on the blade vibrations are crucial for constructors who try to assess the dynamics of runners in hydropower turbines at the earliest stage of the design phase. The current state-of-the-art approach to determine dynamic characteristics of the turbine blades consists of a steady state computational fluid dynamics (CFD) simulation which provides the fluid pressure on the turbine blade. This is then applied as a boundary or load condition for the finite element simulation of the configuration. Such an approach is called one-way coupled simulation since no deflection is fed back into CFD. To capture the influence of the deformed blade on the hydraulic performance, the deformation has to be brought back into the CFD solution such that an improved solution can be found and the loop can be closed. This comprises what is called two-way coupled fluid structure interaction (FSI) simulation or multi-field simulation, which is investigated in this thesis. This study presents a three-dimensional numerical fluid-structure interaction (FSI) modeling of a vibrating hydrofoil using the commercial software ANSYS-CFX and investigates the hydrodynamic damping as the fluid contribution to the total damping.

We use an FSI simulation with two separate solvers, one for the fluid (CFD) and one for the structure (FEM) that run in sequential order with synchronization points to exchange information at the interface of the fluid and structure domains. In the present work the two commercially available solvers ANSYS CFX 13.0 and ANSYS Classic 13.0 are applied as CFD and FEM solver respectively. Different meshes were generated in this analysis for the fluid and solid fields.

As the first step and to show the basic steps in fluid-structure interaction analysis with ANSYS-CFX and to validate the above mentioned two-way FSI approach, oscillation of a vertical plate in a cavity filled with a fluid is considered. We also consider the transient analysis of the plate with cantilever support in dry-condition to investigate the effect of considering numerical damping in the analysis. The effects of time step and viscous damping were also studied in details.

After validating the proposed approach, special attention is paid to damping due to FSI in realistic flowing water conditions through the systematic application of a two-way fluid-structure interaction modeling. The capability of the two-way FSI analysis available in the

commercial software ANSYS is used to predict the amplitudes of vibration, to identify the hydrodynamic damping and to estimate the influence of including FSI in the analysis of the problem. As we observe in our analysis, the identification of blade hydrodynamic damping is influenced by many different parameters, such as the flow velocity distribution around the blade. To compare the results of this research work with those obtained from the experimental observations and estimations under realistic flowing conditions, the geometry of the blade was selected to be similar to the hydrofoil blade used in the experimental investigation done by ANDRITZ. The effects of considering different flow velocities are also investigated.

TABLE OF CONTENTS

ACKNOWLEDGE	iii
RÉSUMÉ	iv
ABSTRACT.....	vi
TABLE OF CONTENTS.....	viii
LIST OF TABLES	x
LIST OF FIGURES	xi
LIST OF APPENDIX	xv
LIST OF SYMBOLS AND ABBREVIATIONS	xvi
CHAPTER 1 INTRODUCTION	1
1.1. Motivation.....	1
1.2. Literature review	2
1.3. The goal of the present study	6
CHAPTER 2 THEORETICAL BACKGROUND.....	8
2.1. Classification of Flow-induced Vibration.....	8
2.2. Fluid Domain	10
2.2.1. Continuity equation.....	10
2.2.2. Equation of motion or Momentum equation.....	11
2.3. Turbulence Model.....	12
2.3.1. Reynolds Averaged Navier-Stokes (RANS) Equations.....	13
2.4. Structural Domain.....	15
2.4.2. Dynamic structural analysis	16
2.5. Damping in mechanical dynamic systems	17
2.5.1. Types of Damping.....	18
2.5.2. Damping Measurement	20
CHAPTER 3 FSI MODELING WITH ANSYS.....	27
3.1. One-Way and Two-Way FSI	27
3.1.1. One-Way FSI	29
3.1.2. Two-Way FSI.....	29

3.2. Modeling procedure	30
3.2.1. Methods available for transient dynamic analysis in ANSYS	31
3.2.2. Forms of Damping in ANSYS	33
CHAPTER 4 VALIDATION	37
4.1. Oscillating Plate	37
4.1.1. Effect of dynamic viscosity.....	41
4.1.2. Effect of numerical damping.....	43
CHAPTER 5 HYDROFOIL BLADE.....	49
5.1. Modal Analysis of Blade without Fluid.....	51
5.2. Transient Analysis of Blade without Fluid	54
5.2.1. Influence of mesh.....	54
5.2.2. Influence of Force Application	58
5.2.3. Influence of Force Position	63
5.2.4. Time-step study.....	65
5.3. Transient Analysis of Blade with Fluid (FSI).....	69
5.3.1. Flow-induced vibration and influence of considering two-way FSI modeling.....	70
5.3.2. Influence of Force Application	72
5.3.3. Influence of mesh.....	78
5.3.4. Influence of time step.....	85
5.3.5. Influence of velocity	89
CHAPTER 6 CONCLUSIONS	94
REFERENCES	96
APPENDIX.....	99

LIST OF TABLES

Table 2-1 The transport equations for the standard k- ϵ model	15
Table 4-1 Parameters to investigate the effects of numerical damping and time step (Dry-condition)	46
Table 5-1 Scaled geometries and predicted natural frequencies of the hydrofoils	51
Table 5-2 Finite element modeling of the blade	52
Table 5-3 Natural frequencies of the blade (Hz) in dry-condition.....	53
Table 5-4 Different forcing functions for transient analysis of the hydrofoil blade	54
Table 5-5 Influence of mesh	55
Table 5-6 Step Force with different time durations (t_f).....	59
Table 5-7 Dominant frequencies and maximum amplitude of blade vibrations	66
Table 5-8 Three types of forces	72
Table 5-9 Step Force with different time durations (t_f) for blade in water.....	73
Table 5-10 Three different fluid meshes (V=6 m/s, dt=0.0004)	80
Table 5-11 Differences between M-Mesh and F-Mesh (V=6 m/s).....	84
Table 5-12 Three different time step (V=6 m/s)	86
Table 5-13 CPU time (h) when 4 parallel CPU are working together	88

LIST OF FIGURES

Fig. 2-1 Trailing edge vortex shedding (Reese, 2010).....	9
Fig. 2-2 The relationship between total loss factor and free-stream velocity (Reese, 2010)...	10
Fig. 2-3 Differential control volume conservation of mass	10
Fig. 2-4 Hysteresis loop for elastic materials.....	18
Fig. 2-5 Impulse response of a simple oscillator	21
Fig. 2-6. A typical step response of a simple oscillator	23
Fig. 2-7. The magnification factor method applied to a single-degree-of-freedom system ...	24
Fig. 2-8. Magnification factor method applied to a multi-degree-of-freedom system	25
Fig. 3-1 Flowchart for multi-field simulations with ANSYS	28
Fig. 3-2 Sequence of Synchronization Points (Reference ANSYS)	30
Fig. 3-3 Fluid boundary conditions.....	33
Fig. 3-4 Rayleigh Damping.....	36
Fig. 4-1 Geometry of oscillating plate (not drawn to scale)	37
Fig. 4-2 The computational mesh	38
Fig. 4-3 Horizontal displacement of the free end of the plate for different time steps and $\mu=0.2$ (ND=0.1).....	39
Fig. 4-4 Comparison of the displacements of the free end of the plate for $\mu=0.2$;	39
Fig. 4-5 Horizontal displacements of the free end of the plate for different time steps and $\mu=1$ (ND=0.1).....	40
Fig. 4-6 Comparison of the displacements of the free end of the plate for $\mu=1$;	40
Fig. 4-7 Horizontal displacements of the free end of the plate for time step $dt=0.01$ and $\mu=5$ (ND=0.1).....	40
Fig. 4-8 Comparison of the displacements of the free end of the plate for $\mu=5$;	41
Fig. 4-9 Horizontal displacement of the free end of the plate for different fluid viscosities ($dt=0.01$)	42
Fig. 4-10 Horizontal displacement of the free end of the plate for different fluid viscosities, —○— $\mu=0.2$; —□— $\mu=1$; — $\mu=5$ [Namkoong et al.(2005)]	42
Fig. 4-11 Damping ratio (ξ) calculated for different fluid viscosities ($dt=0.01$).....	42
Fig. 4-12 Damping ratio calculated for different fluid viscosities,.....	43
Fig. 4-13 Horizontal displacements of the free end of the plate for $dt=0.1$ & ND=0.01 & $\mu=0.2$	44
Fig. 4-14 Horizontal displacements of the free end of the plate for different dt and ND (with $\mu=0$).....	44

Fig. 4-15 Geometry of cantilever beam (Example 2)	46
Fig. 4-16 The variations of the displacements of the free end of the cantilever beam for the first few time steps	48
Fig. 4-17 The variations of the displacements of the free end of the cantilever beam for	48
Fig. 5-1 A schematic diagram of the computational domain.....	50
Fig. 5-2 Schematic of the H1 hydrofoil	51
Fig. 5-3 SOLID185 element	52
Fig. 5-4 First Mode (218.61 Hz).....	53
Fig. 5-5 Second Mode (289.54 Hz).....	53
Fig. 5-6 Third Mode (619.68 Hz)	54
Fig. 5-7 Blade computational mesh (C-mesh)	55
Fig. 5-8 z -displacement at midpoint of the trailing edge of blade (C-mesh, $dt=0.0001$ s)	56
Fig. 5-9 Blade computational mesh (M-mesh)	56
Fig. 5-10 z -displacement at midpoint of the trailing edge of blade (M-mesh, $dt=0.0001$ s) ..	56
Fig. 5-11 Blade computational mesh (F-mesh).....	56
Fig. 5-12 z -displacement at midpoint of the trailing edge of blade (F-mesh, $dt=0.0001$ s)....	56
Fig. 5-13 Blade computational mesh (VF-mesh).....	57
Fig. 5-14 z -displacement at midpoint of the trailing edge of the blade (VF-mesh, $dt=0.0001$ s).....	57
Fig. 5-15 (a) z -displacement at midpoint of the blade trailing edge (For different mesh sizes, $dt=0.0001$ s), (b) Before removing load, (c) After removing load	58
Fig. 5-16. z -displacement at midpoint of the trailing edge of the blade for different tf	60
Fig. 5-17 (a) z -displacement at midpoint of the trailing edge of the blade (b) FFT of the system response	62
Fig. 5-18 (a) z -displacement at midpoint of the trailing edge of the blade (b) FFT of the system response	63
Fig. 5-19 (a) z -displacement at midpoint of the trailing edge of the blade ($F_T=60$ N, $F_L=0$ N)	63
Fig. 5-20 (a) z -displacement at midpoint of the trailing edge of the blade ($F_T=30$ N, $F_L=-30$ N) (b) FFT of the system response.....	64
Fig. 5-21 (a) z -displacement at midpoint of the trailing edge of the blade ($F_T=15$ N, $F_L=-30$ N) (b) FFT of the system response.....	64
Fig. 5-22 (a) z -displacement at midpoint of the trailing edge of the blade ($F_T=0$ N , $F_L=-60$ N) (b) FFT of the system response.....	65

Fig. 5-23 z -displacement of the midpoint of the thin part of the blade M-Mesh , $dt=0.001$ s (5 time steps per oscillation period).....	66
Fig. 5-24 z -displacement at midpoint of the trailing edge of the blade M-Mesh , $dt=0.0004$ s (12 time steps per oscillation period).....	66
Fig. 5-25 z -displacement at midpoint of the trailing edge of the blade M-Mesh , $dt=0.0001$ s (46 time steps per oscillation period).....	67
Fig. 5-26 z -displacement at midpoint of the trailing edge of the blade M-Mesh , $dt=0.00004$ s (114 time steps per oscillation period).....	67
Fig. 5-27 z -displacement at midpoint of the trailing edge of the blade M-Mesh , $dt=0.00003$ s (153 time steps per oscillation period).....	67
Fig. 5-28 z -displacement at midpoint of the trailing edge of the blade (For different time steps)	68
Fig. 5-29 FFT of the system response (a) $dt=0.0001$ s (b) $dt=0.00003$ s.....	69
Fig. 5-30 Fluid forces on the hydrofoil blade	71
Fig. 5-31 Normalized force on the blade	72
Fig. 5-32 Velocity contour at the trailing edge of the blade	72
Fig. 5-33 z -displacement at midpoint of the trailing edge of the blade for different tf	74
Fig. 5-34 (a) z -displacement at midpoint of the trailing edge of the blade (b) FFT of the system response.	76
Fig. 5-35 (a) z -displacement at midpoint of the trailing edge of the blade (b) FFT of the system response for $tf = 0.012$ sec	77
Fig. 5-36 $F_T=15$ N , $F_L=-30$ N (a) z -displacement at midpoint of the trailing edge of the blade (b)&(d) FFT of the system response (c) z -displacement at midpoint of the leading edge of the blade.....	78
Fig. 5-37 Different Fluid Meshes (a) C-mesh (b) M-mesh (c) F-mesh	79
Fig. 5-38 z -displacement at midpoint of the blade trailing edge (For different mesh sizes, $dt=0.0004$ s, $V=6$ m/s)	80
Fig. 5-39 Comparison of damping ratio for different velocities and different mesh sizes with the experiment results ($dt=0.0004$ s).....	81
Fig. 5-40 z -displacement at midpoint of the blade trailing edge (For C-mesh and M-mesh, $dt=0.0002$ s, $V=6$ m/s)	81
Fig. 5-41 z -displacement at midpoint of the blade trailing edge (For C-mesh, $dt=0.0001$ s, $V=6$ m/s)	82

Fig. 5-42 z -displacement at midpoint of the blade trailing edge (For M-mesh and F-mesh, $dt=0.0002$ s, $V=6$ m/s)	82
Fig. 5-43(a) z -displacement at midpoint of the trailing edge of the blade (b) FFT of the system response. (For F-mesh, $dt=0.0001$ s, $V=6$ m/s)	83
Fig. 5-44 Z -displacement at midpoint of the blade trailing edge (For M-mesh and F-mesh, $dt=0.0002$ ss, $V=9$ m/s).....	85
Fig. 5-45 z -displacement at midpoint of the blade trailing edge (M-mesh, different time steps, $V=6$ m/s)	86
Fig. 5-46 z -displacement at midpoint of the blade trailing edge (For M-mesh, different time step, $V=12$ m/s).....	87
Fig. 5-47 Deformations of the half of blade for $V=12$ m/s , $dt=0.0002$ s at (a) $t=0.03$ s (b) $t=0.06$ s.....	87
Fig. 5-48 z -displacement at midpoint of the blade trailing edge (For different fluid velocities, $dt=0.0002$ s)	90
Fig. 5-49 Maximum amplitude of blade oscillation for different fluid velocities	90
Fig. 5-50 Natural frequency of blade for different fluid velocities.....	90
Fig. 5-51 Damping ratio of the blade (ξ) for different fluid velocities ranging from 0 to 25 m/s. The experimental results are taken from (Seeley et al., 2012).....	91
Fig. 5-52 Damping ratio of the blade (ξ) for fluid velocities ranging from 0 to 7.5 m/s. The experimental results are taken from (Seeley et al., 2012).....	91
Fig. A-1 (a) z -displacement at midpoint of the trailing edge of the blade (b) FFT of the system response for $tf = 1 \times 10^{-3}$ sec	100
Fig. A-2 ANSYS interface loads	100
Fig. A-3(a) z -displacement at midpoint of the trailing edge of the blade (b) FFT of the system response for $tf = 1 \times 10^{-3}$ sec	100

LIST OF APPENDIX

APPENDIX A: Notes on using ANSYS for FSI analysis	99
---	----

LIST OF SYMBOLS AND ABBREVIATIONS

Latin characters

<u>Symbol</u>	<u>Description</u>	<u>Units</u>
E	Young's modulus	Gpa
f	Frequency	Hz
t	Time	s
dt	Time step	s
w	Displacement	mm
V	Velocity	m/s
u, v, w	Velocity component at x, y, z direction	m/s
p	Pressure	Pa
F	Force	N
a	Acceleration	m/s^2
B	Body force	N
x, y, z	Positions	m
T	Period	s

Greek symbols

<u>Symbol</u>	<u>Description</u>	<u>Units</u>
ξ	Damping ratio	
ν	Poisson ration	
ρ	Density	kg/m^3
μ	Fluid dynamic viscosity	Pa s
σ	stress	Pa
ω	Angular velocity	Rad/s
δ	Logarithmic decrement	
γ	Strain tensor	
δ_{ij}	Kronecker delta	
$\bar{\lambda}, \bar{\mu}$	Lame constants	

Subscript

<u>Symbol</u>	<u>Description</u>
n	Natural
shed	shedding
t	turbulent
s	solid
i, j, k	components
FSI	Fluid-Solid interaction

Abbreviations

<u>Symbol</u>	<u>Description</u>
FSI	Fluid-Structure Interaction
EIE	Extraneously Induced Excitation
IIE	Instability Induced Excitation
MIE	Movement Induced Excitation
CFD	Computational Fluid Dynamics
RANS	Reynolds Averaged Navier-Stokes
URANS	Unsteady Reynolds Averaged Navier-Stokes
DES	Detached-Eddy Simulation
DNS	Direct Numerical Simulation

CHAPTER 1 INTRODUCTION

1.1. Motivation

Fluid-structure interaction (FSI) and unavoidable blade vibration are important characteristics in the operation of hydropower structures and must be taken into account in the analysis and design of such equipment. Among several parameters in the fluid-structure interaction analysis of hydrofoil blades, considering the damping effect of the flowing water and its interaction with the vibration amplitude of the blade is of great interest. This effect is called the hydrodynamic damping effect and is known as the fluid contribution to the total damping of an immersed vibrating structure which also includes structural and material damping. It should be noted that the vibration amplitudes are inversely related to the damping from the structural components and fluid effects and it is therefore critical to investigate the additional damping due to FSI during the design phase to accurately estimate vibration amplitudes and to avoid costly problems later while in service (Seeley et al., 2012). The effects of damping due to FSI for cables and pipes have been investigated by (Naudascher and Rockwell, 1980). However to the best of the author's knowledge, few efforts have been targeted towards damping effects in hydraulic turbine blade applications (Reese, 2010). Recently, an experimental investigation of damping due to FSI has been presented by Seeley et al. (2012). They used three hydrofoils to investigate damping due to FSI. The excitation to the hydrofoil test structures was provided by using piezoelectric actuation with macro-fiber composites (MFCs). Natural frequency and damping estimates were experimentally obtained from sine sweep frequency response functions measured with a laser vibro-meter through a window in the test section. The results indicated that, although the natural frequencies were not substantially affected by the flow, the damping ratios increased linearly with respect to flow velocity.

This study presents a three-dimensional numerical fluid-structure interaction (FSI) modeling of a vibrating hydrofoil (as presented by Seeley et al. (2012)) using the commercial software ANSYS-CFX and investigates the hydrodynamic damping as the fluid contribution to the total damping.

1.2. Literature review

Blade vibration problems are of interest to the structural, hydrodynamic and acoustic engineers. Vibration is almost always undesirable in these applications. As a first example, the hydrodynamic solution is affected by the periodic motion of the blade cross-section which produces unsteadiness and causes time-dependent lift and drag forces to oscillate about the steady-state values. This oscillation can lead to flutter if not carefully controlled. From the structural point of view, these forces can fatigue the blade structure and reduce its operational performance. The structural vibration also causes acoustic wave propagation in the fluid medium. These acoustic waves can cause structural damage when having enough energy. A rotor–stator interaction in hydraulic machinery can also be considered as a second example of blade vibration. The interaction between rotor and stator in this application will induce pressure fluctuations, which can lead to vibrations of the guide vane or resonance in the distributor channels (Lee et al., 2010; Saeed et al., 2010; Thapa et al., 2012; Wang et al., 2009). The flow-induced vibrations of the guide vane, excited by von Karman vortex shedding can also lead to premature cracks (Münch et al., 2010). Thus, there is strong interest to study the elastic behavior of vibrating blades to design safe and reliable turbines and pump-turbines (Wang et al., 2009). On the other hand and from both theoretical and practical point of view, complex interaction between flowing water and structure known as fluid–structure interaction (FSI) must be taken into account in performing dynamic analysis and studying the flow induced vibration of such structures. Fluid-structure interaction is a wide term spanning multiple engineering disciplines and it plays a significant role in many engineering applications (Esmailzadeh et al., 2008). It generally denotes the bi-directional energy transfer in a domain consisting of both solid and fluid.

One-way and two-way fluid-structure interaction modeling: Problems involving the interaction between fluids and structures can be modeled as uncoupled problems within their separate domains. In these un-coupled problems it is assumed that one domain is driven by the other, with the driven domain having no feedback effect on the driving domain. This results in what is called, one-way fluid structure interaction. For instance, the acoustic excitation of air being driven by a speaker can be modeled without considering the feedback effects of the driven air on the structural deflection of the loud speaker surface. That is therefore an example of a classical FSI problem where the coupling effect of the interaction between the fluid and

structural domains only needs to be taken into account in one direction, namely the effect of the structure on the fluid. Another example for one way fluid-structure interaction problem is the dynamic wind loading on many civil structures in which the fluid is the driving domain and the structure is being driven and the structural part has little feedback effect on the fluid domain. In such problems, the motion and displacement of the structure have no considerable effect on the wind loads which drive this motion and the structure can be analyzed separately, or uncoupled from the wind under the given loads of interest. This, however, is not always the case for some practical engineering applications in which the structural displacements caused by the fluid motion further enhance the fluid forces in such a way that the fluid and the structure are interacting in a feedback system. In such cases, two-way FSI analysis needs to be undertaken. This is often the case in situations where the amplitude of the structural deflection is large.

Analytical modeling of complex structures has limited scope, so numerical analysis is often required. The need for numerical solutions to most complex engineering problems has driven the development and wide application of Finite Element Method (FEM) and Computational Fluid Dynamics (CFD) numerical simulations in the structural and fluid domains respectively. One way to numerically model coupled FSI problems is to couple these two computational domains together with independent solvers for each domain, passing boundary conditions from each domain to the other at each computational step (Wang et al., 2009).

Although two-way fluid structure coupling is starting to be more widely available in commercial CFD/FEA packages, it still has not reached a level of integration and computational efficiency that enables it to be used for the analysis of complex structure and flow interactions without significant computational and time expense.

Reese (2010) presented an experimental assessment of two-dimensional theories and trends concerning hydro-elastic response of a cantilever hydrofoil in uniform flow. An aluminum NACA 66 hydrofoil with geometry similar to those found on sea-surface and an undersea vehicle was used to determine modal parameters under the conditions of both flow-induced and mechanical vibrations. The extraction of damping factors for in-air structural, fluid-loaded and uniform flow cases were also performed in his analysis. Hydrodynamic damping factors were compared with theory and it was shown to agree well for bending modes, but not as well for torsional modes. They concluded that further refinement to the torsional mode hydrodynamic

damping factor, added mass and hydrodynamic resistance theory for 3-dimensional mode shapes were required because the two-dimensional theory overestimates the damping factor.

Noting that the fluid-structure investigations in hydraulic machines using coupled simulations are particularly time-consuming, an alternative method has been presented by Münch et al. (2010) that linearizes the hydrodynamic load of a rigid, oscillating hydrofoil. The hydrofoil was surrounded by incompressible, turbulent flow and was modeled with forced and free pitching motions. Unsteady simulations of the flow, performed with ANSYS CFX, were also presented and validated with experiments which were carried out in the High-Speed Cavitation Tunnel (in Laboratory for Hydraulic Machines, Ecole Polytechnique Federale de Lausanne, Switzerland). The hydrodynamic load was linearized by combining the added moment of inertia, fluid damping and fluid stiffness effects. As expected, the potential flow analysis showed that the added moment of inertia is constant, while the fluid damping and the fluid stiffness coefficients depend on the reduced frequency of the oscillation motion.

To gain a better insight on the practical application of the research on blade vibration and fluid-structure interaction problems, a short literature review on its application in design and analysis of water turbines must also be presented. Water turbines, such as Francis turbines, convert the potential and kinetic energies of water into mechanical shaft rotation to turn generators. It is well known that the motion of the water also creates excitation forces that may result in unavoidable blade vibration and changes in the dynamic response of the turbine due to mass loading, stiffness and damping effects. Ignoring this complex interaction between the flowing water and the structure, may lead to premature failure of the turbine (Coutu et al., 2005; Coutu et al., 2007; Coutu et al., 2004; Seeley et al., 2012). Moreover, it is very difficult to rectify such vibrations after the turbine installation and the need for non-contact measuring techniques is apparent due to the high operating pressures and the rotating environment within a turbine. Although there has been extensive investigation of fluid-structure interaction and/or aero-elastic effects in aeronautical applications, such as gas turbine blades, helicopter rotors, wind turbine blades and aero-plane wings, limited investigation of these effects have been conducted for low aspect ratio hydrofoils and marine propellers (Hutchison, 2012).

It is well known that the hydraulic excitation forces on the turbine runners produce high vibration levels that can cause fatigue damage (Thapa et al., 2012). To avoid this situation it is

necessary to undertake an exhaustive analysis of the dynamic behavior of the runner. This analysis has to include the characteristics of the excitation forces and of the runner response to avoid resonances. The runner response can be estimated using the finite element method. Dubas and Schuch (Dubas and Schuch, 1987) used the commercial software ANSYS, with a model based on iso-parametric shell elements to calculate the natural frequencies and mode shapes of a Francis runner without considering water effects. It should be noted that several uncertainties exist when implementing the model due to its complex geometry and boundary constraints. Moreover, the runner is submerged in water and the effect of the added mass and fluid structure interaction (FSI) on the runner response can be important. The quantification of this effect is one of the main doubts when determining the runner response.

Tanaka (Tanaka, 1990) presented a frequency reduction ratio of only one mode measured on both prototype and model runner and showed that the natural frequency will be reduced in water due to the added mass effect and introduced an empirical value 0.2 for the frequency reduction ratio. Du and He et al. (Du et al., 1998) developed a method to consider the water effect on the turbine runner by importing the added mass into the structural dynamic theory. They did a simulation with the mesh including both fluid and structure, and showed some mode shapes and corresponding frequencies. In addition, they calculated the frequency reduction ratio and indicated that the added mass effect depends on the mode shapes of the runner. The influence of still water on the modal characteristics of a reduced scale model of a Francis turbine has been experimentally investigated by Rodriguez et al. (Rodriguez et al., 2006).

The quantitative importance of runner blade-guide vane interactions, also called Rotor-Stator Interactions (RSI) on the dynamic behavior of Francis turbines has also been demonstrated recently (Coutu et al., 2004). All runners in operation are excited by RSI. Although this excitation is usually very small and does not affect the behavior or damage the runner, Andre Coutu et al. (Coutu, 2005) reported on the RSI phenomenon that took place in the Ste-Marguerite 3 (SM-3) runner. In this case, the phenomenon was so strong, that it made the runner crack at an accelerated pace. It has been reported that after a few days of generation at peak efficiency, noticeable noise was heard from the unit 1 of Ste-Marguerite 3 (SM3) in April 2003. The machine was stopped for inspection after 200 hours and major cracks at the blade outflow edge junctions with crown and band were discovered on many blades. Some of the

analyses/calculations/testing performed to identify the root cause of the problem as well as the solution that was implemented are reported in (Coutu et al., 2005; Coutu et al., 2007; Monette et al., 2007).

Dompierre and Sabourin (Dompierre and Sabourin, 2010) considered the fluid-structure interaction modeling in dynamic analysis of a Francis turbine runner under normal operating condition. Their primary interest was the structural vibration in the vicinity of resonance. For this reason, they calculated the damping factor implicitly with no validation on the prediction of damping. More recently, Seeley et al. (2012) presented an experimental effort, started in 2004, to characterize the damping of blade-like structures due to fluid–structure interaction. They used Macro-fiber composite (MFC) piezoelectric actuators bonded to a plate contoured with a hydraulic profile. The plate was placed in a test section, subjected to water with increasing velocities, and excited with sine sweeps using the MFCs. The natural frequencies and damping coefficient were determined from the experimental frequency response functions for a range of water velocities. Results were presented to relate the damping coefficient to the water velocity. The results indicated that, although the natural frequencies were not substantially affected by the flow, the damping ratios were observed to increase in a linear manner with respect to flow velocity.

1.3. The goal of the present study

This research presents an investigation of the hydroelastic behavior of vibrating blades in hydraulic machines, which is of strong interest for turbo machinery applications. Despite numerous industrial applications, very few studies have been devoted to the case of a hydrofoil. In particular, damping due to FSI for hydraulic blades in realistic flowing water conditions has not received much attention. The hydrodynamic damping influences the amplitude of vibrations and is directly related to fatigue problems in hydraulic machines which are of great importance in their design procedure. Therefore, the identification of hydrodynamic damping is crucial for constructors who try to assess the dynamics of runners in hydropower turbines at the earliest stage of the design phase. The aim of this research is to investigate the coupled effects of flowing fluid and a simplified hydrofoil blade by using a two-way fluid-structure interaction modeling of hydrofoil blade and its importance in predicting vibration amplitudes. Special attention will be paid to damping due to fluid–structure interaction in realistic flowing water conditions through

the systematic application of a two-way fluid-structure interaction modeling. The effects of considering different flow velocities will also be investigated in the present study. The capability of the two-way fluid-structure interaction analysis available in the commercial software ANSYS will be used to predict the amplitudes of vibration. The geometry of the blade is selected to be similar with the hydrofoil blade used in the experimental investigation reported in (Seeley et al., 2012). For the test cases, an initial force is applied on the structure to excite the blade in the fluid at the first bending mode. After removing the applied force, the analysis of displacement of a point attached to the structure whose amplitude is significant allows us to extract the natural frequencies of the modes involved in the resulting free vibration. The damping coefficient of the blade can also be estimated from the damped free vibration curve using either the logarithmic decrement method or a least square curve fit. The results of the present numerical investigation will also be compared with the experimental results given by Seeley et al. (2012).

CHAPTER 2 THEORETICAL BACKGROUND

This chapter reviews the fundamental concepts of fluid and solid mechanics as a necessary background for the fluid-structure vibration analysis of hydrofoil blades. It includes a brief theoretical description of (i) classification of flow-induced vibrations, (ii) governing equations for the fluid domain, (iii) different turbulent models, (iv) governing equations for the structural domain, (v) basic equations for transient structural dynamics and (vi) different types of damping in mechanical systems. A fluid is a substance that will deform continuously under the action of applied surface (shearing) stresses. The magnitude of the stress in the fluid depends on the *rate of angular deformation*. On the other hand, a solid can be defined as a substance that will deform by an amount proportional to the stress applied after which static equilibrium will result. The magnitude of the shear stress in solids depends on the magnitude of *angular deformation*. The governing equations for the solid and fluid can be derived starting with particle kinematics and deformation measures and by using three fundamental laws of physics (i.e., conservation of mass, conservation of linear momentum and conservation of energy). These laws must always be fulfilled and are not restricted to any particular material.

2.1. Classification of Flow-induced Vibration

Among different classifications of flow-induced vibrations, a very systematic and logical classification has been proposed in terms of the sources of excitation of flow-induced vibration, namely, (i) extraneously induced excitation (EIE), (ii) instability-induced excitation (IIE), and (iii) movement-induced excitation (MIE). Extraneously induced excitation (EIE) is defined as being caused by fluctuations in the flow or pressure, independently of any flow instability and any structural motion. An example is the turbulence-induced excitation of a cylinder in flow due to pressure fluctuations associated with turbulence in the flow. Instability-induced excitation (IIE) is associated with flow instability and involves local flow oscillations. An example for IIE can be reviewed as flows from the top and bottom of an airfoil blade re-converge at the trailing edge (Fig. 2-1). In this case, the boundary layers shed alternately from the blade with a shedding frequency (f). Shedding frequency is related to the speed at which vortices are convected from the trailing edge and the separation distance between vortices. The change in momentum due to shed fluid vortices imparts a force in the cross-flow direction along the trailing edge of the blade. The extreme case of shedding frequency excitation occurs when the

shedding frequency aligns with a natural frequency of the structure. This condition is known as “lock-in”. Some known key points of the shedding frequency excitation in relation to damping are as follows,

- When the shedding frequency is below the natural frequency of a mode ($f_{\text{shed}} < f_n$), the mode is excited a moderate amount and damped only by mechanical and sound radiation mechanisms.
- When the shedding frequency is very close to the natural frequency ($f_{\text{shed}} \approx f_n$), lock-in can occur and the mode is excited strongly with very little damping. The peak response at the resonance frequency jumps upward because of the loss of damping.
- When the shedding frequency is above the natural frequency ($f_{\text{shed}} > f_n$), the mode is weakly excited and is highly damped by additional hydrodynamic damping which increases with increasing flow velocity.

The relationship between total loss factor (η_T) and the free stream velocity (V_∞) is shown in Fig. 2-2. It can be seen from this figure that the total damping drops significantly at lock-in.

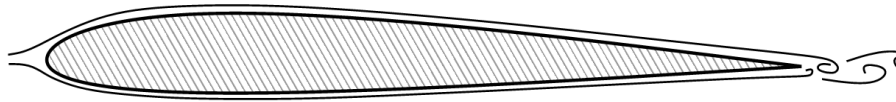


Fig. 2-1 Trailing edge vortex shedding (Reese, 2010)

Finally, in movement-induced excitation (MIE) the fluctuating forces arise from movements of the body; hence, the vibrations are self-excited. Flutter of an aircraft wing and of a cantilevered pipe conveying fluid are examples of this type of excitation. Clearly, certain elements of IIE with fluid elastic feedback and MIE are shared; however, what distinguishes MIE is that in the absence of motion there is no oscillatory excitation whatsoever.

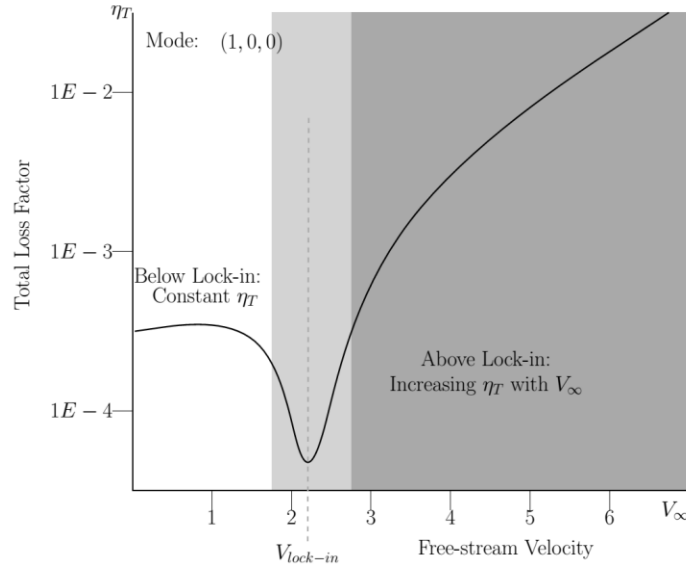


Fig. 2-2 The relationship between total loss factor and free-stream velocity (Reese, 2010)

2.2. Fluid Domain

The derivation of the governing equations for the fluid domain needs using the continuity equation, equation of motion or momentum equation and the energy equation.

2.2.1. Continuity equation

The continuity equation is derived by using a differential control volume of size ($dx dy dz$) as shown in Fig. 2-3 From the principle of conservation of matter, the sum of the flux of mass for the three directions x , y , and z , must be equal to the time rate of change of mass $\frac{\partial}{\partial t}(\rho dx dy dz)$.

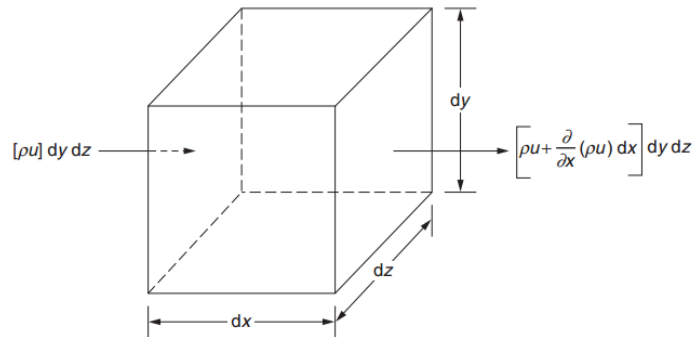


Fig. 2-3 Differential control volume conservation of mass

Nothing that the control volume is independent of time, the continuity equation is obtained as

$$\frac{\partial \rho}{\partial t} + \frac{\partial}{\partial x}(\rho u) + \frac{\partial}{\partial y}(\rho v) + \frac{\partial}{\partial z}(\rho w) = 0 \quad (2-1)$$

where ρ is the mass density, t is time and u , v , and w are the x , y , and z components of velocity, respectively. By using the vector notation,

$$\vec{V} = u\vec{i} + v\vec{j} + w\vec{k} = \text{velocity vector}$$

and

$$\vec{\nabla} = \frac{\partial}{\partial x}\vec{i} + \frac{\partial}{\partial y}\vec{j} + \frac{\partial}{\partial z}\vec{k} = \text{gradient vector}$$

the continuity equation can be written as

$$\frac{\partial \rho}{\partial t} + \vec{\nabla} \cdot \rho \vec{V} = 0 \quad (2-2)$$

This equation can also be written as

$$\frac{\partial u}{\partial x} + \frac{\partial v}{\partial y} + \frac{\partial w}{\partial z} = -\frac{1}{\rho} \frac{D(\rho)}{Dt} \quad (2-3)$$

where (D/Dt) represents the total or substantial derivative with respect to time. Equations (2.1, 2.2 and 2.3) represent the general three-dimensional continuity equation for a fluid in unsteady flow. If the fluid is incompressible, the time rate of volume expansion of a fluid element will be zero and the continuity equation, for both steady and unsteady flows, becomes

$$\vec{\nabla} \cdot \vec{V} = \frac{\partial u}{\partial x} + \frac{\partial v}{\partial y} + \frac{\partial w}{\partial z} = 0 \quad (2-4)$$

2.2.2. Equation of motion or Momentum equation

The state of stress in a fluid is characterized, as in the case of a solid, by the six stress components σ_{xx} , σ_{yy} , σ_{zz} , σ_{xy} , σ_{yz} , and σ_{zx} . However, if the fluid is at rest, the shear stress components σ_{xy} , σ_{yz} , and σ_{zx} will be zero and all the normal stress components will be the same and equal to the negative of the hydrostatic pressure, p that is, $\sigma_{xx} = \sigma_{yy} = \sigma_{zz} = -p$. The relations between stress and the rate of strain for a Newtonian fluid can be obtained as (Rao, 2011)

$$\sigma_{ij} = -P\delta_{ij} + 2\mu(D_{ij} - \frac{1}{3}D_{kk}\delta_{ij}) \quad (2-5)$$

$$D_{ij} = \frac{\partial v_i}{\partial x_j} + \frac{\partial v_j}{\partial x_i} \quad (2-6)$$

The equation of motion can now be derived by applying Newton's second law to a differential volume ($dx dy dz$) of a fixed mass m . If the body forces acting on the fluid per unit mass are given by the vector

$$\vec{B} = B_x \vec{i} + B_y \vec{j} + B_z \vec{k} \quad (2-7)$$

the application of Newton's law in x direction gives

$$\vec{\nabla} \cdot \vec{F} = m\vec{a} \quad (2-8)$$

where $\vec{\nabla} \cdot \vec{F}$ and \vec{a} are the differential force and acceleration, respectively. Dividing this equation by the volume of the element give the following equations of motions

$$\rho \vec{B} + \vec{\nabla} \cdot \vec{\sigma} = \rho \vec{a} \quad (2-9)$$

The above equations are applicable to any fluid with gravitational-type body forces. For Newtonian fluids with a single viscosity coefficient, these equations can be simplified to

$$\underbrace{\rho \vec{a}}_{\text{Inertia force}} = \rho \left(\frac{\partial \vec{V}}{\partial t} + \vec{V} \cdot \vec{\nabla} \vec{V} \right) = \underbrace{\rho \vec{B}}_{\text{Body force}} - \underbrace{\vec{\nabla} P}_{\text{Pressure force}} + \underbrace{\mu \vec{\nabla}^2 \vec{V} + \frac{\mu}{3} \vec{\nabla} (\vec{\nabla} \cdot \vec{V})}_{\text{Viscous force}} \quad (2-10)$$

These equations are the Navier-Stokes equations for compressible Newtonian fluids. For incompressible fluids, the Navier-Stokes equations of motion become

$$\vec{a} = \frac{\partial \vec{V}}{\partial t} + \vec{V} \cdot \vec{\nabla} \vec{V} = \vec{B} - \frac{\vec{\nabla} P}{\rho} + \frac{\mu}{\rho} \vec{\nabla}^2 \vec{V} \quad (2-11)$$

2.3. Turbulence Model

Flows are turbulent in the present study. Turbulent flows consist of fluctuations in the flow field in time and space. It is a complex process, mainly because it is three dimensional, unsteady and consists of many scales. It can have a significant effect on the characteristics of the flow.

Turbulence occurs when the inertia forces in the fluid become significant compared to viscous forces, and is characterized by a high Reynolds Number. In principle, the Navier-Stokes equations describe both laminar and turbulent flows without the need for additional information. Turbulence models have been specifically developed to account for the effects of turbulence without recourse to a prohibitively fine mesh and direct numerical simulation. The most important approaches to simulate turbulence are Reynolds-averaged Navier-Stokes (RANS) models, large eddy simulation (LES) and detached-eddy simulation (DES) models. In present study, the RANS models are used.

Reynolds Averaged Navier-Stokes (RANS) equations are known as statistical turbulence models due to the statistical averaging procedure employed to obtain the equations. Simulation of the RANS equations greatly reduces the computational effort compared to a Direct Numerical Simulation (DNS) and is generally adopted for practical engineering calculations. However, the averaging procedure introduces additional unknown terms containing products of the fluctuating quantities, which act like additional stresses in the fluid. These terms, called 'turbulent' or 'Reynolds' stresses, must be determined as further unknowns. The method used to solve the system defines the type of turbulence model.

2.3.1. Reynolds Averaged Navier-Stokes (RANS) Equations

Assuming that the density fluctuations are negligible, the equations for transient flow can be averaged. A modified set of transport equations by introducing averaged and fluctuating components can then be solved for transient simulation. The resulting equations are called URANS (Unsteady Reynolds Averaged Navier-Stokes equations). Substituting the averaged quantities into the original equations results in the Reynolds averaged equations given below,

$$V = \bar{V} + V'$$

$$\frac{\partial \rho}{\partial t} + \frac{\partial}{\partial x_j}(\rho \bar{V}_j) = 0 \quad (2-12)$$

$$\frac{\partial \rho \bar{V}_i}{\partial t} + \frac{\partial}{\partial x_j}(\rho \bar{V}_i \bar{V}_j) = -\frac{\partial p}{\partial x_i} + \frac{\partial}{\partial x_j}(\sigma_{ij} - \rho \bar{V}_i' V_j') + S_M$$

where V_i are the velocity components, σ is the stress tensor including both normal and shear components of the stress, p is the pressure, S_M is the momentum source. Two types of models are used in practical applications:

- Eddy viscosity models: The eddy viscosity hypothesis assumes that the Reynolds stresses are related to the mean velocity gradients and turbulent viscosity by the gradient diffusion hypothesis similar to the relationship between the stress and strain tensors in laminar Newtonian flow,

$$-\rho \overline{V'_i V'_j} = \mu_t \left[\frac{\partial \overline{V}_i}{\partial x_j} + \frac{\partial \overline{V}_j}{\partial x_i} \right] - \frac{2}{3} \delta_{ij} \left(\rho k + \mu_t \frac{\partial \overline{V}_k}{\partial x_k} \right) \quad (2-13)$$

where μ_t is the eddy viscosity or turbulent viscosity. Eddy viscosity models represent several methods with different levels of complexity and accuracy such as algebraic (zero equation) models, one equation models and two equation models (k- ϵ , k- ω).

- Reynolds stress models: These models are based on transport equations for all components of the Reynolds stress tensor and the dissipation rate and do not use the eddy viscosity hypothesis.

Having in mind the need for the finer meshes in other turbulent models and considering the satisfactory results from the k- ϵ turbulence model reported in the literature for similar problems, we use k- ϵ model in this thesis.

k- ϵ model

The k- ϵ model is one of the most common turbulence models. It is a two equation model which includes two extra transport equations to represent the turbulent properties of the flow. This allows a two equation model to account for history effects like convection and diffusion of turbulent energy. The k- ϵ model has been shown to be useful for free-shear layer flows with relatively small pressure gradients. The transport equations for the standard k-epsilon model are given in Table 2.1.

Table 2-1 The transport equations for the standard k-ε model

For turbulent kinetic energy k
$\frac{\partial}{\partial t}(\rho k) + \frac{\partial}{\partial x_i}(\rho k \bar{V}_i) = \frac{\partial}{\partial x_j} \left[\left(\mu + \frac{\mu_t}{\sigma_k} \right) \frac{\partial k}{\partial x_j} \right] + P_k + P_b - \rho \varepsilon - Y_M + S_k$
For dissipation ε
$\frac{\partial}{\partial t}(\rho \varepsilon) + \frac{\partial}{\partial x_i}(\rho \varepsilon \bar{V}_i) = \frac{\partial}{\partial x_j} \left[\left(\mu + \frac{\mu_t}{\sigma_\varepsilon} \right) \frac{\partial \varepsilon}{\partial x_j} \right] + C_{1\varepsilon} \frac{\varepsilon}{k} (P_k + C_{3\varepsilon} P_b) + C_{2\varepsilon} \rho \frac{\varepsilon^2}{k} + S_\varepsilon$
Turbulent viscosity
$\mu_t = \rho C_\mu \frac{k^2}{\varepsilon}$
Product k
$P_k = -\rho \bar{V}_i' \bar{V}_j' \frac{\partial \bar{V}_j}{\partial x_i}$
Effect of buoyancy
$P_b = \theta g_i \frac{\mu_t}{Pr_t} \frac{\partial T}{\partial x_i}$

where Pr_t is the turbulent Prandtl number for energy and g_i is the component of the gravitational vector in the i th direction. For the standard and realizable - models, the default value of Pr_t is 0.85. The coefficient of thermal expansion, θ , is defined as

$$\theta = -\frac{1}{\rho} \left(\frac{\partial \rho}{\partial T} \right)_p$$

$$C_{1\varepsilon} = 1.44, \quad C_{2\varepsilon} = 1.92, \quad C_{3\varepsilon} = -0.33, \quad C_\mu = 0.09, \quad \sigma_k = 1.0, \quad \sigma_\varepsilon = 1.3$$

This model is widely used for flow calculations in practical engineering problems. The method has reasonable calculation time and was selected in this thesis for our analysis.

2.4. Structural Domain

When a solid undergoes a geometric change, we need, in addition to the reference Cartesian coordinates, another coordinate system that follows the deformed shape. In this case, the basic variable is displacement or the geometrical changes of a point in the continuum and such a

coordinate system is called the Lagrangian or material coordinates, commonly used in the solid mechanics. Here, the solid is considered as linear elastic. The equations used in classical elastodynamics are based on the following relations,

1. Equations of motion for a continuum

$$\sigma_{ij,j} + \rho_s b_i = \rho_s \dot{v}_i \quad (2-14)$$

2. The infinitesimal strain tensor

$$\gamma_{ij} = \frac{1}{2} (w_{ij} + w_{ji}) \quad (2-15)$$

3. The constitutive equation is

$$\sigma_{ij} = \bar{\lambda} \gamma_{kk} \delta_{ij} + 2\bar{\mu} \gamma_{ij} \quad (2-16)$$

where σ_{ij} 's are the stress tensor components, ρ_s is the density, γ_{ij} 's are the strain tensor components, $\bar{\lambda}$ and $\bar{\mu}$ are Lamé constants, δ_{ij} is the Kronecker delta, w_i 's are the components of the displacement vector \mathbf{w} , v_i 's are the components of the velocity field \mathbf{v} , b_i 's are the components of the body force \mathbf{b} and $i, j=1,2,3$.

As seen, there are 15 equations and 15 unknowns ($w_i, \sigma_{ij}, \gamma_{ij}$). Also, it can be noted that by combining the above equations we can obtain the Navier's equation of motion for isotropic, linear elastic solid as

$$(\bar{\lambda} + \bar{\mu}) \nabla(\nabla \cdot \mathbf{w}) + \bar{\mu} \nabla^2 \mathbf{w} + \rho \mathbf{b} = \rho \dot{\mathbf{v}} \quad (2-17)$$

The assumption of small deformation for solid is consistent with the actual deformation of solid in many cases. Of course, if the dynamic deformation of solid is considerably large or the stress-strain relationship is not linear, this assumption should be changed.

2.4.2. Dynamic structural analysis

In contrast with the static analysis, both inertia and damping effects are important and must be taken into account in the transient analysis. The basic equation of motion for the transient dynamic analysis is

$$M\ddot{\mathbf{W}} + C\dot{\mathbf{W}} + K\mathbf{W} = \mathbf{F}(t) \quad (2-18)$$

where \mathbf{M} , \mathbf{C} and \mathbf{K} are mass, damping and stiffness matrices, respectively, $\mathbf{F}(t)$ is the vector of externally applied load and $\ddot{\mathbf{W}}$, $\dot{\mathbf{W}}$ and \mathbf{W} are the acceleration, velocity and displacement vectors, respectively. It should be noted that the inertia and damping effects are neglected in the static analysis and Equation (2-18) reduces to $\mathbf{KW} = \mathbf{F}$. The choice for static or dynamic analysis (i.e., for including or neglecting the velocity and acceleration-dependent forces in the analysis) is usually decided by engineering judgment.

Transient analysis

Transient dynamic analysis is a technique to determine the dynamic response of a structure under the action of any general time-dependent load. Transient analysis can be used to find the time-varying displacements, strains, stresses and forces in a structure corresponding to any combination of static, transient and harmonic loads. Mathematically, Equation (2-18) represents a system of linear second order differential equations. The solution to this equation can be obtained by standard procedure for the solution of the general second order differential equations with constant coefficients (Boyce, 2001).

2.5. Damping in mechanical dynamic systems

In many practical systems, the vibrational energy is gradually converted to heat or sound. Due to the reduction in the energy, the response, such as the displacement of the system, gradually decreases. The mechanism by which the vibrational energy is gradually converted into heat or sound is known as damping. Although the amount of energy converted into heat or sound is relatively small, the consideration of damping becomes important for an accurate prediction of the vibration response of a system. The nature and the level of damping should be known in order to develop a dynamic model of the system and its peripherals. Knowledge of damping in a system is also important in imposing dynamic environmental limitations on the system (i.e., the maximum dynamic excitation the system could withstand) under in-service conditions. Furthermore, knowledge of its damping could be useful in order to make design modifications in a system that has failed acceptance tests. To characterize damping in a dynamic system, it is important, first, to understand the major mechanisms associated with mechanical-energy dissipation in the system. Then, a suitable damping model should be chosen to represent the associated energy dissipation. Finally, damping values (model parameters) are determined, for example, by testing the system or a representative physical model, by monitoring system

response under transient conditions during normal operation, or by employing already available data.

2.5.1. Types of Damping

There is some form of mechanical-energy dissipation in any dynamic system. In the modeling of systems, damping can be neglected if the mechanical energy that is dissipated during the time duration of interest is small in comparison to the initial total mechanical energy of excitation in the system. Several types of damping are inherently present in a mechanical system. Three primary mechanisms of damping are important in the study of mechanical systems. They are:

Material (Internal) Damping

Internal damping of materials originates from the energy dissipation associated with microstructure defects, such as grain boundaries and impurities; thermoelastic effects caused by local temperature gradients resulting from non-uniform stresses, as in vibrating beams; eddy-current effects in ferromagnetic materials; dislocation motion in metals; and chain motion in polymers. When a material is deformed, energy is absorbed and dissipated by the material. The effect is due to friction between the internal planes, which slip or slide as the deformations take place. When a body having material damping is subjected to vibration, the stress-strain diagram shows a hysteresis loop as indicated in Fig. 2-4.

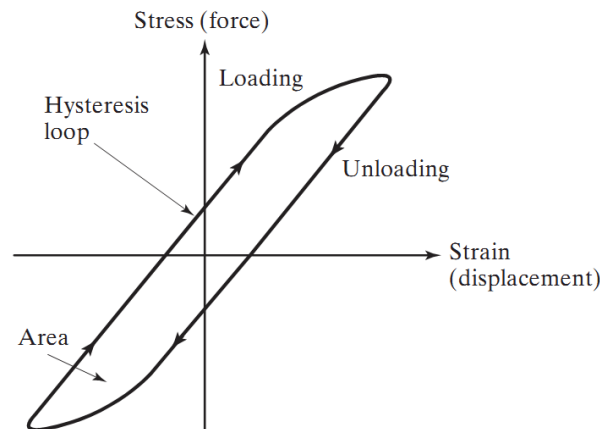


Fig. 2-4 Hysteresis loop for elastic materials

The area of this loop denotes the energy lost per unit volume of the body per cycle due to damping. Experience shows that energy dissipated by internal friction in a real system

does not depend on frequency. Since the material damping has not been understood well and therefore is difficult to quantify, a stiffness multiplier is used in practical applications for numerical simplicity.

Coulomb (Dry-Friction) Damping

Structural damping is a result of the mechanical-energy dissipation caused by rubbing friction resulting from relative motion between components and by impacting or intermittent contact at the joints in a mechanical system or structure. Energy-dissipation behavior depends on the details of the particular mechanical system in this case. Consequently, it is extremely difficult to develop a generalized analytical model that would satisfactorily describe structural damping. Energy dissipation caused by rubbing is usually represented by a Coulomb-friction model. Here the damping force is constant in magnitude but opposite in direction to that of the motion of the vibrating body. It is caused by friction between rubbing surfaces that either are dry or have insufficient lubrication.

Internal damping is usually negligible compared to structural damping. A large portion of mechanical energy dissipation in many engineering structures takes place through the structural-damping mechanism. A major form of structural damping is the slip damping resulting from the energy dissipation by friction at a structural joint. The degree of slip damping that is directly caused by Coulomb (dry) friction depends on several factors such as joint forces, surface properties, and the nature of the materials of the mating surfaces. This is associated with wear, corrosion, and general deterioration of the structural joint. In this sense, slip damping is time dependent.

Viscous Damping

Viscous damping is the most commonly used damping mechanism in vibration analysis. When mechanical systems vibrate in a fluid medium such as air, gas, water or oil the resistance offered by the fluid to the moving body causes energy to be dissipated. In this case, the amount of dissipated energy depends on many factors, such as the size and shape of the vibrating body, the viscosity of the fluid, the frequency of vibration, and the

velocity of the vibrating body. In viscous damping, the damping force is proportional to the velocity of the vibrating body and can be expressed as,

$$F = -c\dot{x} \quad (2-19)$$

Typical examples of viscous damping include (1) fluid film between sliding surfaces, (2) fluid flow around a piston in a cylinder, (3) fluid flow through an orifice, and (4) fluid film around a journal in a bearing.

2.5.2. Damping Measurement

There are two general ways by which damping measurements can be made: time-response methods and frequency-response methods. The basic difference between the two types of measurements is that the first type uses a time-response record of the system to estimate damping, whereas the second type uses a frequency-response record.

Logarithmic Decrement Method

This is perhaps the most popular time-response method used to measure damping. When a single-degree-of-freedom oscillatory system with viscous damping is excited by an impulse input (or an initial condition excitation), its response takes the form of a time decay (Fig. 2-5), given by Silva (2000) as

$$y(t) = y_0 e^{-\xi \omega_n t} \sin \omega_d t \quad (2-20)$$

in which the damped natural frequency is given by

$$\omega_d = \omega_n \sqrt{1 - \xi^2} \quad (2-21)$$

If the response at $t = t_i$ is denoted by y_i , and at $t = t_i + \frac{2\pi r}{\omega_d}$ is denoted by y_{i+r} , then from Equation (2-20),

$$\frac{y_{i+r}}{y_i} = e^{-\xi \frac{\omega_n}{\omega_d} (2\pi r)} \quad (2-22)$$

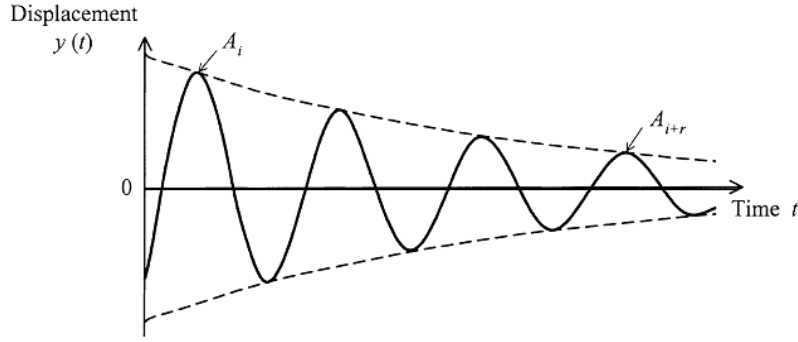


Fig. 2-5 Impulse response of a simple oscillator

In particular, suppose that y_i corresponds to a peak point in the time decay, having magnitude A_i , and y_{i+r} corresponds to the peak-point r cycles later in the time history, and its magnitude is denoted by A_{i+r} (see Fig. 2-5). Although the above equation holds for any pair of points that are r periods apart in the time history, the peak points seem to be the appropriate choice for measurement in the present procedure, as these values would be more prominent than any arbitrary points in a response time history. Then, (Silva, 2000)

$$\frac{A_{i+r}}{A_i} = e^{-\xi \frac{\omega_n}{\omega_d}(2\pi r)} = e^{-\frac{\xi}{\sqrt{1-\xi^2}}(2\pi r)} \quad (2-23)$$

where Equation (2-21) has been used. Then, the logarithmic decrement δ (per unit cycle) is given by

$$\delta = \frac{1}{r} \ln \left(\frac{A_i}{A_{i+r}} \right) = \frac{2\pi\xi}{\sqrt{1-\xi^2}} \quad (2-24)$$

or, the damping ration can be expressed as

$$\xi = \frac{1}{\sqrt{1 + \left(\frac{2\pi}{\delta} \right)^2}} \quad (2-25)$$

For low damping (typically, $\xi < 0.1$), $\omega_d \cong \omega_n$, and Equation (2-24) becomes

$$\frac{A_{i+r}}{A_i} \cong e^{-\xi(2\pi r)} \quad (2-26)$$

or

$$\xi = \frac{1}{2\pi r} \ln \left(\frac{A_i}{A_{i+r}} \right) = \frac{\delta}{2\pi} \quad \text{for } \xi < 0.1 \quad (2-27)$$

This is the logarithmic decrement. The damping ratio can be estimated from a free-decay record using Equation (2-27). Specifically, the ratio of the extreme amplitudes in prominent r cycles of decay is determined and substituted into Equation (2-27) to get the equivalent damping ratio. Alternatively, if n cycles of damped oscillation are needed for the amplitude to decay by a factor of two, for example, then, from Equation (2-27), one obtains

$$\xi = \frac{1}{2\pi n} \ln(2) = \frac{0.11}{n} \quad \text{for } \xi < 0.1 \quad (2-28)$$

For slow decays (low damping) the logarithmic decay in one cycle may be approximated by:

$$\ln \left(\frac{A_i}{A_{i+r}} \right) \cong \frac{2(A_i - A_{i+1})}{(A_i + A_{i+1})} \quad (2-29)$$

Then, from Equation (2-27), one obtains

$$\xi = \frac{(A_i - A_{i+1})}{\pi(A_i + A_{i+1})} \quad (2-30)$$

Any one of the Equations (2-25), (2-27), (2-28), and (2-30) can be employed in computing ξ from test data. It should be cautioned that the results assume single-degree-of-freedom system behavior. For multi-degree-of-freedom systems, the modal damping ratio for each mode can be determined using this method if the initial excitation is such that the decay takes place primarily in one mode of vibration. In other words, substantial modal separation and the presence of “real” modes (not “complex” modes with non-proportional damping) are assumed.

Step-Response Method

This is also a time-response method. If a unit-step excitation is applied to the single-degree-of-freedom oscillatory system, its time response is given by (Kelly, 2012; Silva, 2000)

$$y(t) = 1 - \frac{1}{\sqrt{1 - \xi^2}} e^{-\xi \omega_n t} \sin(\omega_d t + \phi) \quad (2-31)$$

in which $\phi = \cos^{-1} \xi$. A typical step-response curve is shown in Fig. 2-6. The time at the first peak (peak time), T_p , is given by

$$T_p = \frac{\pi}{\omega_d} = \frac{\pi}{\omega_n \sqrt{1 - \xi^2}} \quad (2-32)$$

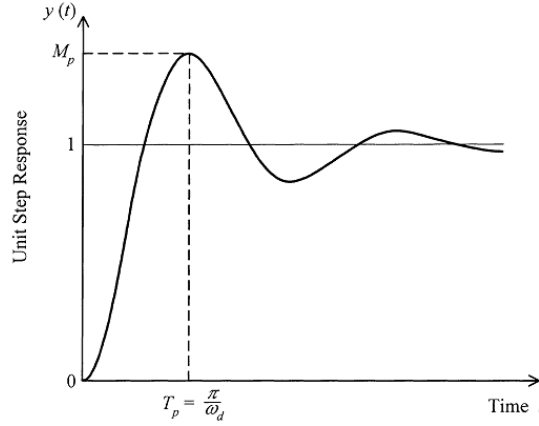


Fig. 2-6. A typical step response of a simple oscillator

The response at peak time (peak value), M_p , is given by

$$M_p = 1 + e^{-\xi \omega_n T_p} = 1 + e^{\frac{-\pi \xi}{\sqrt{1 - \xi^2}}} \quad (2-33)$$

The percentage overshoot, PO , is given by,

$$PO = (M_p - 1) \times 100\% = 100e^{\frac{-\pi \xi}{\sqrt{1 - \xi^2}}} \quad (2-34)$$

It follows that, if any one parameter of T_p , M_p , or PO is known from a step-response record, the corresponding damping ratio ξ can be computed using the appropriate relationship from the following: (Silva, 2000)

$$\xi = \sqrt{1 - \left(\frac{\pi}{T_p \omega_n} \right)^2} \quad (2-35)$$

$$\xi = \frac{1}{\sqrt{1 + \frac{1}{\left[\frac{\ln(M_p - 1)}{\pi} \right]^2}}} = \frac{1}{\sqrt{1 + \frac{1}{\left[\frac{\ln(PO/100)}{\pi} \right]^2}}} \quad (2-36)$$

It should be noted that, when determining M_p , the response curve should be normalized to unit steady-state value. Furthermore, the results are valid only for single-degree-of freedom systems and modal excitations in multi-degree-of-freedom systems.

Magnification-Factor Method

This is a frequency-response method. Consider the single-degree-of-freedom oscillatory system with viscous damping. The magnitude of its frequency-response function is

$$|H(\omega)| = \frac{\omega_n^2}{\sqrt{[(\omega_n^2 - \omega^2)^2 + 4\xi^2\omega_n^2\omega^2]}} \quad (2-37)$$

A plot of this expression with respect to ω , the frequency of excitation, is given in Fig. 2-7. The peak value of magnitude occurs when the denominator of the expression is minimum. This corresponds to

$$\frac{d}{d\omega} [(\omega_n^2 - \omega^2)^2 + 4\xi^2\omega_n^2\omega^2] = 0 \quad (2-38)$$

The resulting solution for ω is termed the resonant frequency ω_r ,

$$\omega_r = \sqrt{1 - 2\xi^2}\omega_n \quad (2-39)$$

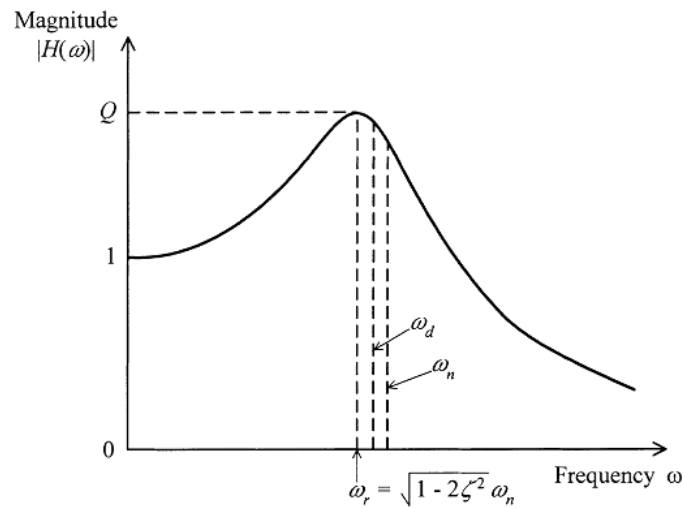


Fig. 2-7. The magnification factor method applied to a single-degree-of-freedom system

It is noted that $\omega_r < \omega_d$ but for low damping ($\xi < 0.1$), the values of ω_n , ω_d , and ω_r , are nearly equal. The amplification factor Q , which is the magnitude of the frequency response function at resonant frequency, is obtained by substituting Equation (2-39) in Equation (2-37), (Kelly, 2012)

$$Q = \frac{1}{2\xi\sqrt{1-\xi^2}} \quad (2-40)$$

For low damping ($\xi < 0.1$),

$$Q = \frac{1}{2\xi} \quad (2-41)$$

In fact, Equation (2-41) corresponds to the magnitude of the frequency-response function at $\omega = \omega_n$. It follows that, if the magnitude curve of the frequency-response function (or a Bode plot) is available, then the system damping ratio ξ can be estimated using Equation (2-41). In using this method, it should be remembered to normalize the frequency-response curve so that its magnitude at zero frequency (termed static gain) is unity. For a multi-degree-of-freedom system, modal damping values can be estimated from the magnitude Bode plot of its frequency-response function, provided that the modal frequencies are not too closely spaced and the system is lightly damped. Consider the logarithmic (base 10) magnitude plot shown in Fig. 2-8. The magnitude is expressed in decibels (dB), which is done by multiplying the \log_{10} (magnitude) by the factor 20. At the i^{th} resonant frequency ω_i , the amplification factor q_i (in dB) is obtained by drawing an asymptote to the preceding segment of the curve and measuring the peak value from the asymptote. Then,

$$Q_i = (10)^{\frac{q_i}{20}} \quad (2-42)$$

and the modal damping ratio,

$$\xi = \frac{1}{2Q_i} \quad i=1,2,\dots,n \quad (2-43)$$

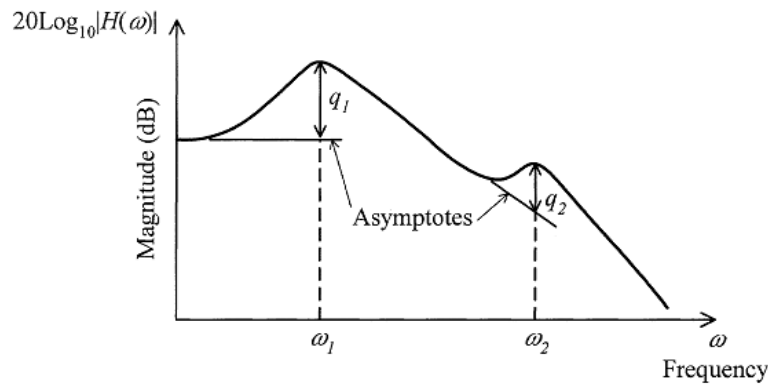


Fig. 2-8. Magnification factor method applied to a multi-degree-of-freedom system

If the significant resonances are closely spaced, curve-fitting to a suitable function might be necessary in order to determine the corresponding modal damping values. The Nyquist plot can also be used in computing damping using frequency domain data (Silva, 2000).

In the present study, we use the logarithmic decrement approach which is a time response method for estimating damping. It is mainly due to fact that in our analysis, we are using transient analysis in which the system response of the problem can directly be obtained from ANSYS-CFX modeling.

CHAPTER 3 FSI MODELING WITH ANSYS

Design of structures in contact with fluid needs specific attentions on the static and dynamic analysis and requires more accurate simulation tools (e.g., finite element method (FEM)) to improve performance of the system while minimizing the cost of manufacturing. The commercial package ANSYS was used with CFX for computational fluid dynamics and ANSYS mechanical for the structural simulation. The traditional approach to determine the mechanical stress and deflection of a structure in contact with fluid consists of a steady state computational fluid dynamics (CFD) simulation which provides the fluid pressure on the structure. This can then be applied as a boundary or load condition for the FEM simulation of the configuration (Schmucker et al., 2010). Such approach is called one-way coupled simulation since no deflection is fed back into CFD. To capture the influence of the deformed structure on the hydraulic performance, the deformation has to be brought back into the CFD solution such that an improved solution can be found and the loop can be closed. This comprises a so called two-way coupled fluid structure interaction (FSI) simulation or multi-field simulation and will be discussed in this chapter.

3.1. One-Way and Two-Way FSI

Solving FSI problems involves multi-field simulations of two separate physical behaviours. First, the fluid produces the load on the solid structure and is thereby a driving force whereas the solid structure as the second part reacts by means of stresses and deflections to the fluid field. The resulting deflection of the solid field has then an impact on the fluid field that has to adapt to the modified boundary. Finally, if one considers unsteady effects, the fluid field not only acts as a driving force, but also as a damping influence on the solid field since fluid mass has to be displaced during the motion of the structure which requires additional energy (Khalid et al., 2013; Schmucker et al., 2010). The solution of such a multi-field simulation usually requires two separate solvers, one for the fluid (CFD) and one for the structure (FEM) that run in sequential order when the information is exchanged between the CFX and FEM solvers at synchronization points (SP). A flowchart for the multi-field simulation with ANSYS and the sequence of synchronization points are shown in Fig. 3-1 and Fig. 3-2, respectively. While CFX provides the

forces, FEM returns the resulting deflections and the two meshes are adapted to the new geometry. The complete simulation is running until a convergence criterion is reached, e.g. the change in deflection from iteration to iteration is less than a certain value in the case of a steady state simulation or the selected real time duration is reached in the case of a transient FSI run. Details can be found in the documentation provided by ANSYS.

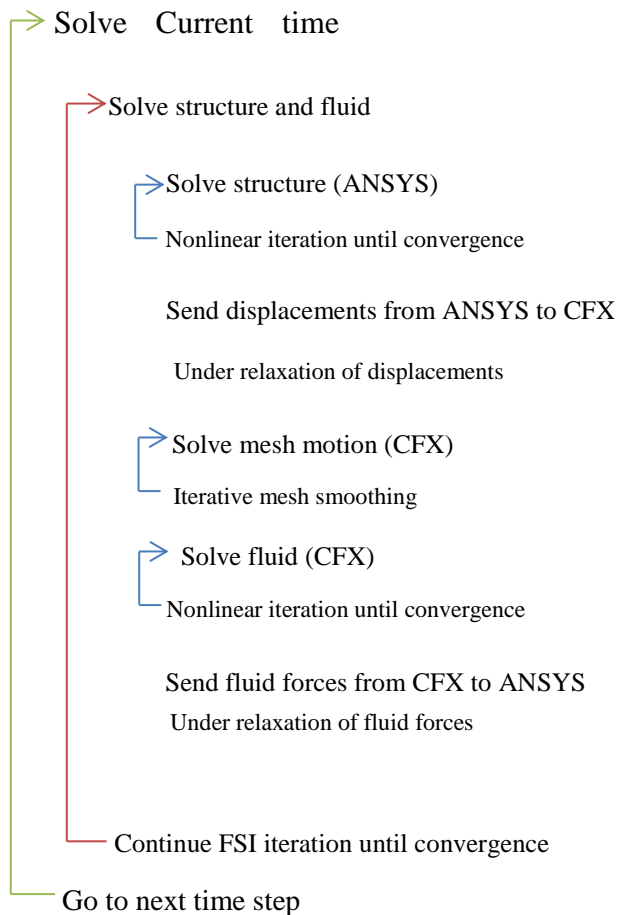


Fig. 3-1 Flowchart for multi-field simulations with ANSYS

As mentioned before, ANSYS supports two types of Fluid-Structure Interaction: one-way FSI and two-way FSI modeling. In the one-way FSI, CFD results are applied as loads in the mechanical analysis, but the results of the mechanical analysis are not passed back to a fluid analysis. In the two-way FSI, the results for displacements obtained from the mechanical analysis are used to modify the problem geometry and passed back to the fluid model. Two-way

FSI is important when the mechanical analysis could produce such deformation that, when implemented in the fluid analysis, would significantly affect the fluid analysis.

3.1.1. One-Way FSI

In a one-way FSI analysis, the results of the CFD analysis at the fluid-structure interface are transferred and applied as loads to the mechanical model. The subsequently calculated displacements or temperatures at the interface are not transferred back to the CFD analysis. One-way transfer is appropriate when displacements and temperatures differentials calculated are not large enough to have a significant impact on the fluid analysis. (Reference: ANSYS Mechanical User Guide)

3.1.2. Two-Way FSI

In a two-way FSI modeling, the results of the CFD analysis are transferred to the mechanical model whereas the subsequently calculated displacements at the interface are transferred back to the CFD analysis. The coupling capability that is currently available enables CFX to work with the ANSYS Mechanical solver within an ANSYS Multi-field simulation. During coupled simulations, the ANSYS CFX and Mechanical solvers execute the simulation through a sequence of multi-field time steps, each of which consists of one or more coupling iterations. Coupled simulations begin with the execution of the ANSYS Mechanical and CFX field solvers. The Mechanical solver acts as a coupling master process to which the CFX-Solver connects. Once the connection is established, the solvers advance through a sequence of six pre-defined synchronization points (SPs), as illustrated in Fig. 3-2. At each of these SPs, each field solver gathers the required data from the other solver in order to advance to the next point. The iterations are repeated until a maximum number of iterations are reached or until the data transferred between solvers and all field equations have converged.

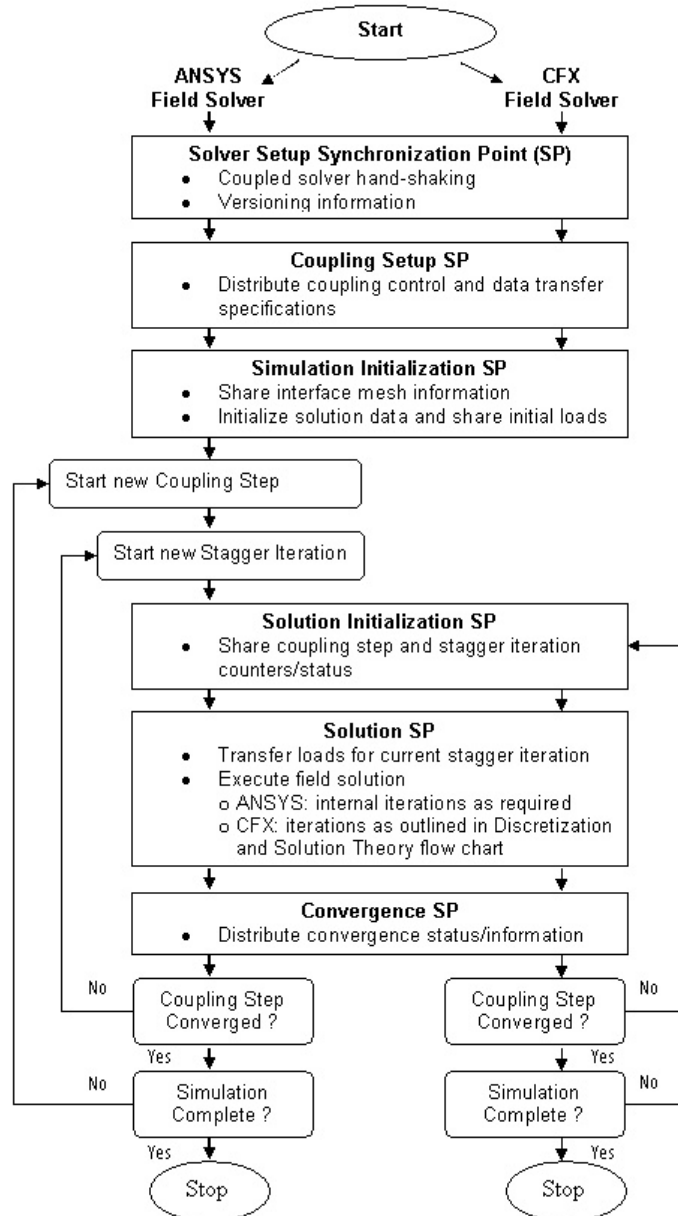


Fig. 3-2 Sequence of Synchronization Points (Reference ANSYS)

3.2. Modeling procedure

Fluid-Structure Interaction (FSI) analysis is an example of a multi-physics problem where the interaction between two different physics phenomena is taken into account. FSI analysis consists of performing a structural analysis in the application, with some of the forces coming from a corresponding fluid analysis or previous CFD analysis. In turn, the results of the mechanical analysis may be used in the fluid analysis. The interaction between the two analyses typically

takes place at the boundaries that the mechanical model shares with the fluids model. These boundaries of interaction are collectively called the fluid-structure interface. It is at this interface where the results of one analysis are passed to the other analysis as loads. The basic equations for fluid and structural domain are given in Chapter 2. The differential governing equations for the transient dynamic analysis of fluid structure problems are also presented in Chapter 2 as a system of linear second order differential equations and in terms of mass, damping and stiffness matrices (**M**, **C** and **K**), vector of externally applied load and acceleration, velocity and displacement vectors (\ddot{W} , \dot{W} and W). The general numerical procedure for solving the transient analysis can be divided into two methods of solution: direct integration method and mode superposition method. Although the two techniques may at first sight appear to be quite different, in fact, they are closely related, and the choice for one method or the other is determined only by their numerical effectiveness (Bathe, 1996).

3.2.1. Methods available for transient dynamic analysis in ANSYS

Three methods are available to do a transient dynamic analysis in ANSYS:

(i) Full method that uses the full system matrices with no matrix reduction. It is the most general of the three methods with the following advantages,

- It is easy to use because there is no need to worry about choosing master degree of freedoms or mode shapes;
- It allows all types of nonlinearities to be included;
- It uses full matrices with no matrix approximation involved;
- It calculates all displacements and stresses in a single pass;
- It works with all types of loads (i.e., nodal forces, imposed displacements and pressure and temperature load);

The main disadvantage of the method is that it is the most expensive method than either of the other methods and must be avoided if we are not interested to consider nonlinearities in the simulation.

(ii) Reduced method which condenses the problem size by using master degrees of freedom and reduced matrices. After finding the displacements at the master degrees of freedom, the program expands the solution to the original full degree of freedom set. The advantage of the

reduced method is that it is faster and less expensive than the full method. However, the method has several disadvantages,

- The time step must remain constant throughout the solution.
- The only nonlinearity allowed is simple node-to-node contact (gap condition)
- All loads must be applied at master degrees of freedom. Element loads such as temperature and pressure cannot be applied.

(iii) Mode superposition that uses the mode shapes (eigenvectors) from a modal analysis to calculate the structure's response. The method has the following advantages,

- It is faster and less expensive than the reduced or full method for many problems.
- It accepts considering damping ratio as a function of mode number.

The main disadvantages of the mode-superposition method are,

- The time step must remain constant throughout the analysis and automatic time stepping is not allowed.
- The only nonlinearity allowed is simple node-to-node contact (gap condition)
- It does not accept imposed nonzero displacements.

For complete details on performing a full transient dynamic analysis as we used in this thesis can be found in ANSYS Mechanical APDL Structural Analysis Guide. The modeling process starts in ANSYS-WORKBENCH multi-field when the simulation is performed between transient structural (ANSYS-MECHANICAL) and fluid flow (CFX-Pre). Both models are developed independently. Each model requires independent mesh, boundary conditions, analysis options and output options. The ANSYS-STRUCTURE works as a master code. It reads all commands including interface meshes from the CFX, maps and communicates time, and stagger loop controls to the CFX code. The ANSYS mapping is done to interpolate loads between dissimilar meshes on either side of the coupling interface. Initial analysis is performed for the structural part with the specified fundamental properties (density, Young's modulus and Poisson's ratio) for the structure. In the Mechanical Application, the structural part is meshed and the fluid part is suppressed. For creating fluid meshes, we can use GAMBIT or ICEM-CFD softwares. Appropriate names are assigned to all inlet, outlet and side surfaces and symmetry planes in the mesh generating software whereas corresponding boundary conditions for named surfaces and planes are specified in CFX-Pre. The motion of all the remaining nodes will be determined by

the mesh motion model. This model will be used to transfer the displacement applied at the boundary surface to the other nodes. The boundary type ‘wall’ is selected for the blade with mass and momentum option of ‘no-slip wall’. This condition by default indicates that the fluid sticks to the wall and moves with the same velocity at the wall. Fig. 3-3 shows CFX simulation model with defined boundary conditions (BC).

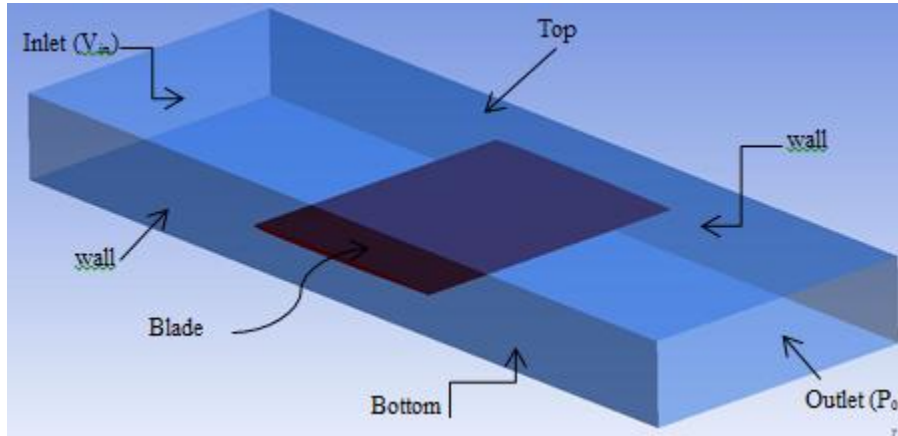


Fig. 3-3 Fluid boundary conditions

The differences between one-way and two-way coupled simulations can be seen in ‘ANSYS Field Solver’ (structural) window for forces and ‘ANSYS Interface Load Transfer’ window. These two windows do not appear in case of one-way FSI solver managers. The FSI simulation with the loads described above is run for different number of iterations depending on the time step. The number of iterations must be selected in such a way to reach a steady-state condition.

3.2.2. Forms of Damping in ANSYS

The damping matrix \mathbf{C} (as introduced in Equation (2-18)) may be used in harmonic, damped modal and transient analysis in ANSYS. In its most general form, it is:

$$[\mathbf{C}] = \alpha[\mathbf{M}] + \beta[\mathbf{K}] + \sum_{j=1}^{N_{mat}} \beta_j[\mathbf{K}_j] + \beta_c[\mathbf{K}] + [\mathbf{C}_\xi] + \sum_{k=1}^{N_{ele}} [\mathbf{C}_k] \quad (3-1)$$

where

α constant mass matrix multiplier (input on ALPHAD command)

β constant stiffness matrix multiplier (input on BETAD command)

β_j constant stiffness matrix multiplier (input on MP, DAMP command), material-dependent damping. It is noted that different damping parameters are defined for different types of analysis when using the material-dependent damping. For example, MP, DAMP in a spectrum analysis specifies a material-dependent damping ratio ξ , not β .

β_c variable stiffness matrix multiplier: (available for the harmonic response analysis, is used to give a constant damping ratio, regardless of frequency)

$$\beta_c = \frac{\xi}{\pi f} = \frac{2\xi}{\omega} = \frac{\eta}{\omega} \quad (3-2)$$

ξ constant damping ratio (input on DMPRAT command). From Equation (3-2), the damping ratio ξ should be $\frac{\eta}{2}$ where η is the loss factor.

f frequency in the range between f_b (beginning frequency) and f_e (end frequency);

$[C_\xi]$ frequency-dependent damping matrix, $[C_\xi]$ may be calculated from the specified ξ_r (damping ratio for mode shape r) and is never explicitly computed.

$$\{W_r\}^T [C_\xi] \{W_r\} = 4\pi f_r \xi_r \quad (3-3)$$

f_r frequency associated with mode shape r

$$\xi_r = \xi + \xi_{mr} \quad (3-4)$$

ξ constant damping ratio (input on DMPRAT command)

ξ_{mr} modal damping ratio for mode shape r (input on MDAMP command)

$[C_k]$ element damping matrix

The following forms of damping models are available in ANSYS:

Constant Damping: This property is available for random vibration analyses.

Constant Damping Ratio: This specifies the amount of damping in the structure as a percentage of critical damping. It is used in conjunction with the stiffness coefficient and mass coefficient.

Stiffness Coefficient (Beta Damping, β): It is a coefficient value that is used to define a beta damping by multiplying it with stiffness. Its value can be entered directly or computed from a damping ratio at a specified frequency.

Mass Coefficient (Alpha Damping Factor, α): This coefficient is used to define an alpha damping by multiplying it with mass. Beta and alpha damping factors are collectively called Rayleigh damping. The damping matrix $[C]$ is calculated by using these constants to multiply the mass matrix $[M]$ and stiffness matrix $[K]$:

$$[C] = \alpha[M] + \beta[K] \quad (3-5)$$

The values of α and β are not generally known directly, but are calculated from modal damping ratios, ξ_i . ξ_i is the ratio of actual damping to critical damping for a particular mode of vibration. If ω_i is the natural circular frequency of mode i , α and β satisfy the relation

$$\xi_i = \frac{\alpha}{2\omega_i} + \frac{\beta\omega_i}{2} \quad (3-6)$$

In many practical structural problems, alpha damping (or mass damping) may be ignored ($\alpha = 0$).

In such cases, we can evaluate β from known values of ξ_i and ω_i , as

$$\beta = \frac{2\xi_i}{\omega_i} \quad (3-7)$$

Since only one value of β can be input in a load step, the most dominant frequency active in that load step can be used to calculate β . To specify both α and β for a given damping ratio ξ , it is commonly assumed that the sum of the α and β terms is nearly constant over a range of frequencies.

$$\alpha = 2\xi \frac{\omega_1\omega_2}{\omega_1 + \omega_2} \quad (3-8)$$

$$\beta = \frac{2\xi}{\omega_1 + \omega_2} \quad (3-9)$$

Alpha damping can lead to undesirable results if an artificially large mass has been introduced into the model. One common example is when an artificially large mass is added to the base of a structure to facilitate acceleration spectrum input. The alpha damping coefficient, which is multiplied by the mass matrix, will produce artificially large damping forces in such a system, leading to inaccuracies in the spectrum input, as well as in the system response. Beta damping and material damping can lead to undesirable results in a nonlinear analysis. These damping

coefficients are multiplied by the stiffness matrix, which is constantly changing in a nonlinear analysis. Beta damping is not applied to the stiffness matrices generated by contact elements. The resulting change in damping can sometimes be opposite to the actual change in damping that can occur in physical structures. For example, whereas physical systems that experience softening due to plastic response will usually experience a corresponding increase in damping, an ANSYS model that has beta damping will experience a decrease in damping as plastic softening response develops.

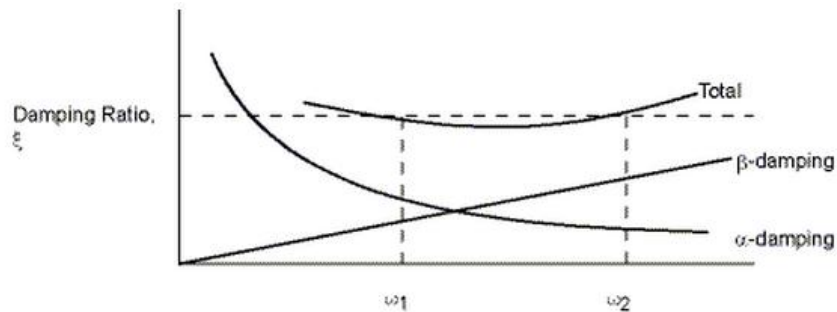


Fig. 3-4 Rayleigh Damping

The constant damping ratio represents the ratio of actual damping to critical damping and is the simplest way of specifying damping in the structure.

Numerical Damping: It is referred to as amplitude decay factor (γ). This parameter controls the numerical noise produced by the higher frequencies of a structure. Usually the contributions of these high frequency modes are not accurate and some numerical damping is preferable. A default value of 0.1 is used for transient structural analysis and a default value of 0.005 is used for transient structural analysis using a linked modal analysis system.

Material Damping: When a material (i.e., viscoelastic materials) is deformed, energy is absorbed and dissipated by the material due to the friction between the internal planes. There are two types of material-based damping, “*Material Dependent Damping*” and “*Constant Damping Coefficient*”. *Material Dependent Damping* consists of beta damping and alpha damping. In the present analysis and due to the material of the blade structure which is elastic, the material damping is negligible and can be ignored in the analysis.

CHAPTER 4 VALIDATION

The coupling procedure presented in the previous chapters is applied to the oscillating plate problem in this chapter. In this problem, the oscillation of a vertical plate in a cavity filled with a fluid is considered in order to show the basic steps in fluid-structure interaction analysis with ANSYS-CFX 14. The effects of time step and viscous damping are studied in this example.

4.1. Oscillating Plate

In order to study the validity of our modeling, the oscillation of a vertical plate in a cavity filled with a fluid is investigated in this section. A schematic diagram describing the problem is shown in Fig. 4-1 (Großmann et al., 2012; Kim and Youn, 2012).

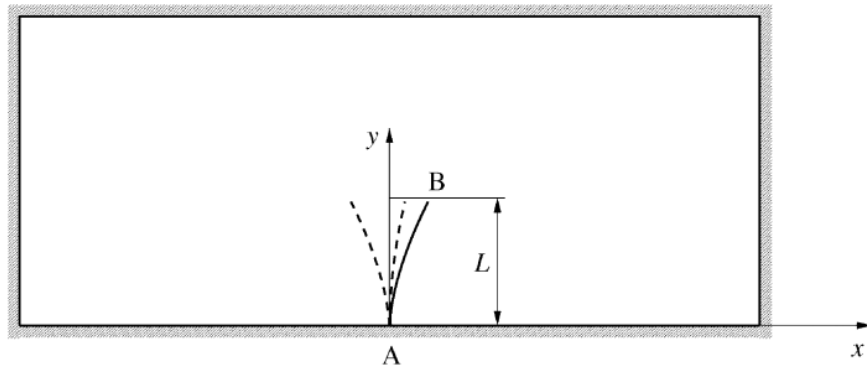


Fig. 4-1 Geometry of oscillating plate (not drawn to scale)

A thin flexible plate with length $L=1.0$ m, width $w=0.4$ m and thickness $t=60$ mm is clamped at the lower boundary. The coupled simulations are performed in three dimensions. The flexible plate has a modulus of elasticity of $E=2.5$ MPa, a Poisson's ratio of $\nu=0.35$, and a density of $\rho=2550$ kg/m³. The fluid density is $\rho_F=1$ kg/m³. Three different dynamic viscosities ($\mu_{F_1}=0.2$ Pa.s; $\mu_{F_2}=1.0$ Pa.s and $\mu_{F_3}=5.0$ Pa.s) are considered for the flow in the laminar range. The computational mesh used in the present study (Fig. 4-2) is similar to that given in Reference (Großmann et al., 2012). The computational domain is taken as follows:

- the distance from the left wall of the cavity to the plate center plane is $10L$,
- the distance from the plate center plane to the right wall of the cavity is $40L$,
- the height of the cavity is $6L$.

- the fluid is considered with the symmetry boundary condition in the z-direction.

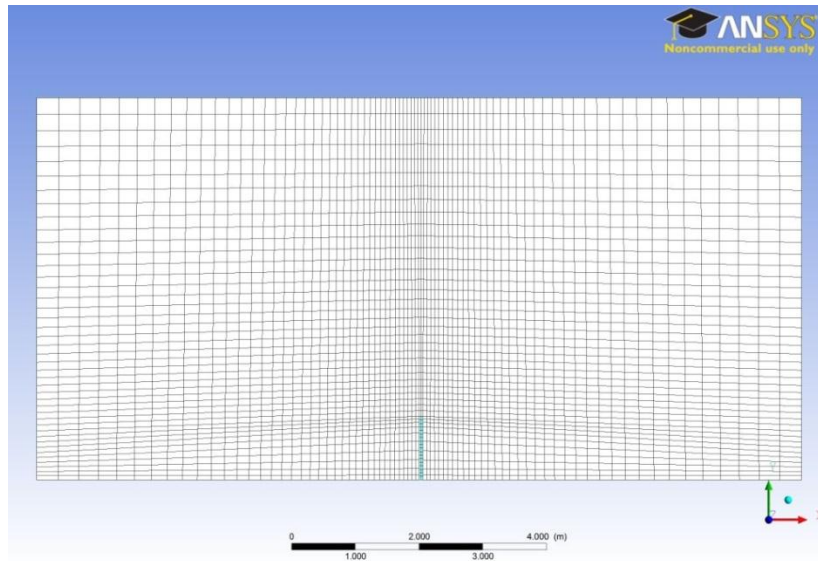


Fig. 4-2 The computational mesh

The size of the time step is governed by the first natural frequency of the structure we wish to capture. The smaller the time step, the higher the mode frequency we will capture. A modal analysis gives the first natural frequency of the plate in dry conditions as $f=0.31072$ Hz. We started our investigation with $dt = 0.1 \approx \frac{1}{33f}$ while the same time step was also used by Glück et al. (2001) and Namkoong et al. (2005). In other words, we must choose our step size such that we will have 33 discrete points per period of the oscillations. The problem is also solved with smaller values of time steps. During the first five steps, i.e., $t \leq 0.5$ s, a uniformly distributed load of 30N/m is applied in order to excite the plate. From the sixth time step on, the plate is loaded by the reacting pressure resulting from the fluid flow. In Fig. 4-3 to Fig. 4-10, the displacements of the free end of the plate for three different viscosities of the fluid are compared with those given by Glück et al. (2001) and Namkoong et al. (2005). There exist slight discrepancies in the frequency and the amplitude of oscillation. However, both the frequency and amplitude of the oscillations are decreased as the viscosity of the fluid is increased. It can also be seen that the higher the viscosity of the fluid is, the faster the plate is damped and reaches its initial state again. Considering that the results reported by Glück et al. (2001) and Namkoong et al. (2005) are based on two-dimensional simulations, these slight discrepancies can be considered quite acceptable. Fig. 4-3 shows the horizontal displacement of the free end of the plate for $\mu=0.2$ for

different time steps and numerical damping $ND=0.1$ (which is taken in ANSYS by default). The effect of numerical damping will be investigated in section 4.1.2.

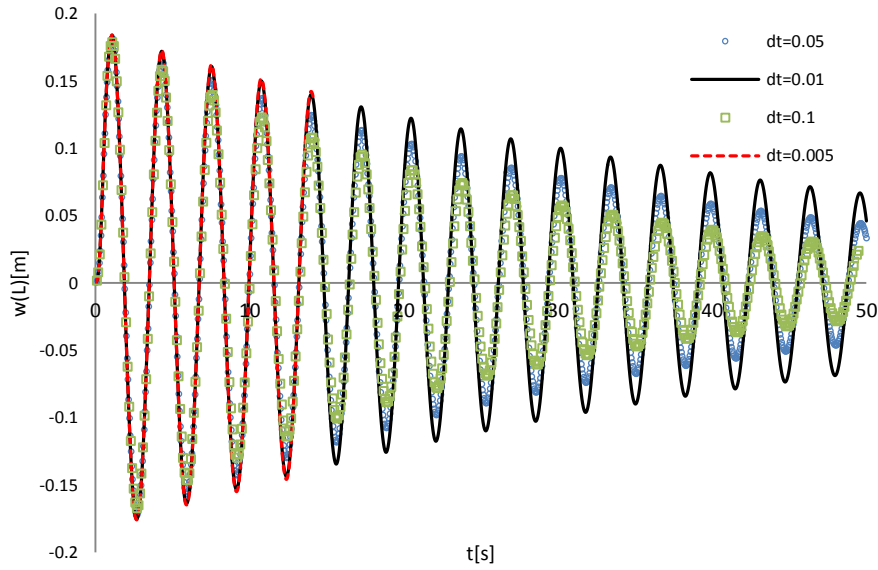


Fig. 4-3 Horizontal displacement of the free end of the plate for different time steps and $\mu=0.2$ ($ND=0.1$)

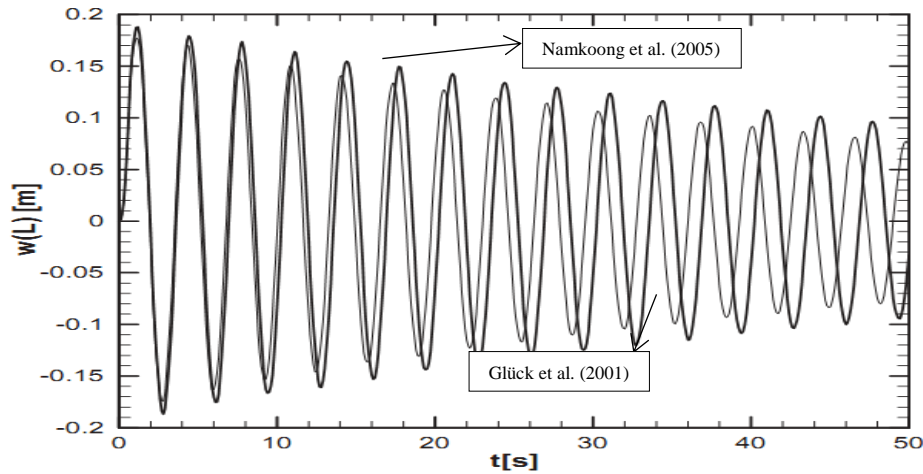


Fig. 4-4 Comparison of the displacements of the free end of the plate for $\mu=0.2$;

Our observation showed that the results obtained for ($dt=0.01s$ and $0.005s$) in Fig. 4-3, are in good agreement with those reported by Glück et al. (2001) in Fig. 4-4 ($dt=0.01s$). Similar behavior can also be observed by comparing Fig. 4-5 and Fig. 4-6. The horizontal displacement of the free end of the plate for $\mu=1$ for different time steps are also given in Fig. 4-5 and are compared with those reported by Glück et al. (2001) and Namkoong et al. (2005) in Fig. 4-6. In

Fig. 4-7 and Fig. 4-8, the results for the horizontal displacement of the free end of the plate for $\mu=5$ are compared with the results given in references (Glück et al., 2001; Namkoong et al., 2005).

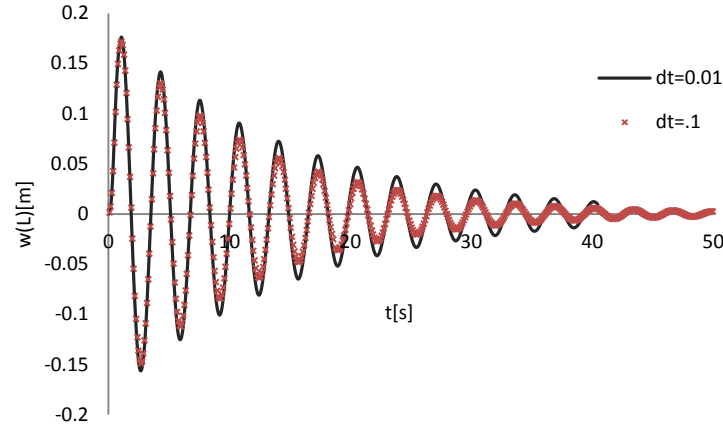


Fig. 4-5 Horizontal displacements of the free end of the plate for different time steps and $\mu=1$ (ND=0.1)

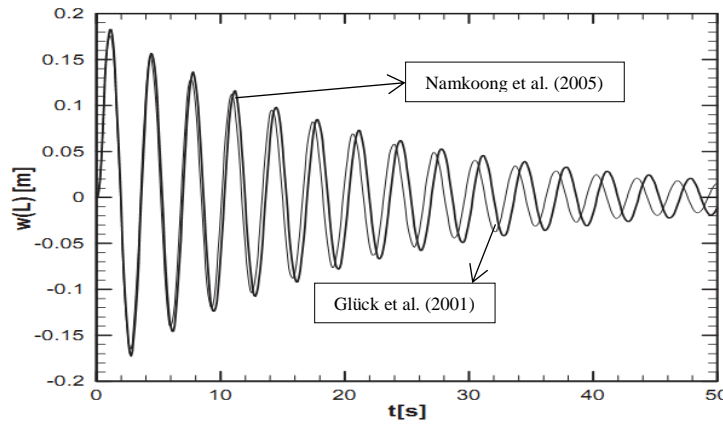


Fig. 4-6 Comparison of the displacements of the free end of the plate for $\mu=1$;

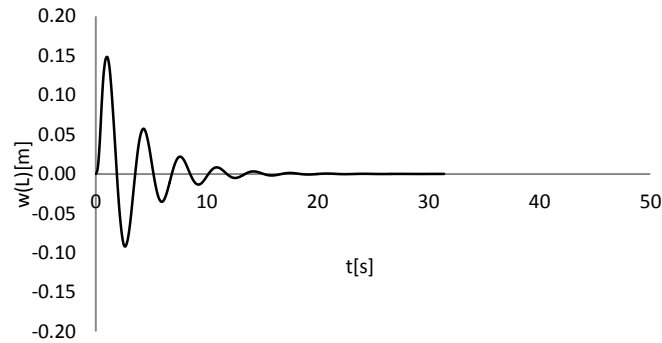


Fig. 4-7 Horizontal displacements of the free end of the plate for time step $dt=0.01$ and $\mu=5$ (ND=0.1)

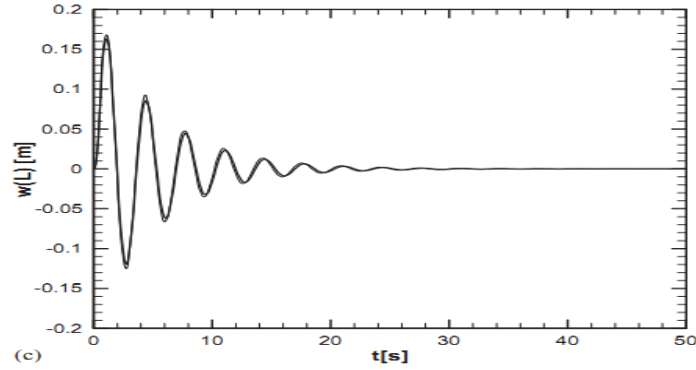


Fig. 4-8 Comparison of the displacements of the free end of the plate for $\mu=5$;
 -----,Glück et al. (2001); _____,Namkoong et al. (2005).

4.1.1. Effect of dynamic viscosity

The effects of dynamic viscosity are investigated in Fig. 4-9 to Fig. 4-12. The value of damping ratio (ξ) for the problem can be estimated using the logarithmic decrement as described in section 2.5.2 and measuring the consecutive horizontal displacements x_1 and x_2 of the free end of the plate for different fluid viscosities as shown in Fig. 4-9. The damping ratio (ξ) is related to the logarithmic decrement in terms of two consecutive displacements one cycle apart (Equation (2-25)). As it can be seen from Fig. 4-9 to Fig. 4-12, increasing the dynamic viscosity will increase the damping effects on the vibration amplitudes as expected. It should be noted that since the same value for fluid density is assumed in all three cases, the damping effect of the fluid on the amplitude of the plate oscillations is increased with increasing the fluid viscosity. This observation is also in agreement with the results given in the previous subsection when it was shown that the amplitude of plate vibrations is reduced with increasing the dynamic viscosity and density of the fluid.

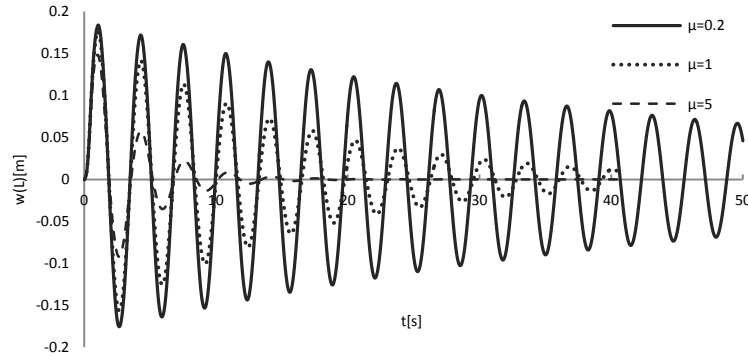


Fig. 4-9 Horizontal displacement of the free end of the plate for different fluid viscosities ($dt=0.01$)

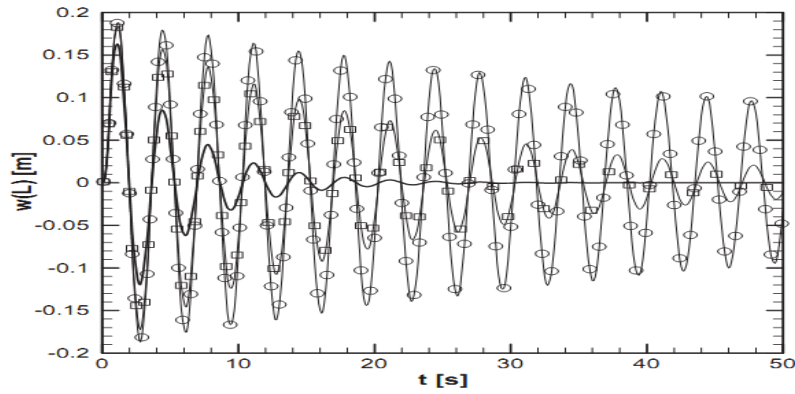


Fig. 4-10 Horizontal displacement of the free end of the plate for different fluid viscosities, \circ — $\mu=0.2$; \square — $\mu=1$; — $\mu=5$ [Namkoong et al.(2005)]

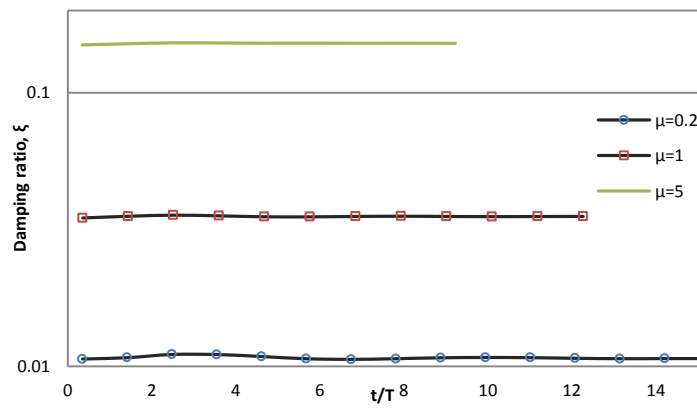


Fig. 4-11 Damping ratio (ξ) calculated for different fluid viscosities ($dt=0.01$)

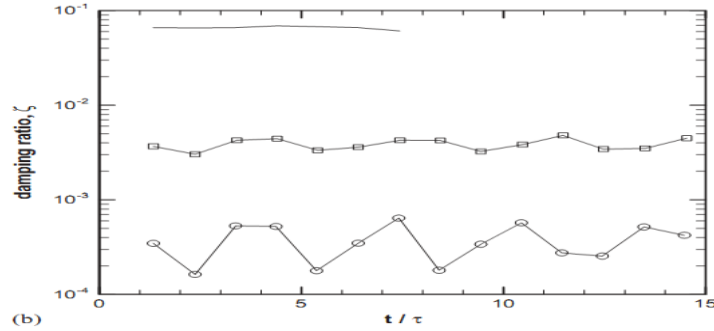


Fig. 4-12 Damping ratio calculated for different fluid viscosities,

—○— $\mu=0.2$; —□— $\mu=1$; — $\mu=5$ [Namkoong et al.(2005)]

It should also be noted that some differences can be observed between our calculations with those reported by Namkoong et al. (2005). However, these differences are probably due to the fact that the simulation done by Namkoong et al. (2005) was based on two-dimensional Euler beam theory.

4.1.2. Effect of numerical damping

Transient analysis in ANSYS is based on two numerical schemes: the Newmark method and the HHT method. Numerical damping is a parameter used in ANSYS during transient analysis to artificially control numerical noise and stabilize the numerical integration scheme by damping out the unwanted high frequency modes. It should be noted that the numerical damping is not true damping and is associated with the time-stepping schemes in transient analysis for integrating second-order systems of equations over time. For the Newmark method, numerical damping also affects the lower modes and reduces the accuracy of the integration scheme from second order to first order. For the HHT method, numerical damping affects only the higher modes and always maintains second-order accuracy. The value of 10% is used in ANSYS by default for numerical damping. This value of numerical damping ($ND=0.1$) is used to plot the horizontal displacement of the free end of the oscillating plate for $\mu=0.2$ and different time steps in Fig. 4-3. We reduced the value of numerical damping to $ND=0.01$ (1%) in Fig. 4-13 to plot the horizontal displacements of the free end of the plate for the time step ($dt=0.1$).

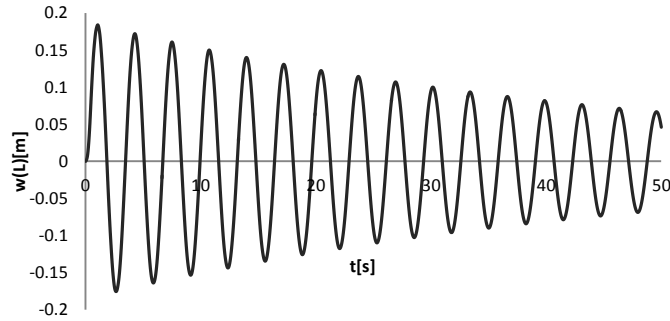


Fig. 4-13 Horizontal displacements of the free end of the plate for $dt=0.1$ & $ND=0.01$ & $\mu=0.2$

We observed that the results obtained for $dt=0.1$ and $ND=0.01$ (Fig. 4-13) are very close to those obtained for a smaller time step $dt=0.01$ and $ND=0.1$ (Fig. 4-3). One idea stems from this comparison: can we use bigger time steps in our analysis if we use a smaller value for ND ? Moreover, what would be the appropriate value of ND in our analysis and can we take $ND=0$?

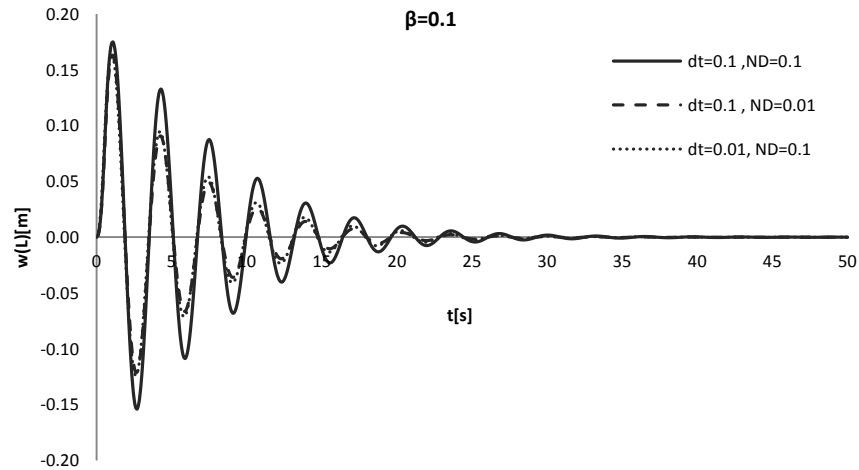


Fig. 4-14 Horizontal displacements of the free end of the plate for different dt and ND (with $\mu=0$)

To answer the above questions and to continue our investigation on the effect of numerical damping, the oscillating plate is considered in dry condition (without viscous damping) but with material (structural) damping. The reason for making this assumption is that the viscous damping is obtained from experiment or must be calculated from a fluid-structure interaction analysis whereas the material damping can be defined in the beginning of our analysis in ANSYS (with input parameters α and β). The damping formulation available in ANSYS was given in Equation (3-5). By assuming the oscillating plate in dry condition, a better estimation on the total damping can be found because no viscous damping is present in the analysis and the problem has only

material damping and numerical damping. To perform our investigation, we do the analysis with an input value for the material damping (by assigning a value to parameter β in ANSYS). The results of the program for vibration amplitudes are then used to calculate the equivalent damping β^* as explained in the following. Our goal is to find appropriate values for the time step (dt) and numerical damping (ND) for which the equivalent damping β^* coincides with the input data for parameter β . The equivalent damping constant β^* is evaluated as follows:

Step I: having the ANSYS output graph for the vibration displacements of the free end of the plate (e.g., Fig. 4-14) and measuring two consecutive displacements x_1 and x_2 (one cycle apart), the logarithmic decrement can be evaluated by using the formula $\delta = \ln(x_1/x_2)$.

Step II: damping ratio (ξ) is calculated by Equation (2-25).

Step III: the parameter β^* is calculated by using Equation (3-6) written in the following form,

$$\xi = \frac{\alpha}{2\omega} + \frac{\beta^*\omega}{2} \quad (4-1)$$

(The theoretical derivation of this equation has been given in chapter 3).

The problem is solved for different values of material damping β (with $\alpha = 0$), numerical damping (ND) and time step (dt). The results of this investigation and parameters used are given in Table 4-1. The values of damping ratio (ξ) and equivalent damping constant β^* are calculated using Equations (2-25) and (4-1), respectively. It can be seen from Table 4-1 that the best agreement between the calculated damping constant β^* and the assumed material damping β is obtained for $dt=0.01$ and $ND=0.1$. Moreover, because of the discrete nature of numerical methods, the solution computed by ANSYS depends on the time step used. The appropriate time step must be in general small enough to produce a stable solution. In the above discussion, we tried to determine an appropriate time step for the problem at hand by comparing the calculated equivalent damping constant β^* with the input value of material damping β . Regarding the first question on the possibility of using bigger time steps with smaller numerical damping (ND) and based on our observations, we concluded that the effects of reducing the time step in some cases might also be achieved by reducing the numerical damping considered in the numerical solution. However and as it can be seen from Table 4-1, this observation cannot be generalized as probably desired. Therefore, the explicit answer to the first question is “NO” in general.

Table 4-1 Parameters to investigate the effects of numerical damping and time step (Dry-condition)

	Numerical damping (ND)	Time step (dt)	ξ (Calculated) Equation (1)	β^* (Calculated) Equation (2)	$\beta-\beta^*$ (Error)
$\beta=0$	0.10	0.10	4.51×10^{-4}	4.51×10^{-4}	4.51×10^{-4}
		0.01	5.04×10^{-4}	5.04×10^{-4}	5.04×10^{-4}
	0.01	0.10	1.22×10^{-3}	1.22×10^{-3}	1.22×10^{-3}
$\beta=0.1$	0.10	0.10	8.25×10^{-2}	8.46×10^{-2}	1.54×10^{-2}
		0.01	9.79×10^{-2}	1.0×10^{-1}	0
	0.01	0.10	9.59×10^{-2}	9.8×10^{-2}	2×10^{-3}
		0.01	11.25×10^{-2}	1.15×10^{-1}	1.5×10^{-2}

For still better understanding of the effects of the numerical damping and to find an appropriate value of ND in the analysis, another problem of transient analysis of a cantilever beam is considered here as shown in Fig. 4-15.

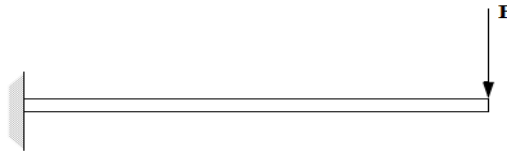


Fig. 4-15 Geometry of cantilever beam (Example 2)

The modulus of elasticity (E) and density (ρ) for the beam are given as 206.8 GPa and 7830 kg/m³, respectively. The cross section of the beam is a rectangle of 0.01 m×0.01 m. A vertical downward impulse load of magnitude 100 N is applied at the end of the beam. It should be noted that since an ideal impulse force excites all modes of the beam, the response of the beam should contain all mode frequencies. However, we cannot produce an ideal impulse force numerically and we have to apply the load over a discrete amount of time dt . As mentioned before, the size of the time step is governed by the first natural frequency of the structure. Moreover, it should be noted that a transient analysis is more involved than a static or harmonic analysis and requires better understanding of the dynamic behavior of the structure. Therefore, a modal analysis of the structure should be initially performed to provide information about the structure's dynamic behavior. The first natural frequency of the cantilever beam is obtained from a free vibration modal analysis as 8.16Hz. To produce the impulse force in this analysis, the

applied force is considered over one time step (Time step=0.001 s). One probe is also placed at the end of the beam to measure the response of that node (UY) with time. Three methods are available to do a transient dynamic analysis in ANSYS: (i) Full method that uses the full system matrices with no matrix reduction. (ii) Reduced method which condenses the problem size by using master degrees of freedom and reduced matrices. (iii) Mode superposition that uses the mode shapes (eigenvectors) from a modal analysis to calculate the structure's response. Here we used a full method to solve the problem. The problem is solved with different values of numerical damping 0.01 and 0.1. The variations of the displacements of the free end of the cantilever beam are shown in Fig. 4-16 and Fig. 4-17. It can be seen from Fig. 4-16 that the displacements obtained for numerical damping values 0.01 and 0.1 are similar for the first few time steps. However with increasing the value of numerical damping from 0.01 to 0.1 (Fig. 4-17) and after passing a number of time steps (for $t > 9.7$ sec), the high frequency noises observed in the displacement response of the free end of the cantilever beam disappears. It can be concluded from these observations that the default value of ND=0.1 gives satisfactory results and can be considered as an appropriate value of numerical damping in our foregoing analysis with confidence. Moreover, we concluded that the numerical damping is essential in the analysis and cannot be taken as zero. It should also be noted that ignoring (or reducing) the numerical damping may cause the solution to diverge. Our final conclusions from the above discussion made in this section can be summarized as follows,

- The numerical damping (ND) must be included in our transient analysis to stabilize the numerical calculations (prevent divergence) and cannot be taken as zero.
- Although we could compensate the effects of using bigger time steps in our analysis for some cases by assuming smaller values for the numerical damping (ND), this conclusion cannot be drawn in general.
- We received satisfactory results by using the default value of ND=0.1 (10%) as suggested by ANSYS and this value will be used in our analysis throughout this thesis.



Fig. 4-16 The variations of the displacements of the free end of the cantilever beam for the first few time steps

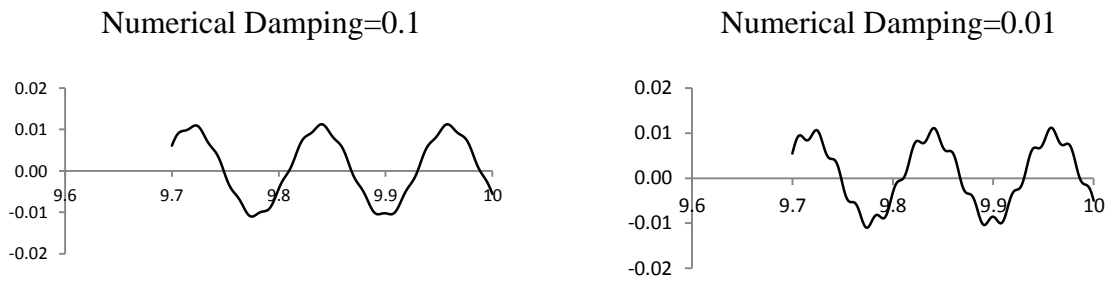


Fig. 4-17 The variations of the displacements of the free end of the cantilever beam for $t > 9.7$ sec.

CHAPTER 5 HYDROFOIL BLADE

Investigation of the hydro-elastic behavior of vibrating blades is of strong interest in turbo machinery applications. The importance of this investigation comes from the fact that blade vibration is an inherent characteristic in the operation of turbines, due to the passing of the rotor blades through the trailing wakes from the upstream stator blade stage. It is the main goal of the present chapter to implement a two-way fluid-structure interaction (FSI) approach for hydro-elastic analysis of vibrating blades and identify the hydrodynamic damping in a reliable way to determine the influence of the flow velocity. The results of the present analysis will also be compared with those from experiment. The hydrodynamic damping is the fluid contribution to the total damping, of an immersed vibrating structure. This type of damping is one of the main parameters influencing the amplitude of blade vibrations and is crucial for manufactures who try to assess the dynamics of runners at the earliest stage of the design phase. Moreover, it is directly related to fatigue problems in hydraulic machines which are of great importance in their design procedure. The identification of blade hydrodynamic damping is influenced by many different parameters, such as the flow velocity, the fluid density and the flow velocity distribution around the blade. Moreover, the fluid environment makes the excitation of an immersed structure difficult. In this chapter as a representative case study of a vibrating blade in Francis turbines, a hydrofoil blade in a water channel is considered in clamped-clamped condition under the action of a line-distributed force at the middle. A schematic diagram of the problem is shown in Fig. 1. Due to symmetry of the problem, only half of the blade is considered in the computational analysis. The material properties of the blade are given as Young's modulus $E=193$ Gpa, density $= 8000 \text{ kg/m}^3$ and Poisson ratio $\nu=0.3$. The chord length of the blade is considered as 279 mm.

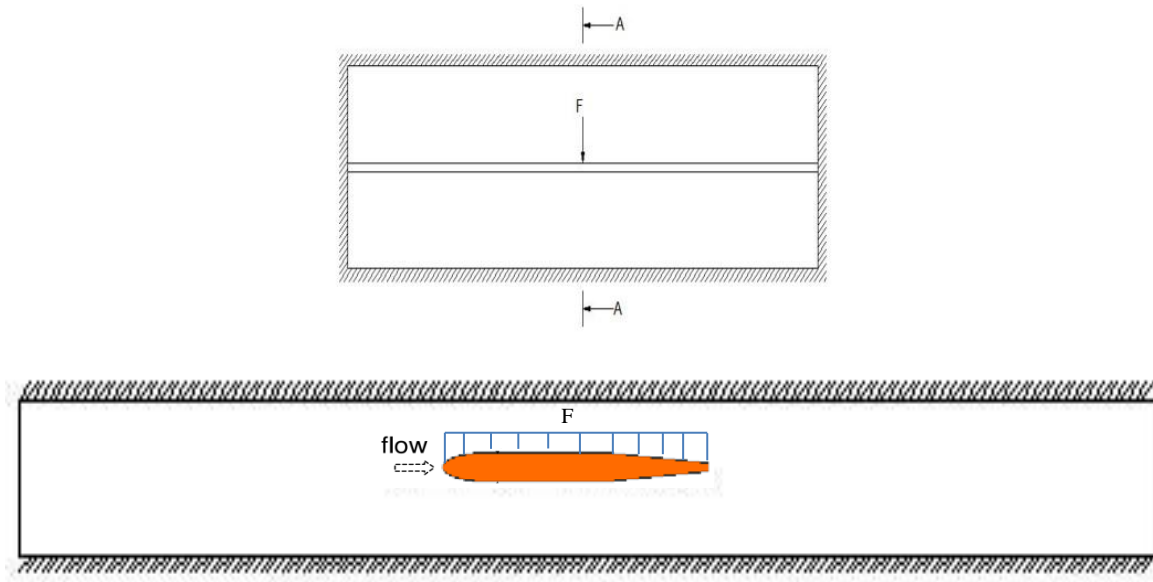


Fig. 5-1 A schematic diagram of the computational domain

The results of simulations are compared with the experimental observations and estimations reported by Seeley et al. (2012). They presented an experimental investigation of damping due to FSI in realistic flowing conditions. Macro-fiber composite (MFC) piezoelectric actuators were bonded to a plate contoured with a hydraulic profile. The plate was placed in a test section, subjected to water at increasing velocities, and excited with sine sweeps using the MFCs. The test section was designed to create realistic water flow conditions, similar to those found in industrial scale Francis turbines. Three hydrofoils were designed and built to be evaluated in the test section (Fig. 5-2) and Table 5-1. The hydrofoil was clamped into place along both sides, and a clear plastic window facilitated visual inspection. Sufficient transition zones from the rectangular test section to the circular pipes were added on the inlet and the outlet to minimize turbulence. Natural frequency and damping estimates were experimentally obtained in their work from sine sweep frequency response functions measured with a laser vibrometer through the window in the test section. The blade H1 is used in this chapter to demonstrate the applicability and validation of the results obtained from the present study.

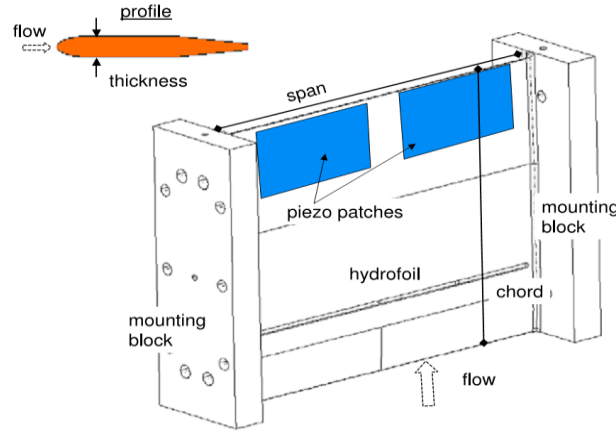


Fig. 5-2 Schematic of the H1 hydrofoil

Table 5-1 Scaled geometries and predicted natural frequencies of the hydrofoils

Hydrofoil	c/c_0	s/s_0	t/t_0	f_s (Hz)	f_{sw} (Hz)	f_{sw}/f_s
H0	1.00	1.00	1.00	226	74.9	0.331
H1	1.00	1.00	0.97	217	71.0	0.327
H3	0.75	1.00	0.79	200	74.1	0.371

5.1. Modal Analysis of Blade without Fluid

The goal of modal analysis is to determine the natural mode shapes and frequencies of the hydrofoil blade during free vibration. The natural frequencies of the blade are dependent only on mass and stiffness of the blade structure and are independent from the load function. The physical interpretation of the eigenvalues and eigenvectors are that they represent the frequencies and corresponding mode shapes. In many practical engineering problems, the only desired modes are those with lowest frequencies because they can be the most prominent modes at which the object will vibrate, dominating all the higher frequency modes. It is also useful to know the modal frequencies of a structure as it allows us to ensure that the frequency of the applied periodic loading will not coincide with a modal frequency and hence cause resonance, which leads to large oscillations.

In the present study, a free vibration analysis of the hydrofoil blade is carried out by using ANSYS 14. The blade is modeled by solid elements (SOLID185 in ANSYS nomenclature) which are suitable for 3-D modeling of solid structures. The element is defined by eight nodes having three degrees of freedom at each node: translations in the nodal x , y , and z directions. The

total number of elements and nodes in the analysis are given in Table 5-2. The fixed-fixed boundary condition of the hydrofoil blade is imposed by deleting all degrees of freedom corresponding to nodes on the blade boundary.

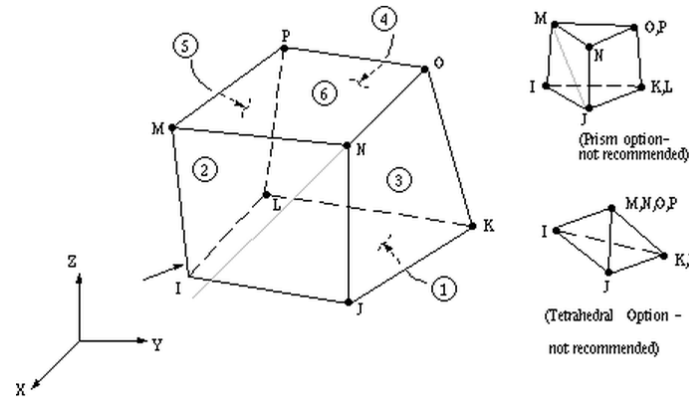


Fig. 5-3 SOLID185 element

Table 5-2 Finite element modeling of the blade

Total number of elements	8047
Total number of nodes	11536

Another higher-order element is also available in ANSYS which is denoted by SOLID186. It is a higher order 3-D 20-node solid element that exhibits quadratic displacement behavior and is well suited to modeling irregular meshes (such as those produced by various CAD/CAM systems). The element may have any spatial orientation. The problem is also solved with SOLID186 (with 20 nodes per element). However, the results obtained using SOLID186 are not presented here for brevity because they were very close to those from SOLID185.

The natural frequencies obtained from the FEM modeling are given in Table 5-3. As it can be seen from this table, they are in good agreement with those previously reported by (Seeley et al., 2012). The first three mode shapes of the problem are also given in Fig. 5-4 to Fig. 5-6. As it can be seen from these figures, the first and third mode shapes of the blade are predominately bending whereas the second mode shape is predominantly torsional.

Table 5-3 Natural frequencies of the blade (Hz) in dry-condition

Mode number	Frequency (Hz)	
	Present Study	(Seeley et al., 2012)
1	218.61	217
2	289.54	-
3	619.68	-

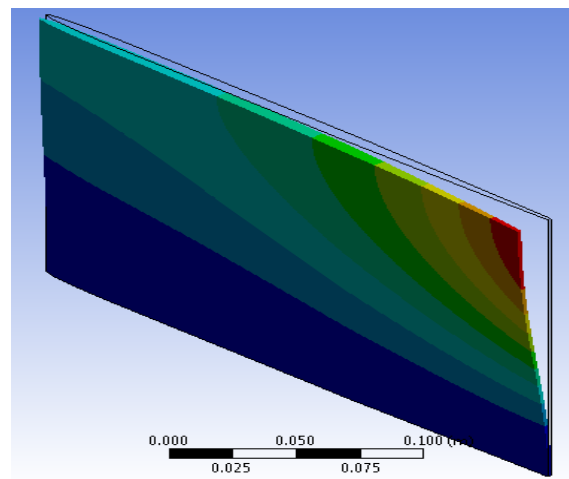


Fig. 5-4 First Mode (218.61 Hz)

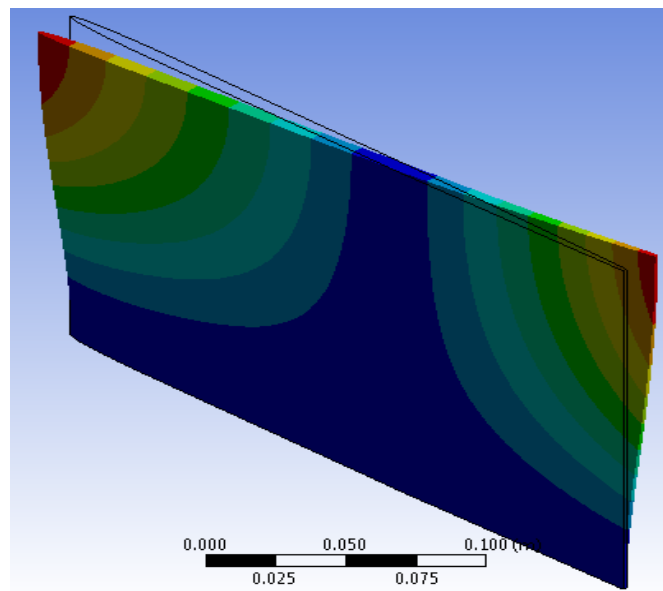


Fig. 5-5 Second Mode (289.54 Hz)

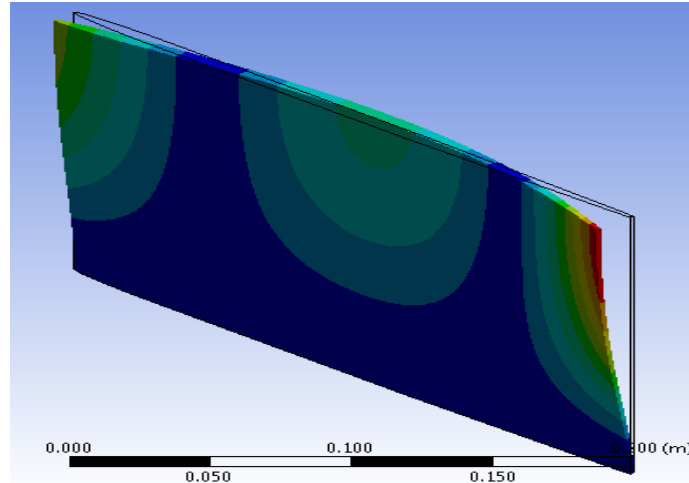


Fig. 5-6 Third Mode (619.68 Hz)

5.2. Transient Analysis of Blade without Fluid

The transient response of the hydrofoil blade is considered in this section when the blade is subjected to several forcing functions as shown in Table 5-4. The forcing function is applied at $t = 0$ and then is removed when $t = t_f$. The magnitude of the forcing function is $F_0 = 60 \text{ N}$. The structural response problem is solved for different values of t_f . Fast Fourier Transform (FFT) is also used to extract the frequency response of the solution.

Table 5-4 Different forcing functions for transient analysis of the hydrofoil blade

Forcing function-a	Forcing function-b	Forcing function-c
Step	Periodic	Increasing

5.2.1. Influence of mesh

Four different mesh sizes are considered to investigate the influence of mesh size. These meshes are indicated as C-mesh, M-mesh, F-mesh and VF-mesh for coarse, medium, fine and very fine meshes, respectively. The transient response of the hydrofoil blade is obtained for forcing function-a with $t_f = 0.9 \text{ sec}$. The forcing function is applied on the centerline of the blade. The frequency response of the solution is obtained by using FFT. The dominant frequency of the

response is obtained from FFT analysis and is given in Table 5-5 for different mesh sizes. This table also shows the maximum response amplitude of the hydrofoil after removing the applied force.

Table 5-5 Influence of mesh

Mesh size	No. of Elements	Frequency (Hz)	Max. Amplitude (mm) (After removing the force)
C-mesh	462	221	0.123
M-mesh	5143	219.7	0.160
F-mesh	8584	219.6	0.164
VF-mesh	14680	219.6	0.164

The computational mesh and z-displacement at midpoint of the trailing edge of the blade for different mesh sizes C-mesh, M-mesh, F-mesh and VF-mesh are shown in Fig. 5-7 to Fig. 5-14.

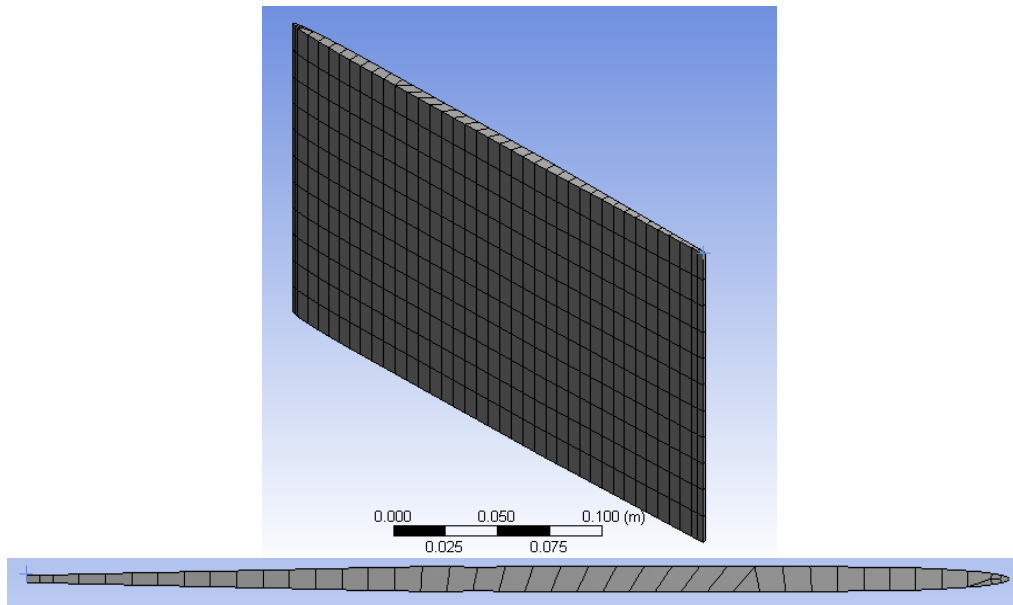


Fig. 5-7 Blade computational mesh (C-mesh)

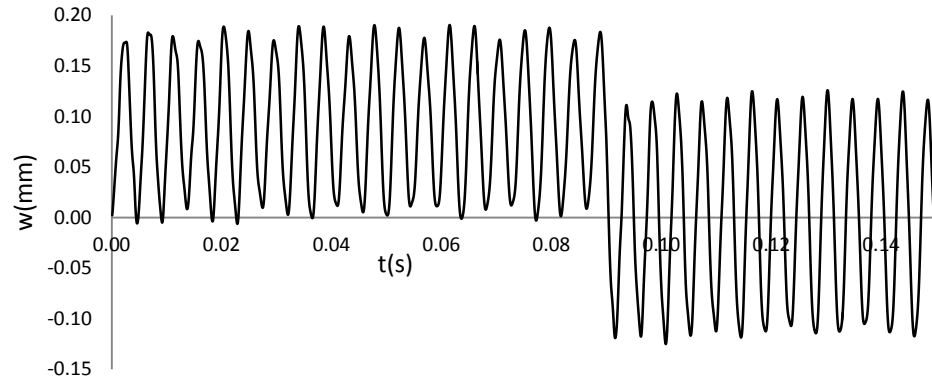


Fig. 5-8 z-displacement at midpoint of the trailing edge of blade (C-mesh, $dt=0.0001$ s)

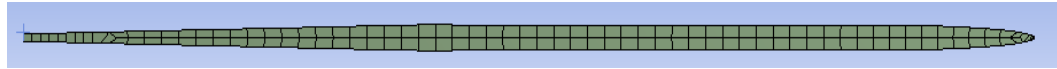


Fig. 5-9 Blade computational mesh (M-mesh)

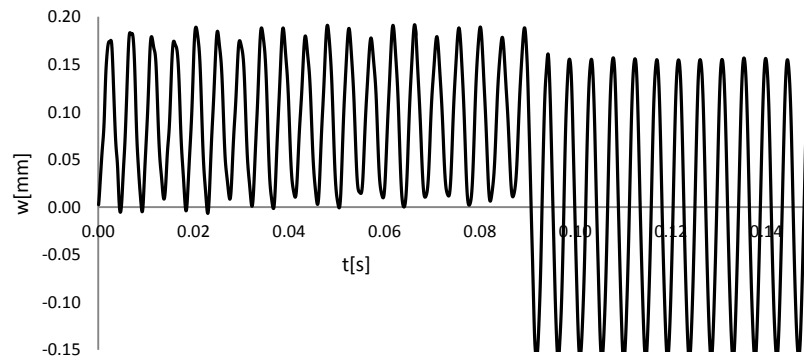


Fig. 5-10 z-displacement at midpoint of the trailing edge of blade (M-mesh, $dt=0.0001$ s)



Fig. 5-11 Blade computational mesh (F-mesh)

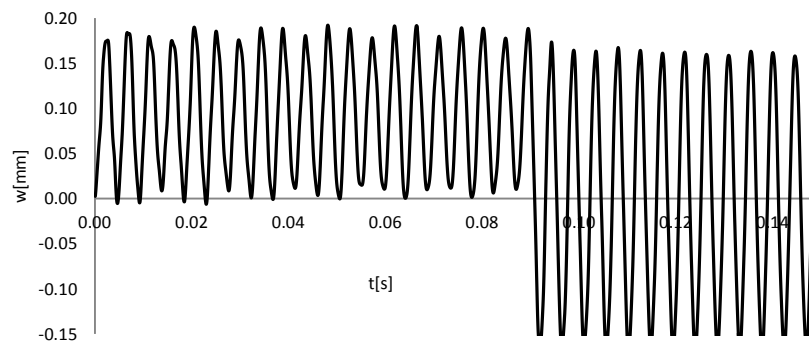


Fig. 5-12 z-displacement at midpoint of the trailing edge of blade (F-mesh, $dt=0.0001$ s)

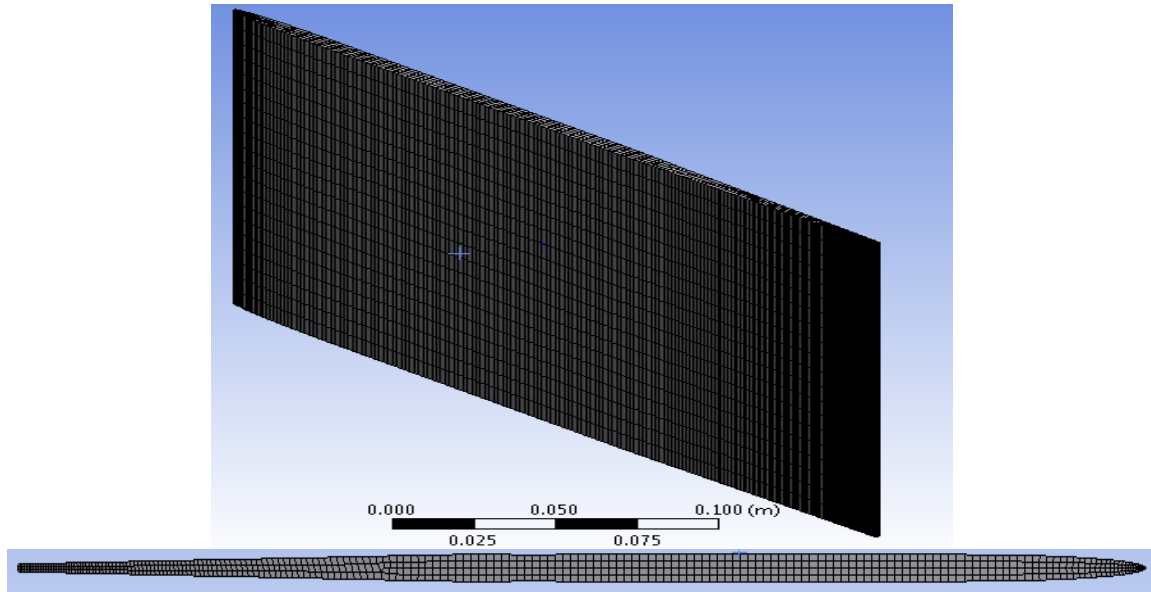


Fig. 5-13 Blade computational mesh (VF-mesh)

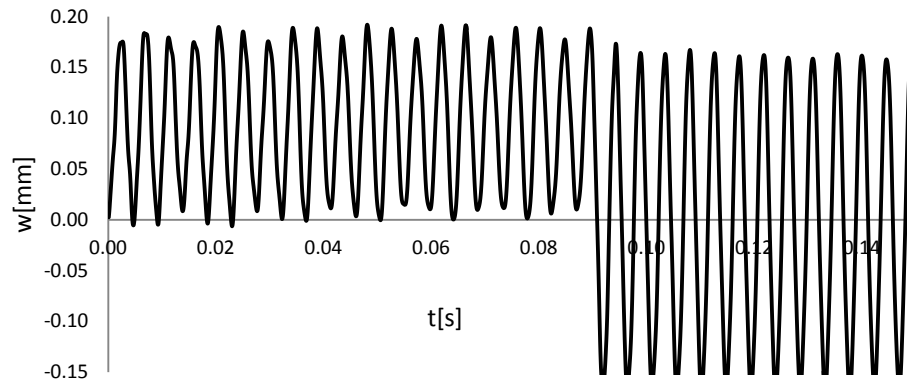


Fig. 5-14 z-displacement at midpoint of the trailing edge of the blade (VF-mesh, $dt=0.0001$ s)

The number of elements for the fine mesh (F-mesh) and very fine mesh (VF-mesh) in the y -direction are 14 and 20, respectively. It can be seen that there is no big difference between the results on the fine mesh with those obtained for the very fine mesh. Moreover, the graphs for z -displacement of the blade trailing edge midpoint are shown in Fig. 5-15 (a, b, c). It can also be seen from these figures that the difference between the fine mesh (8584 elements) and medium mesh (5143 elements) are very small and may be neglected in practical calculations.

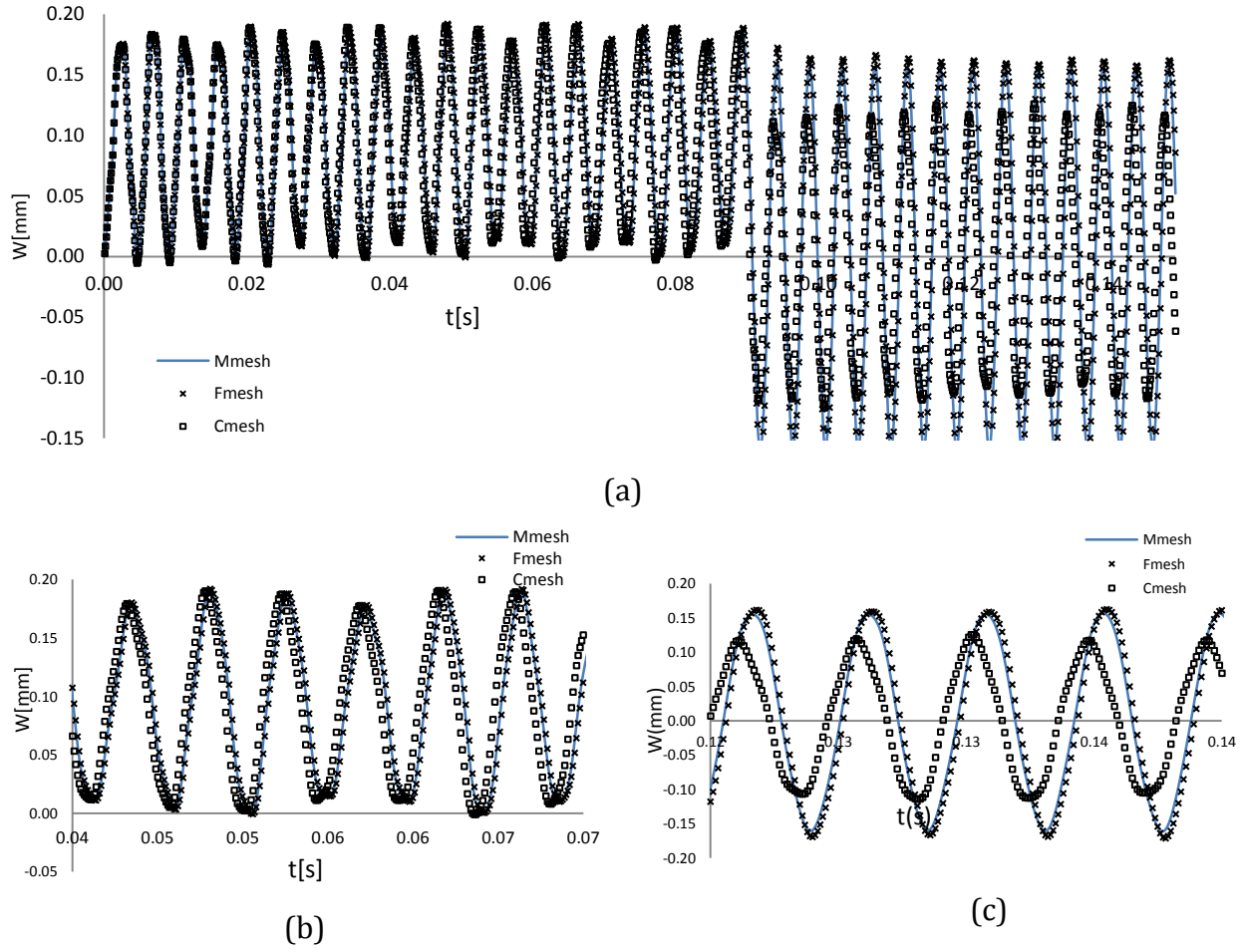


Fig. 5-15 (a) z-displacement at midpoint of the blade trailing edge (For different mesh sizes, $dt=0.0001$ s), (b) Before removing load, (c) After removing load

5.2.2. Influence of Force Application

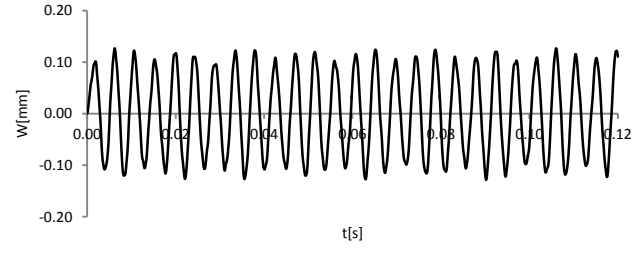
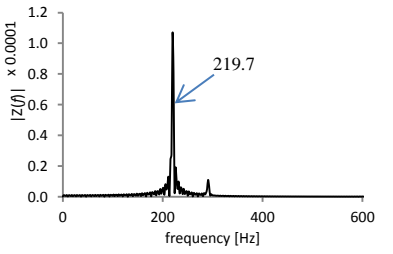
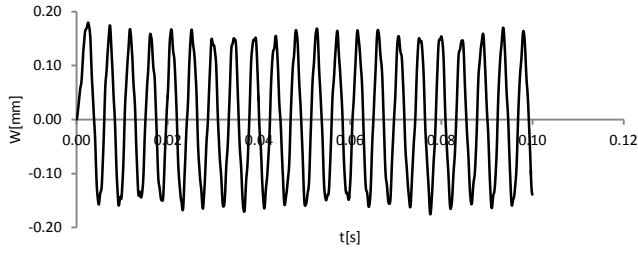
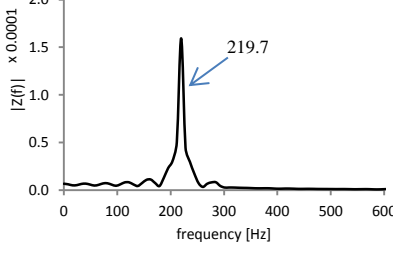
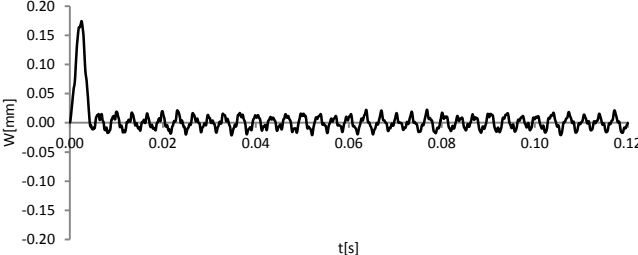
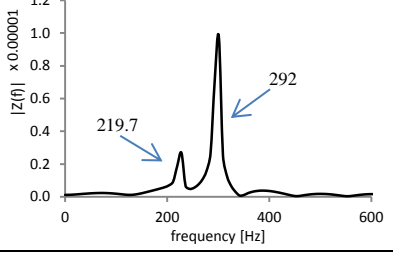
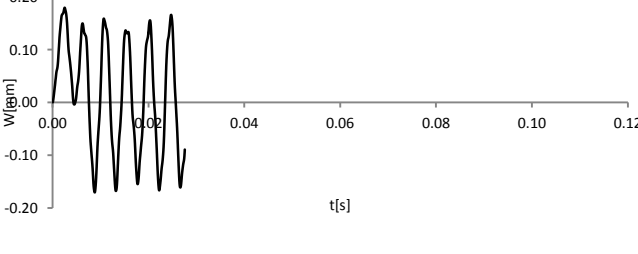
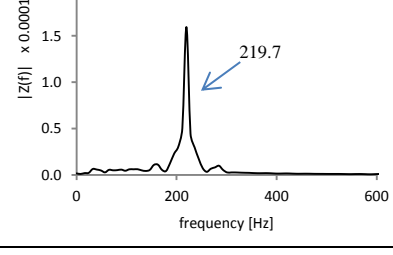
The influence of force application is studied in this section. As shown in Table 5-4, three forcing functions are applied at $t = 0$ and are then removed when $t = t_f$.

a. Step Force

Seven different time durations t_f are considered for the step force, $t_f = 1 \times 10^{-3}$ s, $t_f = 3 \times 10^{-3}$ s, $t_f = 4.5 \times 10^{-3}$ s, $t_f = 6 \times 10^{-3}$ s, $t_f = 9 \times 10^{-3}$ s, $t_f = 4.46 \times 10^{-2}$ s and $t_f = 9 \times 10^{-2}$ s (Table 5-4a). The results of applying these seven step forces are shown in Table 5-6. Considering the shape of the hydrofoil blade and boundary conditions of the problem, we expect the first mode of the blade to be excited due to application of the force. However, our

observations show that the time duration t_f has significant effects on both the mode number being excited and maximum amplitude of the blade fluctuations after removal of the applied load. The effect of time duration t_f will be explained in more details in the following. The frequency content of the response is obtained by using FFT. The FFT of the system response for all t_f are also shown in Table 5-6. The period of the first mode obtained from the modal analysis is $T_s = 4.5 \times 10^{-3} s$.

Table 5-6 Step Force with different time durations (t_f)

		z-displacement at midpoint of the trailing edge of the blade	FFT of the system response
(A)	$t_f = 1 \times 10^{-3} s < \frac{T_s}{2}$		
(B)	$t_f = 3 \times 10^{-3} s < T_s$		
(C)	$t_f = 4.5 \times 10^{-3} s = T_s$		
(D)	$t_f = 6 \times 10^{-3} s > T_s$		

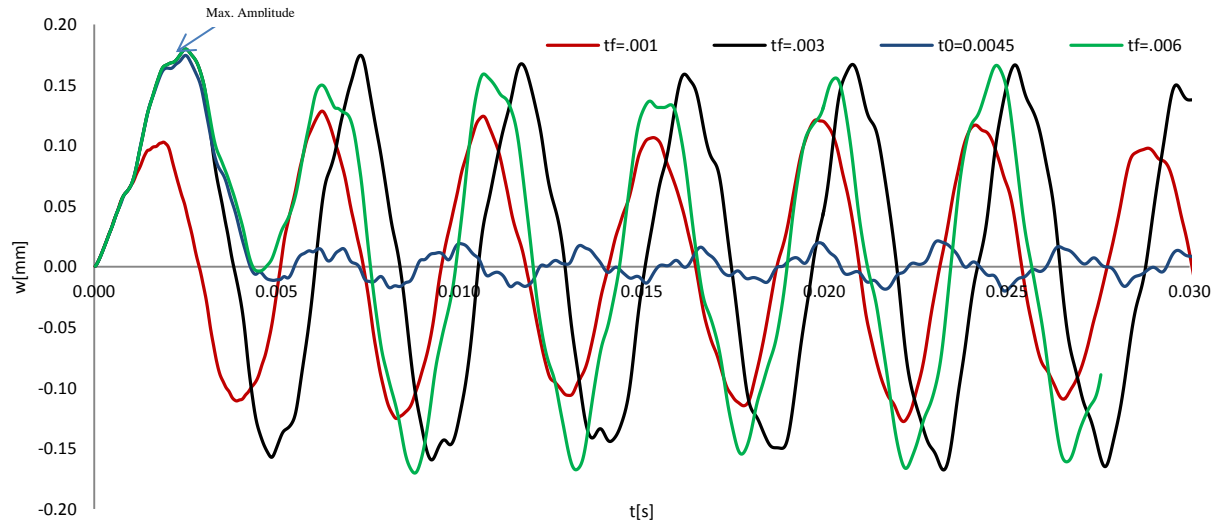
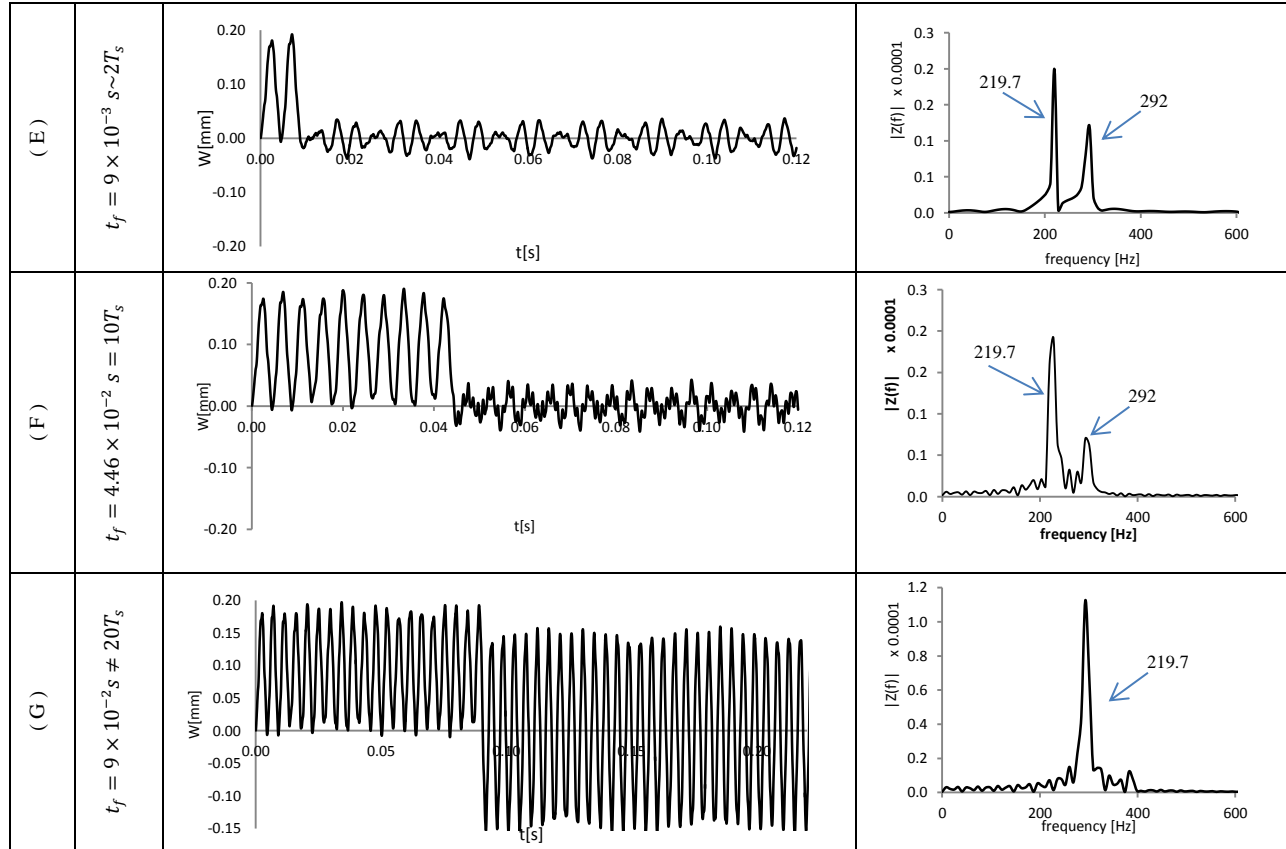


Fig. 5-16. z -displacement at midpoint of the trailing edge of the blade for different t_f

To gain a better understanding of the effect of using different force time durations, z -displacements at midpoint of the trailing edge of the blade are shown in Fig. 5-16. The following conclusions can be drawn from Table 5-6 and Fig. 5-16

- When the time duration t_f is less than half a period ($t_f < \frac{T_s}{2}$), the maximum deflection of the blade increases with increasing the force time duration and reaches the maximum value at $t_f = \frac{T_s}{2}$ (when t_f reaches the value $\frac{T_s}{2}$). (Table 5-6 (A))
- It should be noted that increasing the time duration t_f beyond $\frac{T_s}{2}$ has no effect on the maximum amplitude of the blade vibrations (i.e., the maximum deflection of the blade will remain unchanged) before removal of the applied load.
- For $\frac{T_s}{2} \leq t_f < T_s$, the amplitude of the blade vibrations after removal of the force is greater than the amplitude when the time duration $t_f < \frac{T_s}{2}$. (Table 5-6 (B))
- At $t_f = T_s$, the behavior of blade is completely different. The maximum amplitudes of the blade vibrations after removing the force is very small. It is around 1/5 blade deflection under static force ($F=60\text{N}$). Power spectral densities of the vibration amplitudes obtained by FFT analysis (Table 5-6) for this case shows two dominant frequencies 219.7 Hz and 292 Hz which correspond to the first two natural frequencies of the blade, respectively. Calculating the area under the power spectral density indicates that the main part of the energy of the oscillations is concentrated around these two frequencies 219.7 Hz and 292 Hz. This means physically that the most part of the mechanical energy is attributed to the system around two natural frequencies as we expected from theory of vibrations. Our calculations indicated that 23% of the energy of oscillations is attributed to the system in the frequency range <250 Hz for this loading condition. (Table 5-6 (C))
- We observed similar behaviour when the time duration (t_f) of the applied force is a multiple of natural period ($t_f = nT_s$). (Table 5-6 (C),(E),(F))
- In other cases when $t_f \neq nT_s$, the dominant frequency is the first mode. It can be concluded from this analysis that the second frequency 292 Hz might be ignored in the analysis of the blade under the unit step function with $t_f \neq nT_s$ (n is a natural number).

b. Periodic Force

We found in the previous subsection that the first mode of vibration can be excited by applying a unit step force with $t_f = 9 \times 10^{-2} \text{ sec}$. In this subsection, we are going to study the effects of application of a periodic force as given in Table 5-4. A periodic force with frequency equal to the first fundamental frequency of the blade is considered. The time duration of force application is considered as two periods of vibrations ($t_f = 1 \times 10^{-2} \text{ s}$) to avoid resonance. The applied force is then removed to investigate the free vibration of the blade. The results of the analysis for the z -displacement at midpoint of the trailing edge of the blade and FFT of the system response are shown in Fig. 5-17. It can be seen from Fig. 5-17b that after releasing the periodic force, the system has been excited in the first fundamental frequency 219.7 Hz. Moreover, our calculations showed that 62% of energy of oscillations is attributed to the system for frequencies less than 250 Hz.

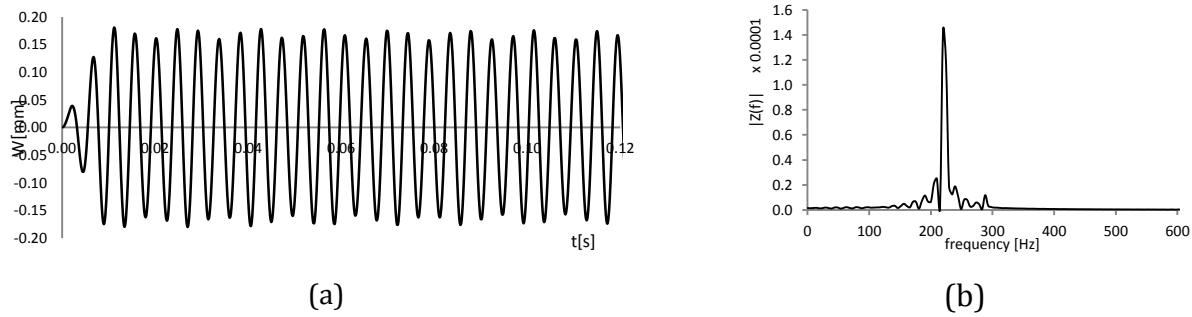


Fig. 5-17 (a) z -displacement at midpoint of the trailing edge of the blade (b) FFT of the system response

c. Increasing Force

The applied force is considered to be an increasing function as shown in Table 5-4c. The force is increased from $F=0 \text{ N}$ at $t=0 \text{ s}$ to $F= 60 \text{ N}$ at $t=0.01 \text{ s}$ and removed at $t_f = 1.2 \times 10^{-2} \text{ s}$. The results of the analysis for the z -displacement at midpoint of the trailing edge of the blade and FFT of the system response are shown in Fig. 5-18. As it can be seen from this figure, the system is excited with the first fundamental frequency 219.7 Hz.

We can conclude from our analysis that using either a periodic force or increasing force can excite the first fundamental frequency of the system with approximately the same time duration of force application. However, in the case of periodic force we need to know the (fundamental) first mode frequency of the system prior to the analysis otherwise, another mode of the system could be excited.

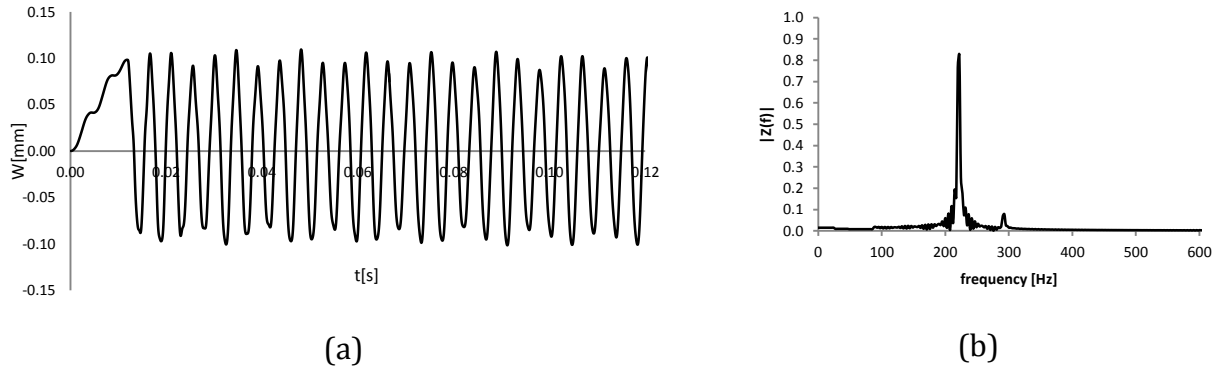


Fig. 5-18(a) z-displacement at midpoint of the trailing edge of the blade (b) FFT of the system response

5.2.3. Influence of Force Position

The forcing function (c) has been applied at the leading and trailing edges (in opposite directions) instead of at the center line of the blade (Fig. 5-1). The z-displacement at midpoint of the trailing edge of the blade and FFT of the system response for different magnitude of forces applied to leading edge (F_L) and trailing edge (F_T) are shown in Fig. 5-19 to Fig. 5-22 .

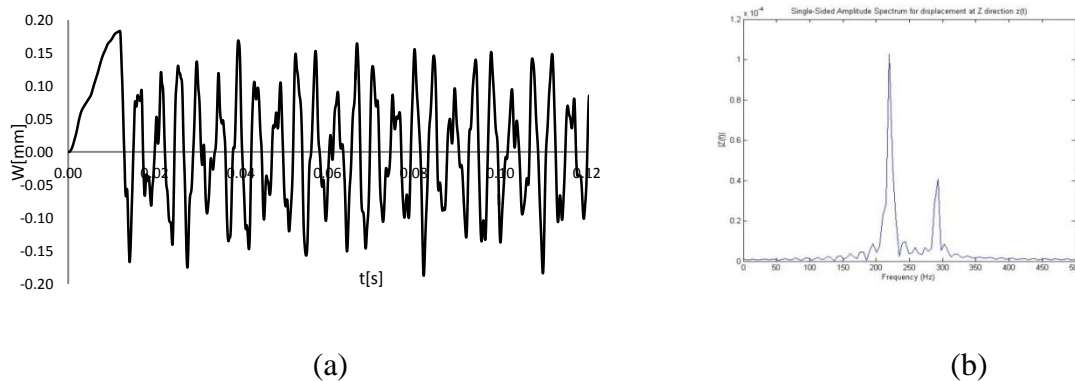


Fig. 5-19 (a) z-displacement at midpoint of the trailing edge of the blade ($F_T=60$ N, $F_L=0$ N)
(b) FFT of the system response

It is interesting to note that different modes of vibration have been excited by changing the magnitude and direction of the applied force. As seen from these figures, applying the same force in opposite directions at the leading and trailing edges of the blade can excite the first and the second mode together. However, when the force applied at the leading edge is two times that at the trailing edge and in opposite direction, the second mode of vibration is mainly excited. Our calculations also showed that most of the energy of oscillations is attributed to the system in the second mode. Moreover, applying the force only on the leading edge will excite both the first and the second mode.

Comparing the time domain responses of the vibration amplitudes given in Fig. 5-19(a) to Fig. 5-22(a) indicates that considerable variations in the peak values of the time domain response of the vibration amplitudes can be seen when the second mode of vibration has been excited. Moreover, the variations in peak values of the responses are more considerable for the cases when the second mode of the vibration is more dominant in the FFT analysis of the response.

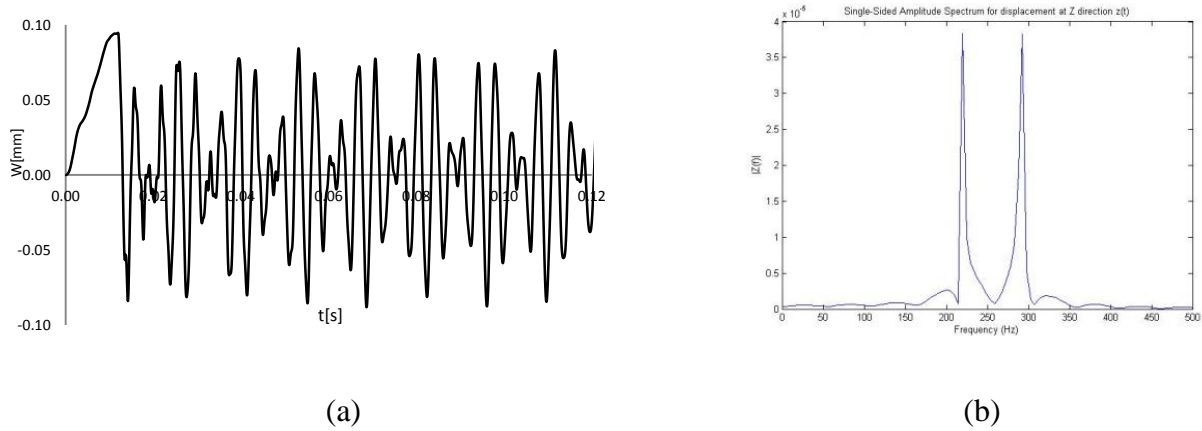


Fig. 5-20 (a) z-displacement at midpoint of the trailing edge of the blade ($F_T=30\text{N}$, $F_L=-30\text{N}$)
(b) FFT of the system response

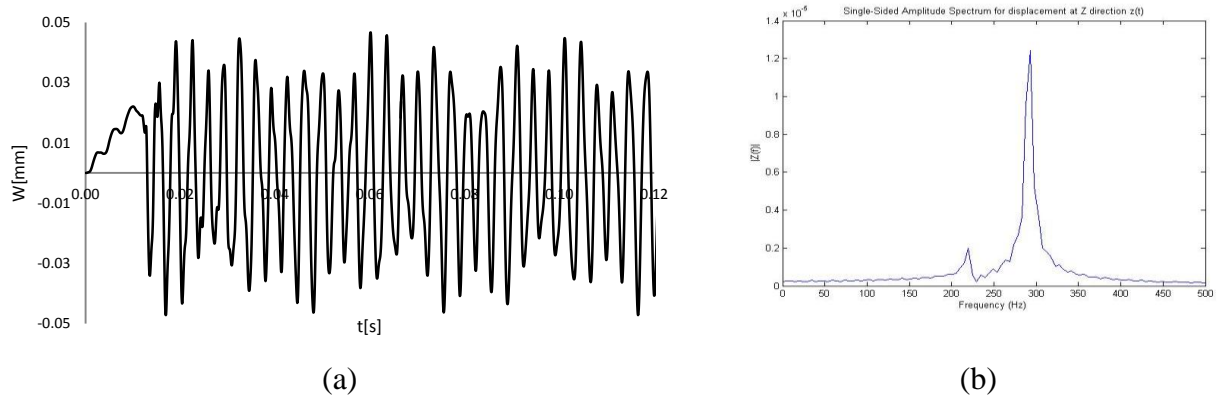


Fig. 5-21 (a) z-displacement at midpoint of the trailing edge of the blade ($F_T=15\text{N}$, $F_L=-30\text{N}$)
(b) FFT of the system response

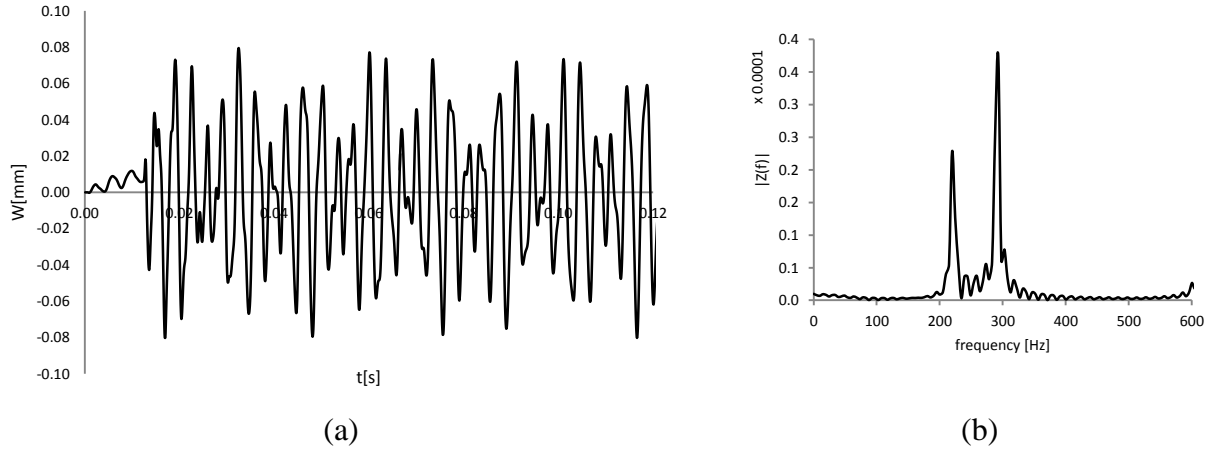


Fig. 5-22 (a) z -displacement at midpoint of the trailing edge of the blade ($F_T=0$ N , $F_L=-60$ N)
(b) FFT of the system response

5.2.4. Time-step study

It is well known that the value of time step may have considerable effect on the solution. In this section, we try to find an appropriate time step for the problem. The forcing function-a (step force) as given in Table 5-4 is used in all calculations in this subsection with $t_f = 9 \times 10^{-2}$ sec. The results for dominant frequencies are given in Table 5-7. The z -displacement of the midpoint of the thin part of the blade is shown in Fig. 5-23 for M-Mesh with $dt=0.001$ sec. It can be seen from this table that the frequency values obtained in the analysis converge to the value of 219.72 Hz for small values of time steps which is very close to the first natural frequency of the system 218.68 Hz from modal analysis. It should also be noted that the z -displacement of the midpoint of the thin part of the blade (Fig. 5-23 and Fig. 5-24) show a decaying rate for time steps 0.001 and 0.0004 which are physically wrong because no damping has been included in the model. In other words, the value of time step must be taken appropriately to get correct results in the analysis. The results of the analysis for smaller time steps 0.0001, 0.00004 and 0.00003 are also shown in Fig. 5-25, Fig. 5-26 and Fig. 5-27, respectively. No considerable difference between the results for z -displacements at midpoint of the trailing edge of the blade can be seen in these figures indicating that each of these time steps (or equivalently 46, 114 or 153 time steps per oscillation period) can be used to solve the problem.

Table 5-7 Dominant frequencies and maximum amplitude of blade vibrations
for different time steps

Time step (s)	Frequency (Hz)	Max. Amplitude (mm) (After removing the force)
0.001	189	0.07
0.0004	209	0.106
0.0001	219.7	0.160
0.00003	219.72	0.160

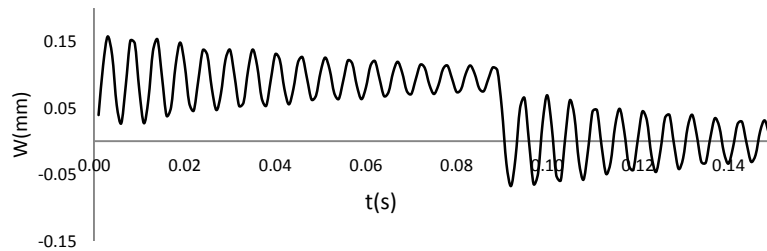


Fig. 5-23 z-displacement of the midpoint of the thin part of the blade M-Mesh , $dt=0.001$ s
(5 time steps per oscillation period)

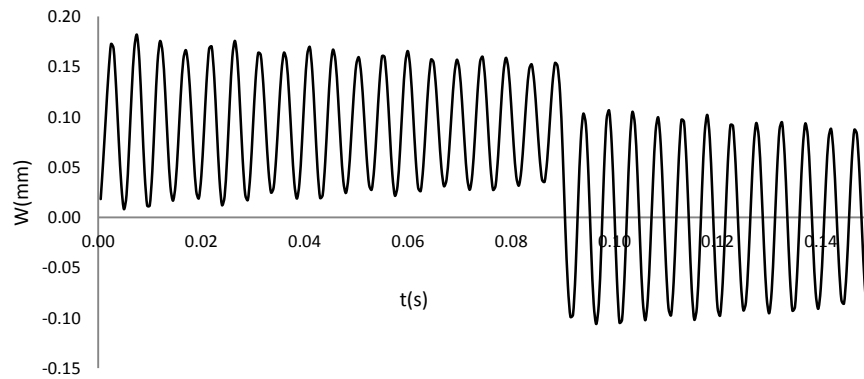


Fig. 5-24 z-displacement at midpoint of the trailing edge of the blade M-Mesh , $dt=0.0004$ s
(12 time steps per oscillation period)

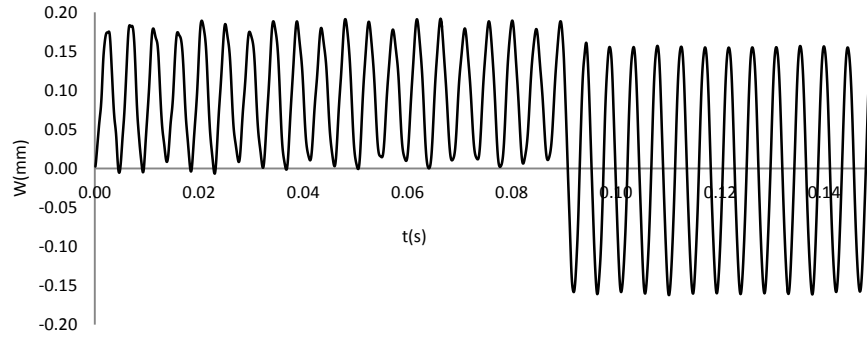


Fig. 5-25 z-displacement at midpoint of the trailing edge of the blade M-Mesh , $dt=0.0001$ s
(46 time steps per oscillation period)

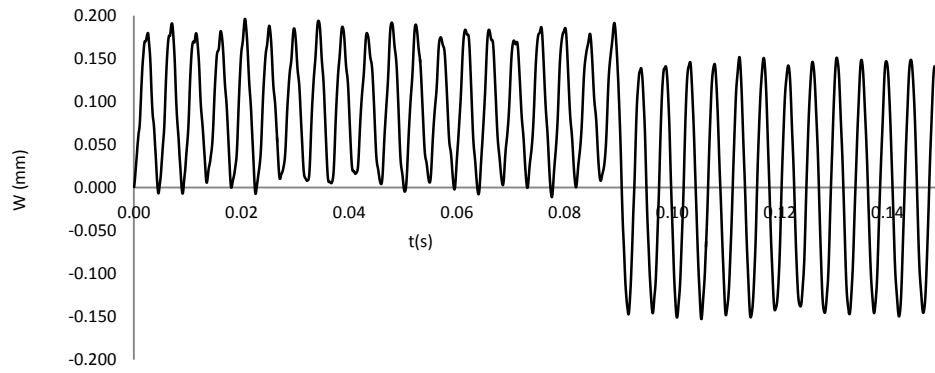


Fig. 5-26 z-displacement at midpoint of the trailing edge of the blade M-Mesh , $dt=0.00004$ s
(114 time steps per oscillation period)

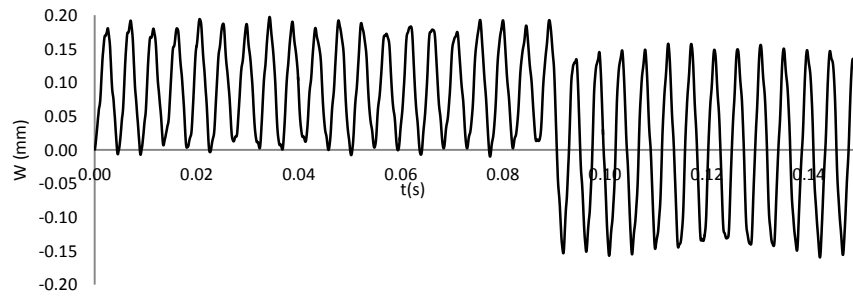


Fig. 5-27 z-displacement at midpoint of the trailing edge of the blade M-Mesh , $dt=0.00003$ s
(153 time steps per oscillation period)

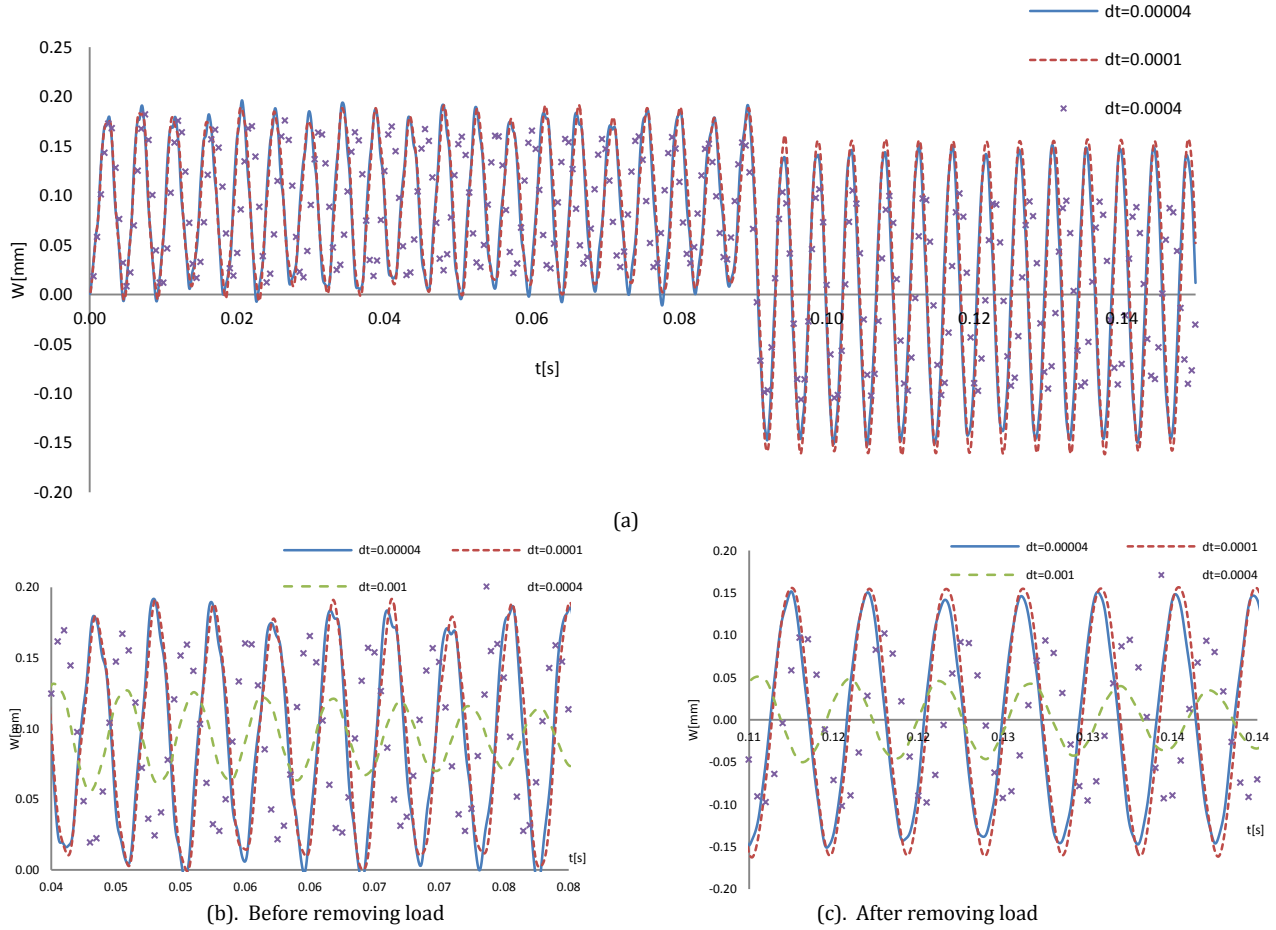


Fig. 5-28 z-displacement at midpoint of the trailing edge of the blade (For different time steps)

To gain a better understanding of the effect of using different time steps, z -displacements at midpoint of the trailing edge of the blade are shown in Fig. 5-28 for different values of time steps for forcing function (a) and $t_f = 9 \times 10^{-2}$ s. It is interesting to note that no considerable difference can be seen between the results obtained for the time steps less than 0.0001 s. Moreover, our analysis showed that using smaller time steps does not change the results obtained for the vibration amplitudes and frequencies and in all these cases, only the first mode of vibration has been excited. The situation is different if the forcing function can also excite the second mode of vibration (i.e., for forcing function (a) and $t_f = 9 \times 10^{-3}$ s). In such cases, the presence of the second mode of vibration for time step 0.0001 cannot be observed in the analysis. However, the analysis with smaller value for the time step indicates that the second mode of vibration is present and is actually excited and must be taken into account in the analysis. This

behavior can be seen from the FFT analysis given in Fig. 5-29 for $\Delta t=0.0001$ s and $\Delta t=0.00003$ s (for forcing function (a) with $t_f = 1 \times 10^{-3}$ s).

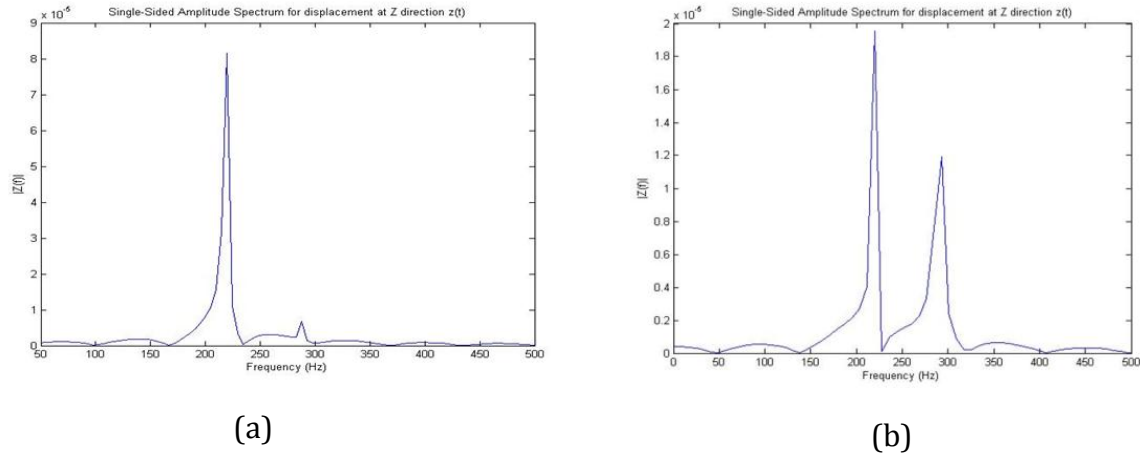


Fig. 5-29 FFT of the system response (a) $\Delta t=0.0001$ s (b) $\Delta t=0.00003$ s

5.3. Transient Analysis of Blade with Fluid (FSI)

Our main objective in this thesis is to find the natural frequency of mechanical vibration of hydrofoil blade in contact with water. We are also aiming to find the effect of considering fluid-structure interaction in estimating the damping parameter in the vibration analysis of the blade and comparing the results with experiment.

The rest of this section is divided into four subsections to investigate the main influences of considering the interaction between the fluid and structure in the dynamic analysis of the blade-fluid system and evaluating the blade natural frequencies,

- Influence of force application to investigate the effects of considering different forces (step force, periodic force, increasing force),
- Influence of mesh
- Influence of time step
- Influence of fluid velocities ($v=0, 3, 6, 9, 12$ and 20 m/s),

The transient analysis is done using the Second Order Backward Euler scheme which is an implicit time-stepping scheme. This scheme is second-order accurate and is generally recommended for most transient runs in ANSYS CFX.

Two methods are used to evaluate the vibration frequency of the blade: (1) averaging the successive oscillation periods obtained from the time-domain response of the z -displacement at midpoint of the trailing edge of the blade and (2) FFT analysis of the z -displacement at midpoint of the trailing edge of the blade. FFT analysis also helps us to obtain a better understanding on the dominant frequency of the blade vibration.

The logarithmic decrement method as explained in Chapter 2 (equation 2-25) is also used to evaluate the damping ratio of the system. We performed our calculations for the damping ratio based on the point to point averaging of the system response and curve fitting approach using $y = y_0 e^{-\xi \omega_n t}$ function. The results from these two approaches were very close to each other and therefore we will only present the results from the curve fitting approach in this chapter.

5.3.1. Flow-induced vibration and influence of considering two-way FSI modeling

For hydraulic efficiency purposes, the hydrofoil blades are relatively slender in the direction normal to the flow and therefore the structural vibrations may be excited by the von Kármán vortices shedding at the trailing edge of the blades. It is worth noting that if the excitation frequency coincides with one of the natural frequencies of the blade, resonance will occur. It may cause vibration and potentially initiate cracks in the blade structure when the amplitude of the excitation force is sufficient. It is well known that the frequency and amplitude of the von Kármán vortices are highly dependent on the free stream velocity and on the trailing edge profile of the blade. In practical applications, it is important not to match the vortex shedding frequency with the blade natural frequency.

To obtain a better understanding of the influence of considering fluid-structure interaction in the analysis of dynamic behavior of the hydrofoil blade and to see if such complicated analysis is actually required from the practical point of view, in this section we compare the results of the transient analysis of the hydrofoil blade by a two-way FSI modeling with those obtained from the analysis of the same problem when the blade structure is assumed rigid. We solved the problem by using fine meshes for the fluid domain with the inlet fluid velocity $v = 6$ m/s (Reynolds number $= 1.7 \times 10^6$) in both cases. Both problems are solved in absence of external forces to see the influence of considering the FSI approach in estimating the fluid forces on the

hydrofoil blade. The results of the analysis for the fluid forces on the hydrofoil blade are presented in Fig. 5-30. As shown in this figure, the fluid forces on the hydrofoil blade evaluated in the FSI analysis are considerably less than the forces estimated on the rigid blade when the interaction of the fluid structure is ignored. It is worth noting that the fluctuating fluid forces have the same frequency in both analyses showing that considering FSI in predicting the frequency of the fluctuating fluid forces in practical problems might be ignored as long as the main concern of the analyzer is to check the possibility of the resonance (lock-in). However, our experience showed that the FSI must be included in the modeling when we aim to predict the influence of the fluid on the damping behaviour in the blade vibration. It should also be noted that running our fluid structure modeling took approximately 35 hours (4 CPU working in parallel) which is considerably higher than the time required for the analysis of the problem when the interaction between the fluid and the hydrofoil blade is ignored. The CPU time required for the solution of the problem when 4 CPU are working in parallel with no interaction between the fluid and structure taken into account was approximately 5 hours.

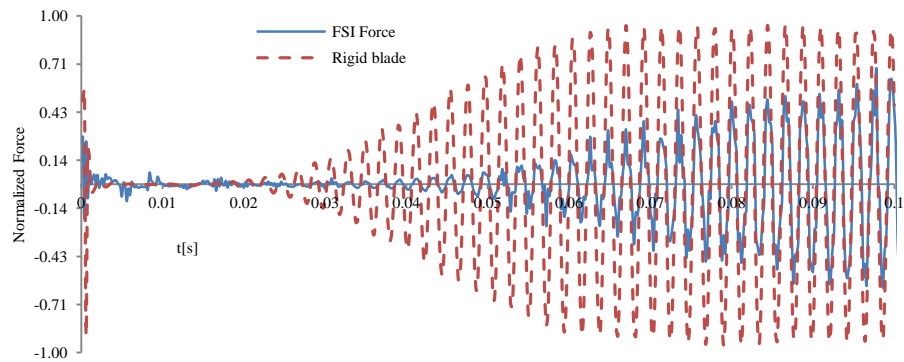


Fig. 5-30 Fluid forces on the hydrofoil blade

The results from the present analysis for the applied forces on the blade due to vortices and their FFT are shown in Fig. 5-31. The velocity contours at the trailing edge of the blade are also given in Fig. 5-32. The dominant frequency of the applied forces on the blade can be estimated as 498 Hz by using FFT. This frequency is far from the fluid-structure natural frequency of the fluid-blade system (~ 71 Hz based on experimental results give in Table 5-1) with a factor of ~ 7 . We can conclude from this comparison that the applied forces due to vortices have small influences on the blade vibration and the risk of lock-in is negligible.

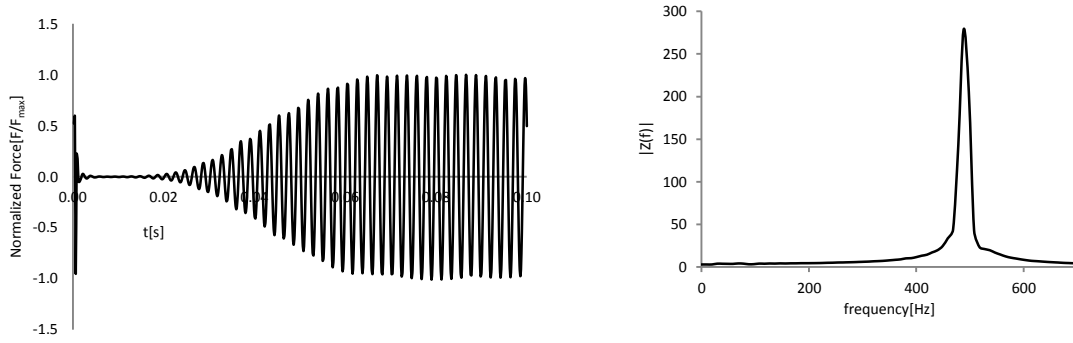


Fig. 5-31 Normalized force on the blade

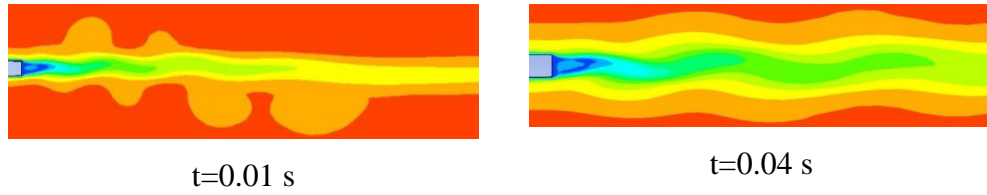


Fig. 5-32 Velocity contour at the trailing edge of the blade

5.3.2. Influence of Force Application

In this subsection, we are going to investigate the effects of considering different types of applied forces on the hydraulic blade. We considered three types of forces including a step force with $t_f = 1 \times 10^{-3} s$ and $t_f = 0.09 s$, a periodic force and an increasing force with $t_f = 0.012 s$ (Table 5-4 and Table 5-8). All forcing functions are applied on the centerline of the blade except for the increasing function which is applied on the centerline of the blade as a first case and on the trailing edge and leading edge as a second case to excite the second vibration mode of the blade. All forcing functions are applied at $t = 0$ and removed at $t = t_f$. Fluid velocity is assumed to be zero in this part and time step is 0.0001 s.

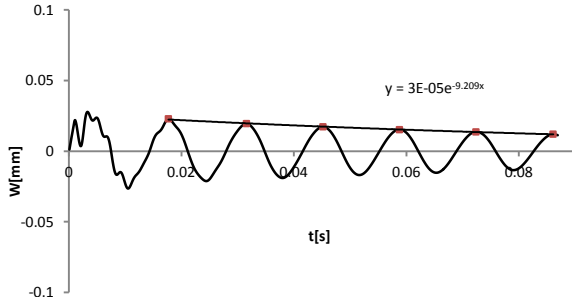
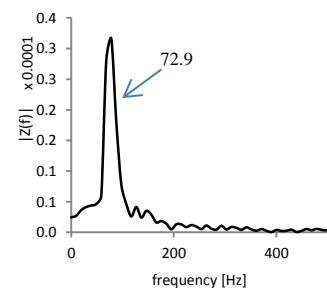
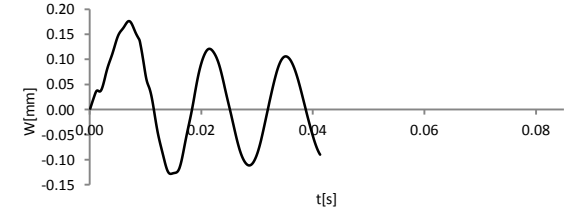
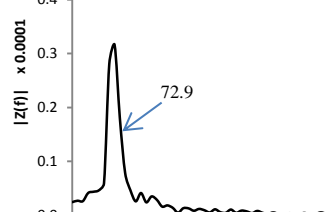
Table 5-8 Three types of forces

	Step Force		Periodic Force	Increasing Force	
	$t_f = 1 \times 10^{-3} s$	$t_f = 0.09 s$		Blade centerline	Blade edges
Response f (Hz)	73.1	72.99	71	72.9	142.8
Damping ratio ξ	0.02	0.02	0.0095	0.0182	0.0167

a. Step force

Five step forces with different force application times $t_f = 1 \times 10^{-3} s$, $t_f = 9 \times 10^{-3} s$, $t_f = 1.36 \times 10^{-2} s$, $t_f = 2.27 \times 10^{-2} s$ and $t_f = 9 \times 10^{-2} s$ are applied on the centerline of the blade. The z -displacement at midpoint of the trailing edge of the blade and the FFT of the blade response for these five step forces are shown in Fig. 5-33 and Table 5-9. Our transient analysis for the blade without fluid (section 5.2.2.a) showed that the time duration t_f has a significant effect on both the mode number being excited and maximum amplitude of the blade fluctuations after removal of the applied load. In this section we consider the transient analysis of the blade with fluid. The effects of time duration t_f are explained in more details in the following. The frequency content of the response is obtained by using FFT. The period of the first mode obtained from the experimental analysis is $T_{FSI} = 1.37 \times 10^{-2} s$.

Table 5-9 Step Force with different time durations (t_f) for blade in water

	z-displacement at midpoint of the trailing edge of the blade	FFT of the system response
$t_f = 1 \times 10^{-3} s < \frac{T_{FSI}}{2}$		
$t_f = 9 \times 10^{-3} s < T_{FSI}$		

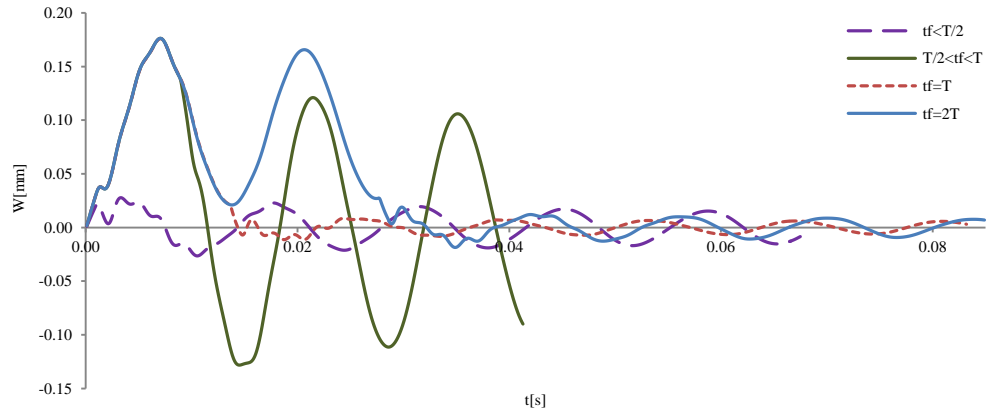
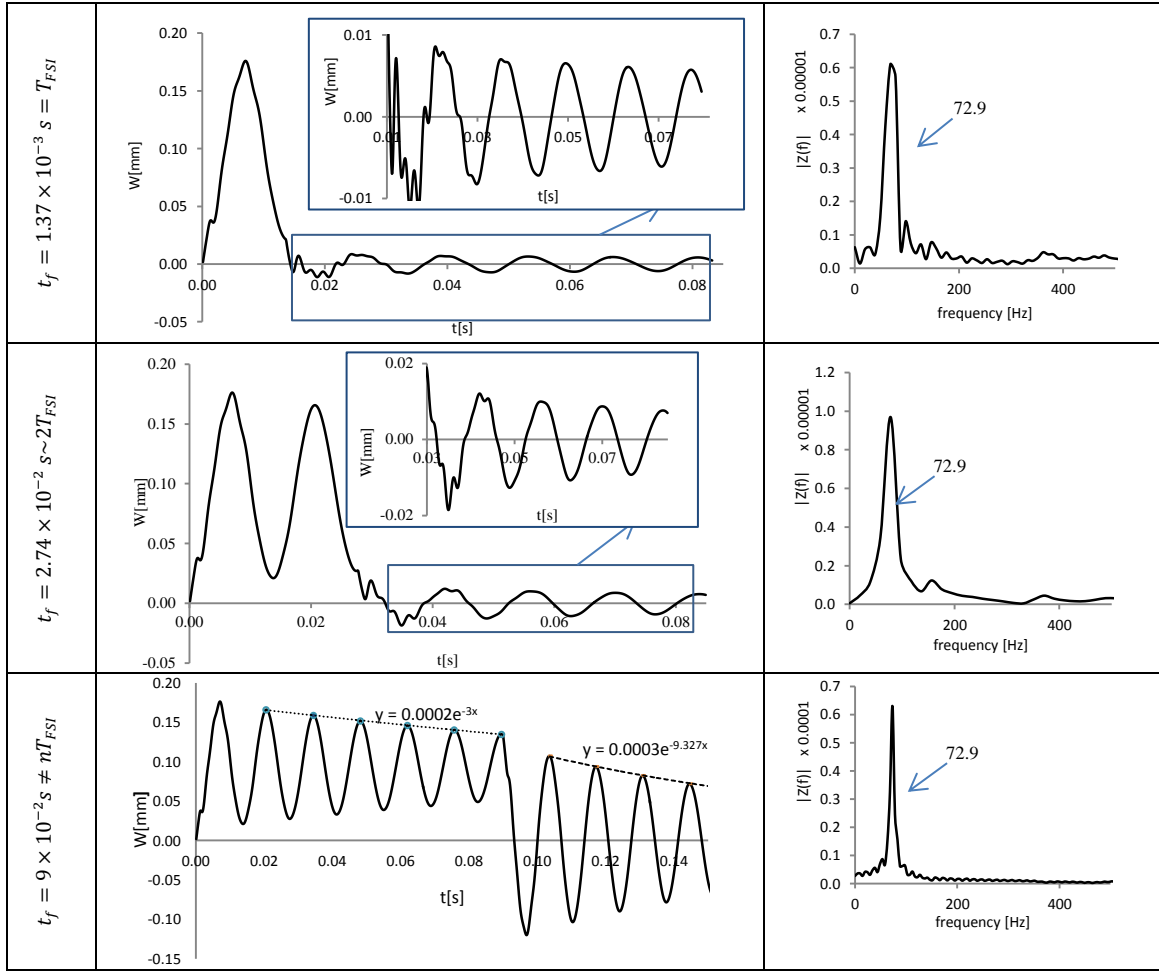


Fig. 5-33 z -displacement at midpoint of the trailing edge of the blade for different t_f

To gain a better understanding of the effect of using different force time durations, z -displacements at midpoint of the trailing edge of the blade are shown in Fig. 5-33. The following conclusions can be drawn from Table 5-9 and Fig. 5-33,

- For $t_f < \frac{T_{FSI}}{2}$, the maximum deflection of the blade in water increases when increasing the time duration of the applied force and reaches the maximum value at $t_f = \frac{T_{FSI}}{2}$. (Table 5-9(A)). This behavior is similar to what we have already seen in section 5.2.2a for the transient analysis of the blade without water. Moreover, we observed that increasing the time duration t_f beyond $\frac{T_{FSI}}{2}$ has no effect on the maximum amplitude of the blade vibrations in water before removal of the applied load.
- For $\frac{T_{FSI}}{2} \leq t_f < T_{FSI}$, the amplitude of the blade vibrations in water (after removal of the force) is greater than for the time duration $t_f < \frac{T_{FSI}}{2}$. (Table 5-9(B)).
- At $t_f = T_{FSI}$, we see a completely different behavior for the blade vibrations. The maximum amplitudes of the blade vibrations in water (after removing the force) is very small. It is worth noting that the vibration response of the blade-water system (after removing the applied force) is combination of different modes of vibrations (with different frequencies) as can be seen from Table 5-9. However and unlike the transient analysis of the blade vibration without fluid, the vibration modes with higher frequencies will be damped rapidly in this case when the effects of water are taken into account (approximately after one period) and it is only the first fundamental mode of blade vibration (with frequency = 72.9 HZ) that governs the final vibration response of the blade in water.
- We also observed similar behavior when the time duration (t_f) of the applied force is a multiple of the natural period ($t_f = nT_{FSI}$). (Table 5-9 (C),(D))
- In other cases ($t_f \neq nT_{FSI}$), the dominant frequency is the first mode and higher frequencies are of less practical importance in the analysis of the blade in water under the unit step function. It should be noted that we have the same behavior even if ($t_f = nT_s$). In other words, when the effect of the fluid-structure interaction is taken into consideration, it is the period of the blade in fluid (T_{FSI}) that governs the behavior of the blade structure (not the period of the blade alone).

b. Periodic Force

The effects of application of a periodic force as given in Table 5-4 (b) is considered in this subsection. A periodic force with a frequency around the first fundamental frequency of the blade obtained in the experiment is considered. The periodic force $f = 20\sin(2\pi 75t)$ is applied to the blade during 2 time periods $t_f = 0.027\text{s}$. The time duration of force application is considered as two periods of vibrations to avoid resonance. The applied force is then removed to investigate the free vibration of the blade. The results of the analysis for the z -displacement at midpoint of the trailing edge of the blade and FFT of the system response are shown in Fig. 5-34. It can be seen from Fig. 5-34 b that the system has been excited in the first fundamental frequency 71 Hz (based on experimental results). Moreover, our calculations showed that 62% of energy of oscillations is attributed to the system for frequencies less than 90 Hz. The damping ratio is also calculated as $\xi=0.01$.

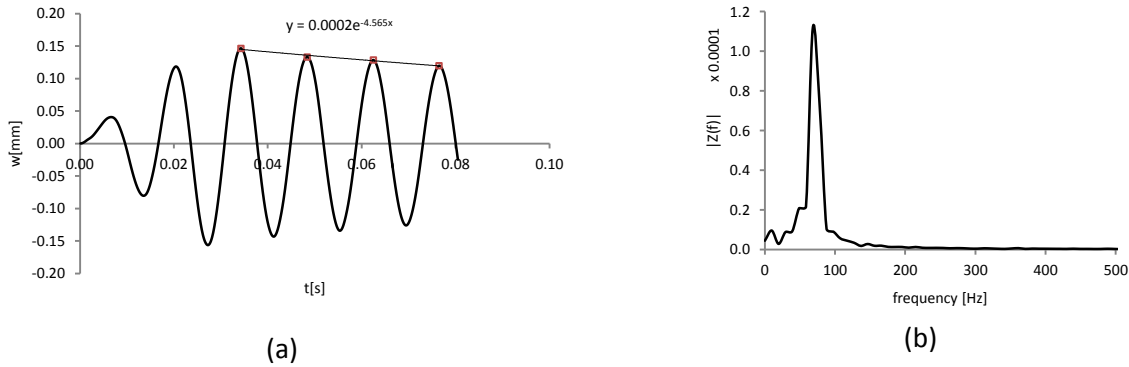


Fig. 5-34 (a) z -displacement at midpoint of the trailing edge of the blade (b) FFT of the system response.

c. Increasing Force

The applied force is now considered to be an increasing function. The force is increased from $F=0\text{ N}$ at $t=0\text{ s}$ to $F=60\text{ N}$ at $t=0.01\text{ s}$ and removed at $t_f = 1.2 \times 10^{-2}\text{ s}$. The results of the analysis for the z -displacement at midpoint of the trailing edge of the blade and FFT of the system response are shown in Fig. 5-35. As it can be seen from this figure, the system is excited with the first fundamental frequency 72.9 Hz. We can conclude from our analysis that using either a periodic force or increasing force can excite the first fundamental frequency of the system. However, in the case of periodic force we need to know the (fundamental) first mode

frequency of the system prior to the analysis otherwise, another mode of the system could be excited. The damping ratio is calculated in this case as $\xi=0.019$.

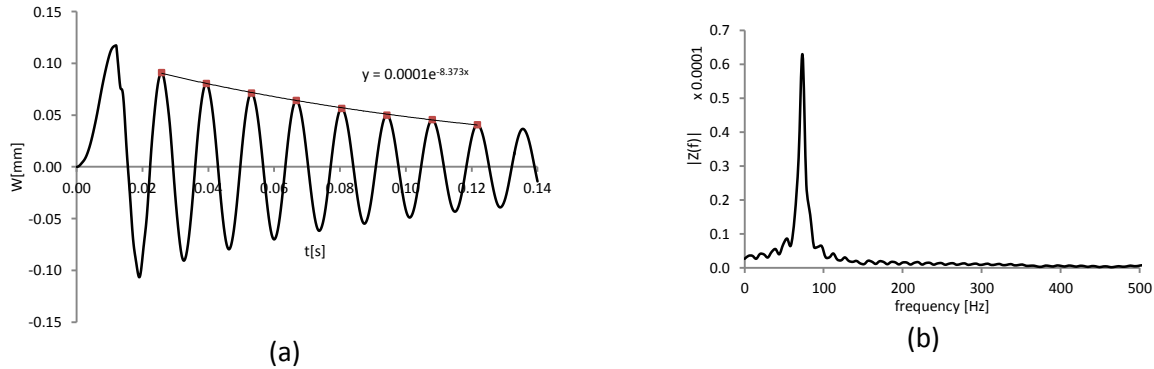


Fig. 5-35 (a) z -displacement at midpoint of the trailing edge of the blade (b) FFT of the system response for $t_f = 0.012 \text{ sec}$

It should be noted that as we have already mentioned in (5.3.2a), the response of the system to the step force depends strongly on the duration of the force application. Moreover, for the periodic force application, we observed that we need to know the fundamental period of the system if we want the system to be excited in its first fundamental frequency. Our observations showed that the response of the system is less sensitive to the duration of the force application when we use an increasing force function. Therefore, we use the increasing force function in the following sections in investigating the influence of other parameters.

5.3.2.1 Influence of Force Position

In subsection 5.2.3, we applied the forcing function at the leading and trailing edges (in opposite directions) and we found that different modes of vibration can be excited by changing the magnitude and direction of the applied forces. For example, we excited both the first and the second modes of the blade by applying equal forces in opposite directions at the leading and trailing edges of the blade, respectively. However, when the applied force on the leading edge was two times that at the trailing edge and in opposite directions, the second mode of vibration was excited and most energy of oscillation was also attributed to the system in the second mode.

To excite the second vibration mode in this part of the analysis, the increasing forcing function (c) with $t_f = 0.012 \text{ sec}$ is applied at the leading (F_L) and trailing edges (F_T) in opposite directions with $F_L=2F_T$. The z -displacement at midpoint of the trailing and leading edges of the blade and FFT of the system response are shown in Fig. 5-36.

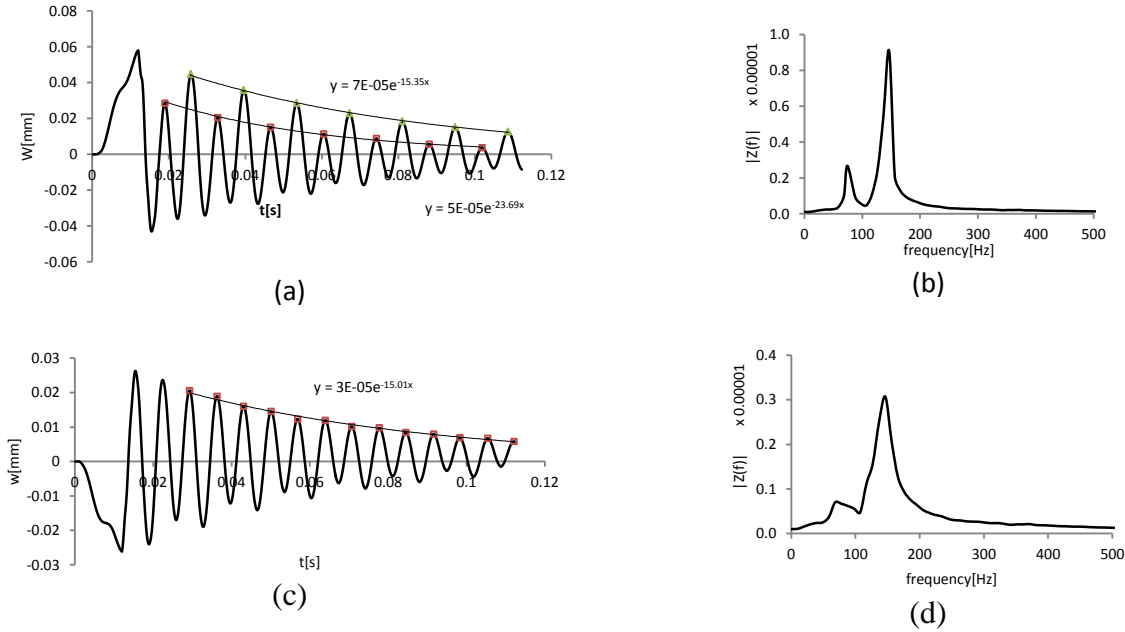


Fig. 5-36 $F_T=15\text{ N}$, $F_L=-30\text{ N}$ (a) z -displacement at midpoint of the trailing edge of the blade (b)&(d) FFT of the system response (c) z -displacement at midpoint of the leading edge of the blade

As seen from Fig. 5-36, the second mode of vibration is excited with the frequency 142.8 Hz. The damping ratio in this case is also calculated as $\xi=0.0167$. It is also worth noting that as can be seen from Fig. 5-36 (a) and (c), the presence of the both the first and second modes of vibrations in the vibration response of the trailing edge (Fig. 5-36 (a)) is more evident than in the vibration response of the leading edge (Fig. 5-36 (c)).

5.3.3. Influence of mesh

One of the most important issues in creating the appropriate meshes for the fluid and structural domain in a fluid-structure problem is to prevent any misalignment in the meshes for the common interface of the structure and the fluid. The meshes on the interface of the fluid and structural domains do not need in general to match each other node by node. However, if the geometry is offset too much, then the interpolation algorithm will have difficulty in deciding where the interfaces touch and the quantities transferred between the structural part and the fluid domain might not be as desired. Mesh alignment error can be avoided in ANSYS by controlling two parameters “Non-Matching Area Fraction” and “Number of Un-Mapped Nodes”. We would have a problem with misaligned meshes if significant Non-Matching Area Fraction or Numbers of Un-Mapped Nodes are present in the model. It should also be noted that the fluid boundary elements around the blade structure are very important in solving a FSI problem and differences

in element normal directions across the interface can produce twisting on coarse meshes with surface curvature. We have already used four different mesh sizes to investigate the influence of mesh size for transient analysis of a blade without fluid in section 5.2.1. These meshes were indicated as C-mesh, M-mesh, F-mesh and VF-mesh for coarse, medium, fine and very fine meshes, respectively. It has been found that there was no considerable difference between the results on fine mesh with those obtained for the very fine mesh. In this section and to find the transient analysis of the blade with fluid-structure interaction taken into account, three different meshes for the fluid (C-mesh, M-mesh and F-mesh) and two different meshes (F-mesh and VF-mesh) for the blade (all hexahedra) are used. To avoid any mesh alignment error in the model, the values of “*Non-Matching Area Fraction*” and “*Number of Un-Mapped Nodes*” are kept to less than 0.1% and equal to zero, respectively. Moreover, we use F-mesh for the blade structure when using C-mesh or M-mesh for the fluid and VF-mesh for the blade structure when we use F-mesh in the fluid domain.

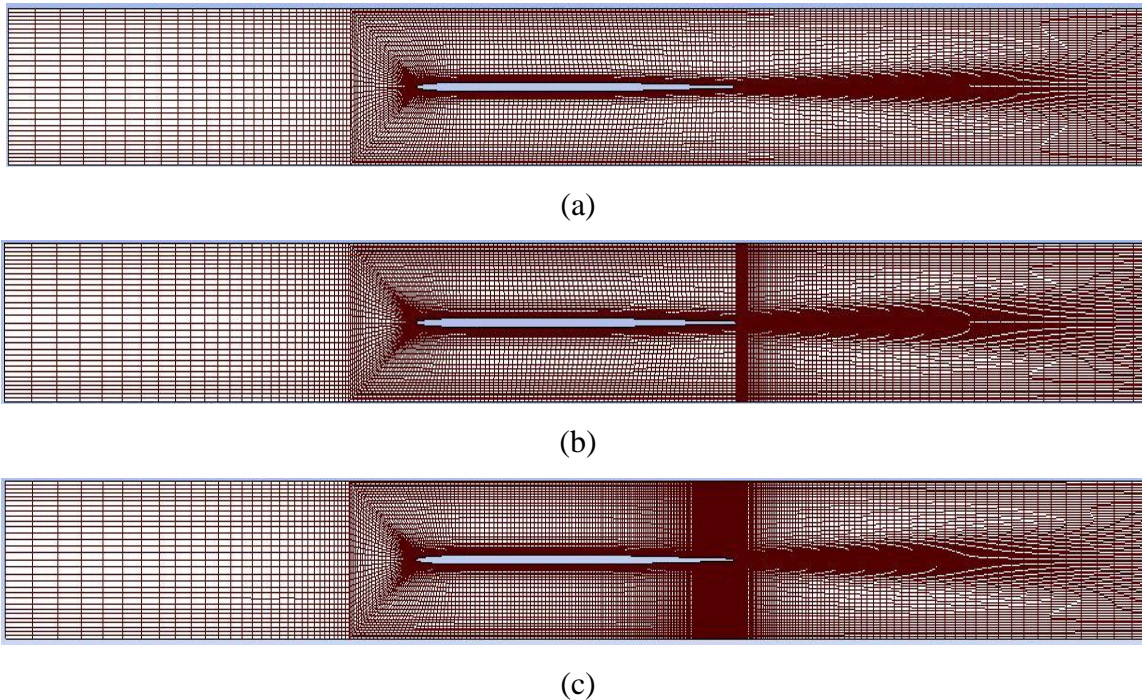


Fig. 5-37 Different Fluid Meshes (a) C-mesh (b) M-mesh (c) F-mesh

Table 5-10 Three different fluid meshes ($V=6$ m/s, $dt=0.0004$)

Mesh size	C-mesh	M-mesh	F-mesh
No. of Elements(Fluid)	228000	363000	567000
No. of Elements(solid)	8584	8584	14680
Response frequency (Hz)	72.9	71.42	72.4
Damping ratio ξ	0.094	0.085	0.09
Max. Amplitude (mm)	0.112	0.118	0.118
Y+ [profile](Ave./Max)	37.49/526	78/121	72/121
CFL (Max/ RMS)	16.03/2.2	9.33/1.58	7.66/1.4
CPU Time (h) for 0.1s	13.5	19	27

Fig. 5-38 shows z -displacement at midpoint of the blade trailing edge for different mesh sizes, with time step $dt=0.0004$ s and inlet velocity $V=6$ m/s.

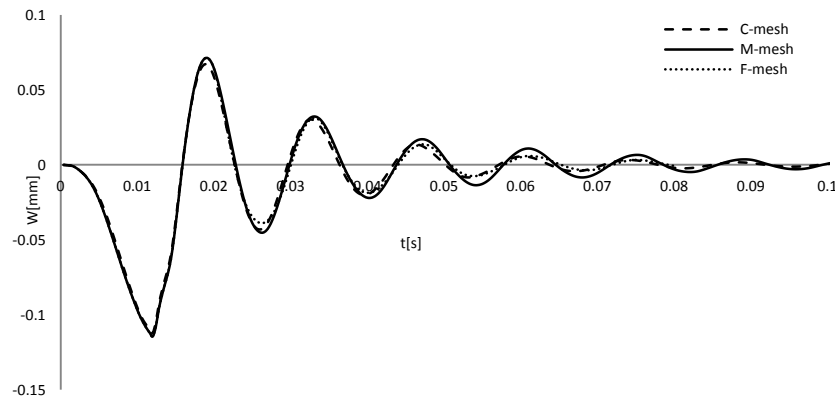


Fig. 5-38 z -displacement at midpoint of the blade trailing edge (For different mesh sizes, $dt=0.0004$ s, $V=6$ m/s)

The mesh specification and results of the current simulation with different meshes are also given in Table 5-10 for time step $dt=0.0004$ s. As can be seen from this table and Fig. 5-38, the results of the simulation with the medium meshes are very close to those obtained with fine meshes and it is therefore reasonable to use the medium mesh size in the calculation for this time step. Fig. 5-39 compares the values of damping ratio for different velocities and different mesh sizes with the experimental results (Seeley et al., 2012). It can also be concluded from Table 5-10 and Fig. 5-38 that the results of the calculations for coarse size meshes are also acceptable (for time step $dt=0.0004$ s) when compared with those obtained for medium and fine meshes.

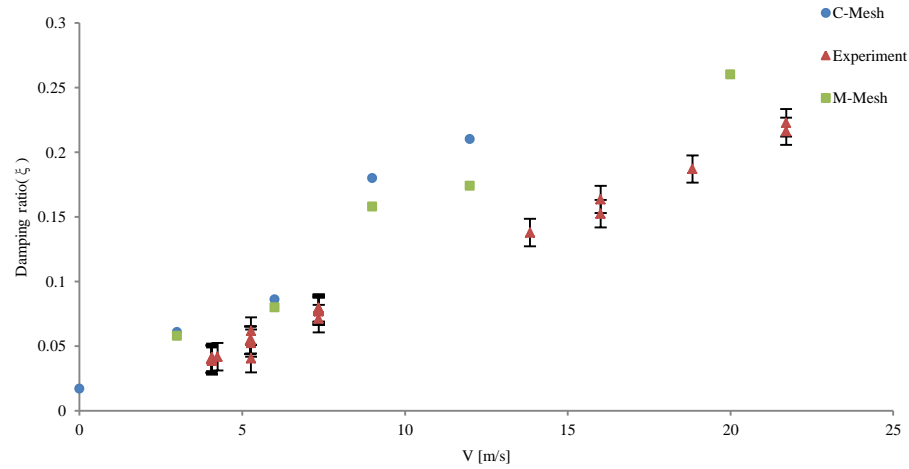


Fig. 5-39 Comparison of damping ratio for different velocities and different mesh sizes with the experiment results ($dt=0.0004$ s)

Comparison of damping ratio for different velocities and different mesh sizes with the experiment results are shown in Fig. 5-39 for $dt=0.0004$ s. This comparison shows considerable differences between the results obtained for the damping ratios for this time step using C-Mesh and M-Mesh with those from the experimental results. To achieve more acceptable results we need to use a smaller time step.

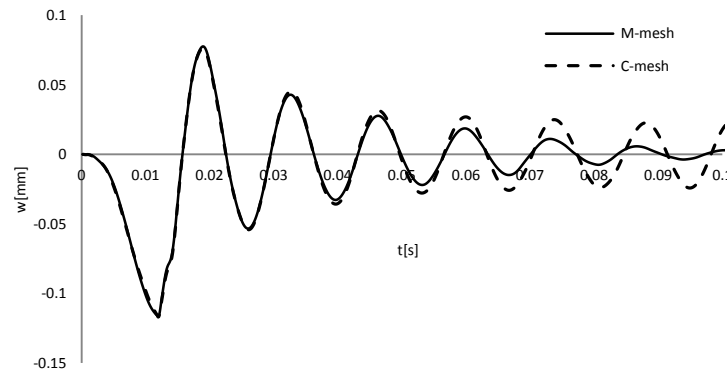


Fig. 5-40 z-displacement at midpoint of the blade trailing edge (For C-mesh and M-mesh, $dt=0.0002$ s, $V=6$ m/s)

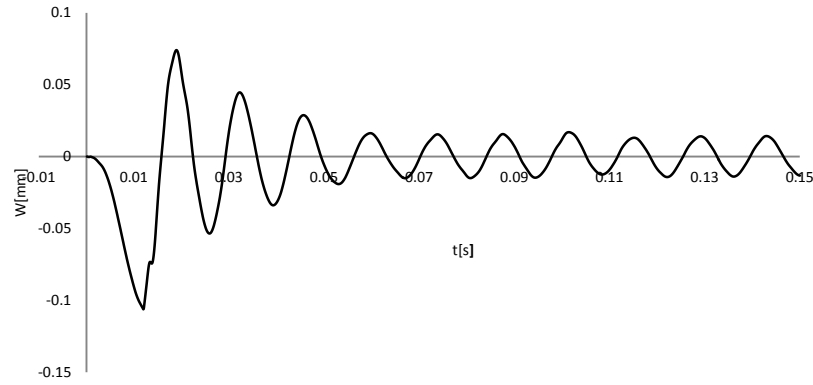


Fig. 5-41 z-displacement at midpoint of the blade trailing edge (For C-mesh, $dt=0.0001$ s, $V=6$ m/s)

We found that selection of mesh sizes depends strongly to the time steps used in the calculations. In our calculations, we reached satisfactory results when we used coarse meshes for $dt=0.0004$ s (Fig. 5-39) whereas using the same meshes for smaller time step $dt=0.0002$ s lead to unacceptable results (Fig. 5-40). The reason for this observation can be explained by noting that at the coarse meshes cannot follow the deformations produced by small time steps. In turn, the damping influence of the fluid cannot be captured appropriately in the analysis when using coarse meshes with small time steps. Similar behavior can also be seen from Fig. 5-41 for the coarse mesh with $dt=0.0001$ s. Our investigations showed that if we keep $V=6$ m/s and reduce the time step to $dt \leq 0.0002$ s, the medium or fine meshes must be used in the calculation to get satisfactory results (Fig. 5-40). However it should be noted that for smaller time steps we need a finer fluid mesh. z -displacements at midpoint of the blade trailing edge are shown in Fig. 5-42 for M-mesh and F-mesh, $dt=0.0002$ s and $V=6$ m/s.

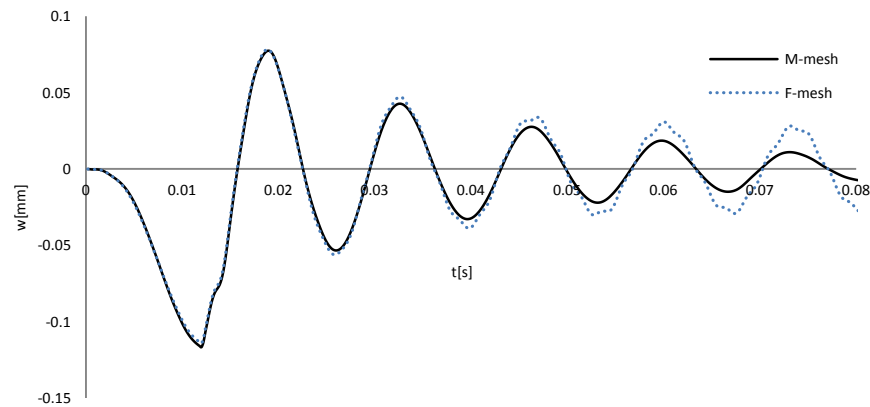


Fig. 5-42 z-displacement at midpoint of the blade trailing edge (For M-mesh and F-mesh, $dt=0.0002$ s, $V=6$ m/s)

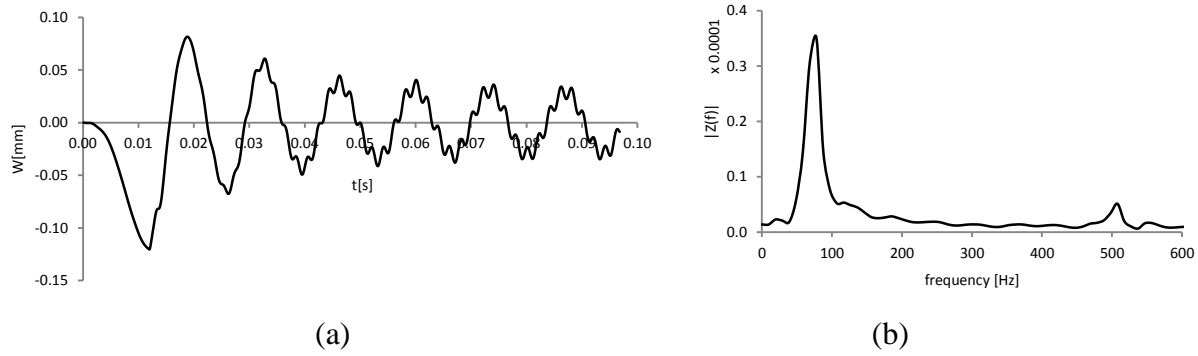


Fig. 5-43(a) z -displacement at midpoint of the trailing edge of the blade (b) FFT of the system response.
(For F-mesh, $dt=0.0001$ s, $V=6$ m/s)

We also noted that if we use fine meshes in the calculations, the effects of the vortices can be captured in the results as shown in Fig. 5-42. This figure shows the effect of the vortices on the vibration of the blade. The presence of the vortices leads to some difficulty in calculating the damping ratio. The influences of using medium and fine meshes are given in Table 5-11 assuming zero external forces on the blade. The normalized forces on the blade, vorticity and velocity contours after the trailing edge are shown in this table for medium and fine meshes. It is worth noting that the forces due to vortex shedding could not be captured when we used the M-mesh. By using the F-mesh, both the applied forces on the blade due to vortex shedding could be captured in the model. It was already shown at the beginning of this chapter that the frequencies of the vortex shedding are large enough to prevent lock-in phenomena. However, the advantages and drawbacks of using F-meshes are as follow:

- Regarding the ability of the F-meshes in capturing the vortex shedding frequencies, a curve fitting approximation algorithm must be used to extract the peak values of the vibration amplitudes of the blade structure. This induces a secondary approximation in our calculation for the frequencies of von Kármán vortices. The presence of the frequency of the vortex shedding in the total response of the hydrofoil blade can be seen more clearly if we reduce the time step to $dt = 0.0001$ s as shown in Fig. 5-43. The total response of the blade in this figure consists of two frequencies to 72.9 Hz and 498 Hz. The frequency 72.9 Hz is the frequency of the vibration of the blade in water under the application of the increasing force as described in section 5.3.2 c. The second frequency (498 Hz) is the vortex shedding frequency. This figure shows that the vibration behavior of the hydrofoil blade in water is similar to what we have seen for the forced vibration of

a mechanical system when an external energy is supplied to the system during the vibration. The source of exciting energy in this case comes from turbulent flow.

- The CPU time for the simulation with medium meshes is significantly less than the corresponding CPU time for the fine meshes. In our calculations, we used 4 CPU in parallel and we needed 128 h and 55 h as the CPU times for F-Mesh and M-Mesh with $dt=0.0002$ s, respectively.
- We obtained damping ratios $\xi \sim 0.052$ (13% error) and $\xi \sim 0.079$ (22% error) by using F-Mesh and M-Mesh, respectively. This indicates that using F-Mesh gives more accurate results when compared with the experimental values.

Table 5-11 Differences between M-Mesh and F-Mesh ($V=6$ m/s)

	M-Mesh	F-Mesh
Normalized force on the blade		
Vorticity at the end of trailing edge		
Velocity contour after trailing edge		

Our experience for the simulation with different inlet velocities indicated that the appropriate mesh size depends also on the inlet velocity. For example, we received no convergence when using coarse meshes for $V=9$ m/s and $dt=0.0002$ s. As shown in Fig. 5-44, fine meshes must be used to obtain acceptable results for this inlet velocity ($V=9$ m/s) and similar behavior are observed for $V=12$ m/s and $V=20$ m/s with $dt=0.0002$ s. In all cases, we need to use fine meshes to achieve reasonable results.

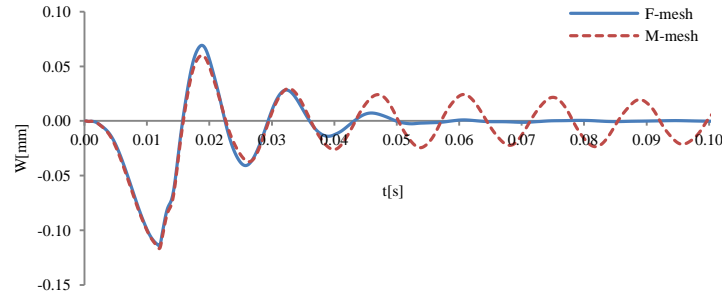
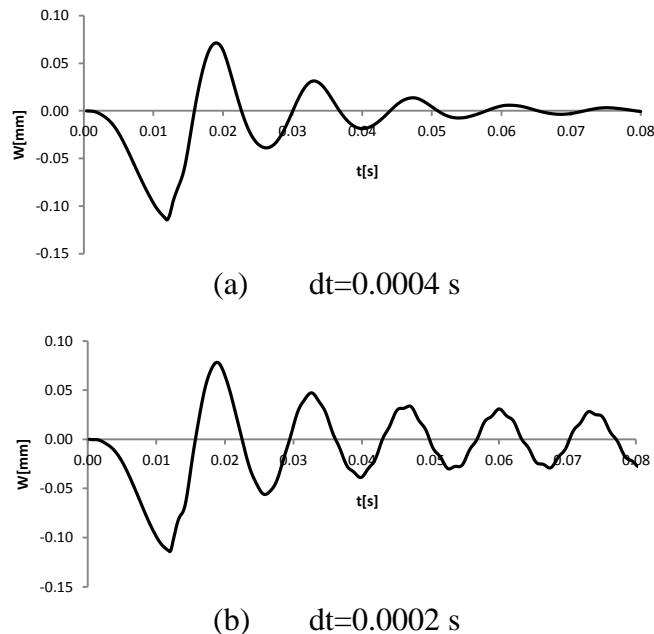


Fig. 5-44 Z-displacement at midpoint of the blade trailing edge (For M-mesh and F-mesh, $dt=0.0002$ ss, $V=9$ m/s)

5.3.4. Influence of time step

The effects of time steps must also be taken into account in the transient analysis. The results for z-displacement at midpoint of the blade trailing edge for the medium mesh with inlet velocity $V=6$ m/s and different time steps are shown in Fig. 5-45.



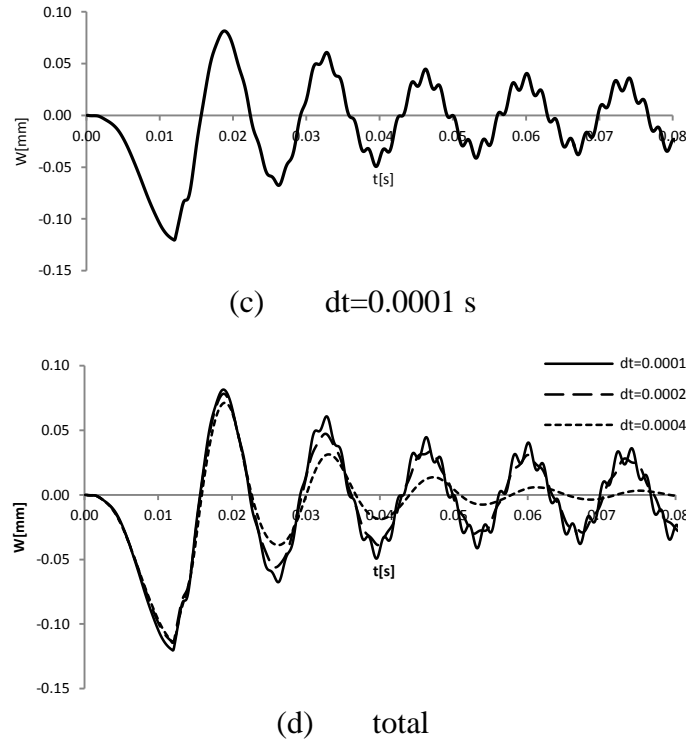


Fig. 5-45 z-displacement at midpoint of the blade trailing edge (M-mesh, different time steps, $V=6$ m/s)

Table 5-12 Three different time step ($V=6$ m/s)

Mesh Size	Time step (s)	Damping ratio (Simulation)	Error (%)	CPU Time (h) for 0.1 s
M-Mesh	0.0004	0.085	31	19
	0.0002	0.079	22	55
	0.0001	0.078	21.5	142
F-Mesh	0.0004	0.09	38	27
	0.0002	0.052	13	128
	0.0001	0.050	15	301

The simulation time for different time steps are given in Table 5-12. It can be seen from this table that halving the time step leads the simulation time to be increased with a factor of more than 2.5. Considering the very small difference between the damping ratios 0.052 and 0.050 calculated for two time steps $dt=0.0002$ s and $dt=0.0001$ s, respectively, the time step $dt=0.0002$ s are used in our calculations.

We have already observed in the previous section that the von Kármán vortices cannot be seen in the analysis if we use medium meshes with $dt=0.0002$ s. It is worth noting that the von Kármán vortices can be captured in the analysis with medium meshes if we reduced the value of time step (i.e., $dt=0.0001$ s). However, Table 5-12 indicates that using fine meshes with $dt=0.0002$ s results in a better estimation for the damping ratio when compared with the medium meshes.

As mentioned above, the problem was solved for several inlet velocities, $V=6, 9, 12$ and 20 m/s. The results from our analysis for time step $dt=0.0004$ s and velocities $V=12$ and 20 m/s, showed only the first mode of the vibration in the system response. However, when we reduced the time step value from $dt=0.0004$ s to $dt=0.0002$ s (at the same velocities), both the first and the second modes can be seen in the response of the system as shown in Fig. 5-46. The deformations of the blade for velocity $V=12$ m/s and time step $dt=0.0002$ s at two different times $t=0.03$ s and $t=0.06$ s are also given in Fig. 5-47. It can be seen from this figure that the deformations of the blade at $t=0.03$ s and $t=0.06$ s are similar to the deformation of the blade in the second and first mode, respectively.

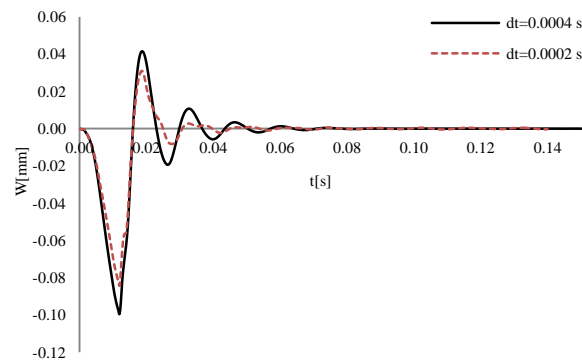


Fig. 5-46 z -displacement at midpoint of the blade trailing edge (For M-mesh, different time step, $V=12$ m/s)

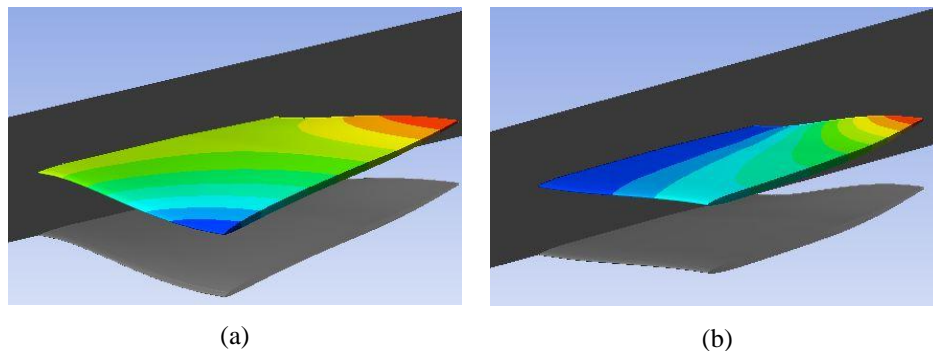


Fig. 5-47 Deformations of the half of blade for $V=12$ m/s, $dt=0.0002$ s at (a) $t=0.03$ s (b) $t=0.06$ s

Table 5-13 CPU time (h) when 4 parallel CPU are working together

Time step	Inlet Velocity											
	V=3m/s			V=6m/s			V=9m/s		V=12m/s		V=20m/s	
	0.0004	0.0002	0.0001	0.0004	0.0002	0.0001	0.0004	0.0002	0.0004	0.0002	0.0004	0.0002
C-Mesh	20.5	N.C.	N.C.	13.5	43.7 [*]	89 [*]	10.4	N.C.	N.C.	N.C.	N.C.	N.C.
M-Mesh	N.C.	56	-	19	55	142 ^{****}	16.8	48 ^{**}	17	N.C.	11	N.C.
F-Mesh	N.C.	N.C.	347	27	128 ^{***}	301 ^{***}	-	119	-	120	18	121

N.C. indicates “No Convergence”

* see Fig. 5-40 and Fig. 5-41 and explanation given in section 5.3.3

** see Fig. 5-44 and explanation given in section 5.3.3

*** see Fig. 5-42 and Fig. 5-43 the explanation given in section 5.3.3

**** see Fig. 5-45c and the explanation given in section 5.3.3

5.3.5. Influence of velocity

It is well known that the vibration amplitudes are inversely related to the damping from the structural components and fluid effects and therefore it is critical to understand the additional damping due to FSI to accurately estimate vibration amplitudes of hydraulic blades. It should be noted that the damping from fluid effects can be considered as one of the most important parameters in controlling the amplitude of the blade vibrations at resonance whereas its effect can even be more critical for the blades with small structural damping and/or high velocity flowing water. In some practical operations, the velocity of water relative to the turbine blades may be as high as 40 m/s (Seeley et al., 2012). Therefore, determining the relationship between damping and water velocity would be of critical interest for understanding potentially dangerous blade vibrations.

To study the effects of considering fluid-structure interaction in estimating the damping parameter in the vibration analysis of the blade and investigating the effects of flow velocity on the damping ratio of the hydraulic blade, the coupled fluid-blade system is considered in this part of the analysis with different flow velocities $V = 0, 3, 6, 7.4, 9, 12$ and 20 m/s. Regarding our observations and conclusions in the previous sections the problem is solved with F-mesh for $V=0, 3$ m/s (with $dt=0.0001$ s) and $V= 6, 7.4, 9, 12, 20$ m/s (with $dt=0.0002$ s). The z-components of the vibration amplitudes at midpoint of the trailing edge of the blade is shown in Fig. 5-48 for different fluid velocities.

The results of this section are also compared with the experimental observations and estimations reported by (Seeley et al., 2012). This comparison indicates that, although the natural frequencies were not substantially affected by the flow, the damping ratios were observed to increase in a linear manner with respect to flow velocity. The following conclusions can be summarized,

- The maximum amplitude of the blade vibration decreases when the fluid velocity is increased (Fig. 5-49).
- The response frequency of the blade decrease with the increasing of the fluid velocity. (Fig. 5-50). This is in agreement with the behavior reported in Wang (2008).
- There is a linear relationship between the damping ratio and the fluid velocity (Fig. 5-51). This conclusion is in agreement with the results reported by Seeley et al. (2012) from the experimental observations.

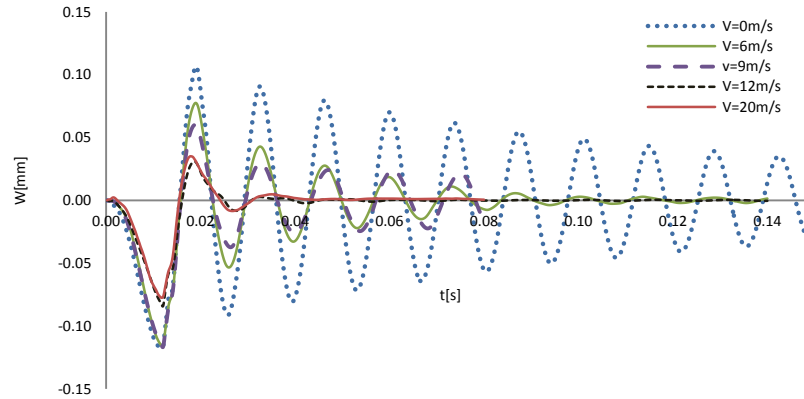


Fig. 5-48 z-displacement at midpoint of the blade trailing edge (For different fluid velocities, $dt=0.0002$ s)

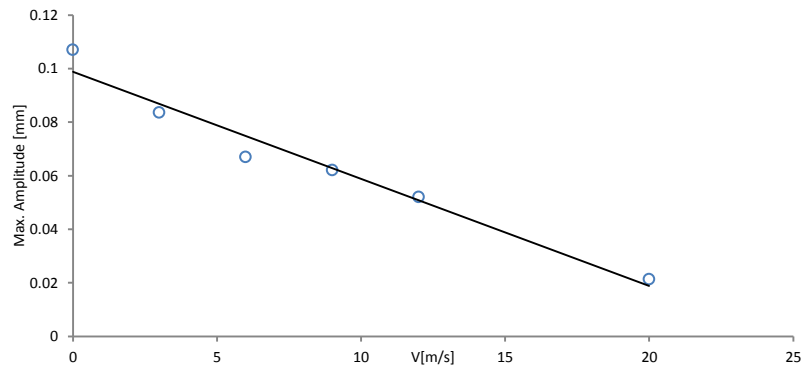


Fig. 5-49 Maximum amplitude of blade oscillation for different fluid velocities

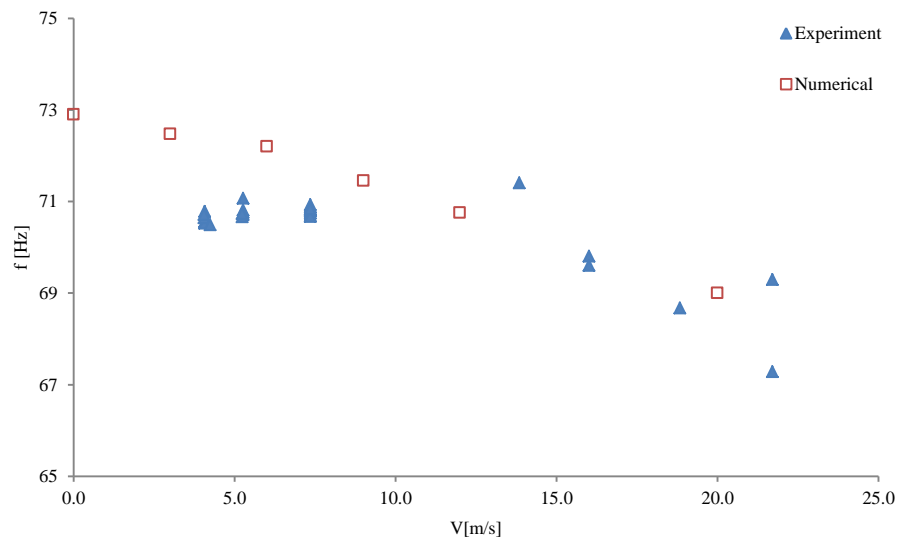


Fig. 5-50 Natural frequency of blade for different fluid velocities

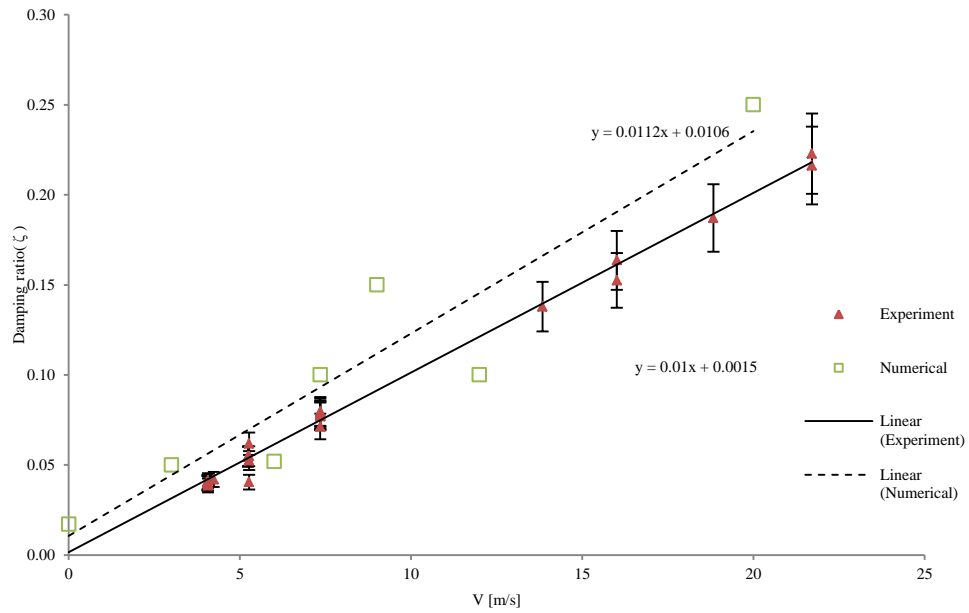


Fig. 5-51 Damping ratio of the blade (ξ) for different fluid velocities ranging from 0 to 25 m/s. The experimental results are taken from (Seeley et al., 2012)

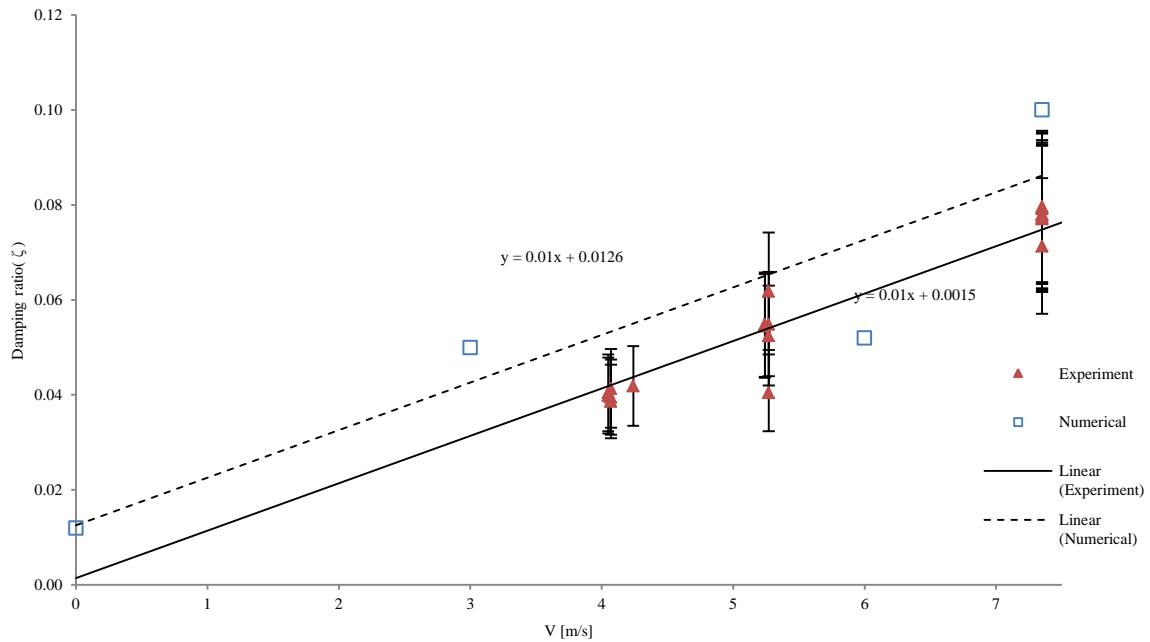


Fig. 5-52 Damping ratio of the blade (ξ) for fluid velocities ranging from 0 to 7.5 m/s. The experimental results are taken from (Seeley et al., 2012)

The variations of damping ratio for different fluid velocities ranging from 0 to 25 m/s and 0 to 7.5 m/s are plotted in Fig. 5-51 and Fig. 5-52, respectively. The following conclusions can be summarized from our investigations done in this thesis:

- ✓ The effects of considering different types of applied forces on the hydraulic blade were studied in section 5.3.2. We considered three types of forces including a step force, a periodic force and an increasing force. We found that the response of the system to the step force depends strongly on the duration of the force application. However, we need to know the fundamental period of the system if we want the system to be excited in its first fundamental frequency under the periodic force application. Our observations also showed that the response of the system is less sensitive to the duration of the force application when we use an increasing force function. These observations convinced us to use the increasing force function in our foregoing analysis in studying the influence of other parameters.
- ✓ To study the effects of using different meshes and to prevent any misalignment on the common interface of the fluid-structure problem, we studied three mesh sizes for the fluid domain along with two mesh sizes for the structural domain. It should also be noted that the fluid elements around the blade structure are very important in solving a FSI problem
- ✓ We found that selection of mesh sizes depends strongly on the time steps used in the calculations. Smaller time steps need finer fluid meshes.
- ✓ Higher velocities need finer fluid meshes. The results of our analysis with fluid fine meshes showed good agreement with those obtained from the experiment for inlet velocities less than or equal 7 m/s.
- ✓ For inlet velocity more than 4m/s we could capture von Kármán vortices by using fine meshes and small time steps.
- ✓ Calculated values of damping ratio for the blade by using the results of the FSI analysis for the velocities ranging from 0 to 7.5 m/s are in better agreement with those from the experiment when compared with the calculations based on the velocities ranging from 0 to 25 m/s. This indicates higher confidence in our FSI analysis for lower velocities. It should be noted here that as we mentioned earlier in section 5.3.3, FSI analysis of the hydrofoil blade with higher velocities requires a finer fluid mesh.

- ✓ The presence of higher modes of vibrations in the FSI analysis of the problem with higher fluid velocities can also be considered as another source of discrepancies between the experimental values and the calculated ones obtained from the FSI analysis. As we explained earlier, when we use the results of the FSI analysis with higher fluid velocities, the results contain higher modes of vibrations and the effects of damping due to the first and second modes of vibrations are included in the analysis whereas the damping ratio has been obtained by exciting the first mode of vibration in the experiment. This is mentioned as “The main objective of the tests was to obtain the experimental frequency response function near the first mode of vibration, then to determine the natural frequency and damping from the character of the experimental frequency response function” in (Seeley et al., 2012).
- ✓ In the experimental test, Macro-fiber Composite (MFC) piezoelectric actuators were bonded to a plate, placed in a test section and subjected to flowing water at increasing velocities. Manufacturing tolerances and the effect of MFC on increasing the thickness of the hydrofoil blade might also be considered as possible sources of discrepancy with the experiment.
- ✓ Our experience in using ANSYS for FSI analysis of hydrofoil blades indicates that more attention must be given to the convergence of the iterations on the interface loads. For more detail you can see Appendix A.
- ✓ The maximum amplitude of the blade vibration decreases when the fluid velocity is increased.
- ✓ The response frequency of the blade decrease with the increasing of the fluid velocity.
- ✓ There is a linear relationship between the damping ratio and the fluid velocity. This conclusion is in agreement with the results reported by Seeley et al. (2012) from the experimental observations.

CHAPTER 6 CONCLUSIONS

The aim of this research was to investigate the coupled effects of flowing fluid and a simplified hydrofoil blade by using a two-way fluid-structure interaction modeling of hydrofoil. The capability of two-way fluid-structure interaction modeling available in the commercial software ANSYS was used in this analysis. In particular and due to the practical importance, special attention was paid to damping due to FSI in realistic flowing water conditions. The geometry of the blade was selected to be similar with the hydrofoil blade used in the experimental investigation available in the literature. The damping coefficient of the blade was estimated from the damped free vibration response of the blade using logarithmic decrement method. The problem was solved for different types of numerical meshes to study the influences of mesh size on the convergence of the solution procedure. Our experience showed that the proposed two-way FSI analysis of the problem was more sensitive to the meshes used in the fluid domain and more attention must be paid in creating the appropriate meshes in the fluid domain of the problem. Moreover, the appropriate mesh size for the problem depends on the velocity of the fluid. We found in our analysis that finer meshes must be used for higher velocities, as expected. Another important parameter in the FSI solution is the value of the time step. Our analysis showed that small time steps must be used to obtain a better agreement with the experimental results. However, smaller time steps require finer meshes which in turn increase the calculation time. It is therefore necessary to use an optimum combination of mesh size and time step to make the two-way FSI solution computationally efficient.

For a better understanding of the influence of considering FSI in the analysis of dynamic behavior of the hydrofoil blade and to see if such complicated analysis is actually required from the practical point of view, we also compared the results of a transient analysis of the hydrofoil blade including FSI with those obtained from the analysis of the same problem when the blade structure is assumed rigid and the FSI effects are ignored. It was found that the fluid forces on the hydrofoil blade evaluated by the FSI analysis were considerably less than those estimated when the interaction of the fluid structure was ignored. However, we obtained the same frequency for the fluctuating fluid forces in both analyses. This result indicates that considering FSI in predicting the frequency of the fluctuating fluid forces in practical problems might be less

important if the main concern of the analyzer is to check the possibility of the resonance (lock-in). We concluded that the FSI must be included in the modeling when we aim to predict the influences of the fluid on the damping behaviour in the blade vibration. In terms of the computational time, we found that running our FSI modeling took approximately 35 hours (with 4 CPU working in parallel) which was considerably higher than 5 hours which was the time required for the analysis of the problem when the interaction between the fluid and the hydrofoil blade was ignored. We also found that the presence of fluid in the vicinity of the hydrofoil blade has the effect of reducing the natural frequency of the blade. In our problem, the natural frequency of the blade-fluid system was approximately one third of that for the dry-blade. This frequency was also decreased with increasing fluid velocity. Moreover, we found that the maximum amplitude of blade deformation in water was considerably less than the blade deformation ignoring the fluid effects. The maximum amplitude of the vibration was also decreased when the fluid velocity was increased. As a general conclusion, we found a linear relationship between the damping ratio and the fluid velocity. This conclusion was in agreement with the results reported by Seeley et al. (2012) from the experimental observations.

From the practical point of view, our experience in using ANSYS for FSI analysis of hydrofoil blades indicated that more attention must be given to properly initialization of different analysis parameters before starting the solution. Using the default initialization parameters as recommended by ANSYS may leads to inappropriate numerical results without any warning and/or errors.

It should also be mentioned here that the hydrodynamic damping influences the amplitude of vibrations and is directly related to fatigue problems in hydraulic machines which are of great importance in their design procedure. Therefore, the results of the present study in identification of hydrodynamic damping are crucial for constructors and can be used to assess the dynamics of runners in hydropower turbines at the earliest stage of the design phase.

REFERENCES

- Bathe, K.J., 1996. Finite Element Procedure. Prentice Hall, New Jersey.
- Boyce, 2001. Elementary Differential Equations (Boyce & DiPrima 7Th Edition)
- Coutu, A., Aunemo, H., Badding, B. and Velagandula, O., 2005. Dynamic Behaviour of High Head Francis Turbines, Hydro 2005, Villach, Austria.
- Coutu, A., Monette, C. and Velagandula, O., 2007. Francis Runner Dynamic Stress Calculations, Hydro 2007, Granada, Spain.
- Coutu, A., Proulx, D., Coulson, S. and Demers, A., 2004. Dynamic assessment of hydraulic turbines-high head Francis, Hydrovision, Montréal.
- Coutu, A., Velagandula, O., Nennemann, B., 2005. Francis Runner Forced Response Technology, Waterpower XIV, Austin, TX.
- Dompierre, F. and Sabourin, M., 2010. Determination of turbine runner dynamic behaviour under operating condition by a two-way staggered fluid-structure interaction method, 25th IAHR Symposium on Hydraulic Machinery and Systems, September 20, 2010 - September 24, 2010. IOP Conference Series: Earth and Environmental Science. Institute of Physics Publishing, Timisoara, Romania.
- Du, J., He, S. and Wang, X., 1998. Dynamic analysis of hydraulic turbine runner and blade system (2). Analysis of examples. Qinghua Daxue Xuebao/Journal of Tsinghua University, 38(8): 72-75.
- Dubas, M. and Schuch, M., 1987. Static and dynamic calculation of a Francis turbine runner with some remarks on accuracy. Comput Struct, 27(5): 645-655.
- Esmailzadeh, M., Lakis, A., Thomas, M. and Marcouiller, L., 2008. Three-dimensional modeling of curved structures containing and/or submerged in fluid. Finite Elements in Analysis and Design, 44(6-7): 334-345.
- Glück, M., Breuer, M., Durst, F., Halfmann, A. and Rank, E., 2001. Computation of fluid-structure interaction on lightweight structures. Journal of Wind Engineering and Industrial Aerodynamics, 89(14-15): 1351-1368.
- Großmann, D., Jüttler, B., Schlusnus, H., Barner, J. and Vuong, A.-V., 2012. Isogeometric simulation of turbine blades for aircraft engines. Computer Aided Geometric Design, 29(7): 519-531.

- Hutchison, S.R., 2012. Numerical Modelling of Hydrofoil Fluid-Structure Interaction, University of Tasmania.
- Kelly, 2012. Mechanical Vibrations: Theory and Applications. Global Engineering: Christopher M. Shortt.
- Khalid, S.-s., Zhang, L., Zhang, X.-w. and Sun, K., 2013. Three-dimensional numerical simulation of a vertical axis tidal turbine using the two-way fluid structure interaction approach. *J. Zhejiang Univ. Sci. A*, 14(8): 574-582.
- Kim, H.-J. and Youn, S.-K., 2012. Spline-based meshfree method. *International Journal for Numerical Methods in Engineering*: n/a-n/a.
- Lee, Y.H., Huai, W.X., Zheng, B. and Qian, Z.D., 2010. Analysis of pressure oscillations in a Francis hydraulic turbine with misaligned guide vanes. *Proceedings of the Institution of Mechanical Engineers, Part A: Journal of Power and Energy*, 224(1): 139-152.
- Monette, C., Coutu, A. and Velagandula, O., 2007. Francis Runner Natural Frequency and Mode Shape Predictions, *Waterpower XV*, Chattanooga TN, USA
- Münch, C., Ausoni, P., Braun, O., Farhat, M. and Avellan, F., 2010. Fluid–structure coupling for an oscillating hydrofoil. *J Fluid Struct*, 26(6): 1018-1033.
- Namkoong, K., Choi, H.G. and Yoo, J.Y., 2005. Computation of dynamic fluid–structure interaction in two-dimensional laminar flows using combined formulation. *J Fluid Struct*, 20(1): 51-69.
- Naudascher, E. and Rockwell, D., 1980. Oscillator-Model Approach To The identification And Assessment Offlow-Induced Vibrations In A System. *Journal of Hydraulic Research*, 18(1): 59-82.
- Rao, S.S., 2011. *The Finite Element Method in Engineering* Butterworth–Heinemann.
- Reese, M.C., 2010. *Vibration and Damping of Hydrofoils in Uniform Flow*, The Pennsylvania State University.
- Rodriguez, C.G., Egusquiza, E., Escaler, X., Liang, Q.W. and Avellan, F., 2006. Experimental investigation of added mass effects on a Francis turbine runner in still water. *J Fluid Struct*, 22(5): 699-712.
- Saeed, R.A., Galybin, A.N. and Popov, V., 2010. Modelling of flow-induced stresses in a Francis turbine runner. *Adv Eng Softw*, 41(12): 1245-1255.

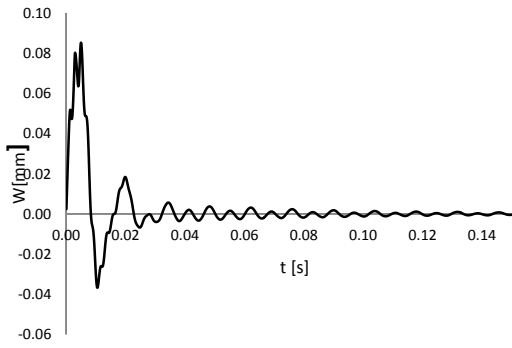
- Schmucker, H., Flemming, F. and Coulson, S., 2010. Two-way coupled fluid structure interaction simulation of a propeller turbine. IOP Conference Series: Earth and Environmental Science, 12(1): 012011.
- Seeley, C., Coutu, A., Monette, C., Nennemann, B. and Marmont, H., 2012. Characterization of hydrofoil damping due to fluid–structure interaction using piezocomposite actuators. Smart Materials and Structures, 21(3): 035027.
- Silva, C.W., 2000. Vibration: Fundamentals and Practice. CRC Press LLC.
- Tanaka, H., 1990. Vibration behavior and dynamic stress of runners of very high head reversible pump-turbines, 15th IAHR Symposium, Belgrade.
- Thapa, B.S., Panthee, A. and Thapa, B., 2012. Computational Methods in Research of Hydraulic Turbines Operating In Challenging Environments. International Journal of Advanced Renewable Energy Research, 1(2): 1-4.
- Wang, W.Q., He, X.Q., Zhang, L.X., Liew, K.M. and Guo, Y., 2009. Strongly coupled simulation of fluid-structure interaction in a Francis hydroturbine. Int J Numer Meth Fl, 60(5): 515-538.
- Wang, X., 2008. Fundamentals of Fluid-Solid Interactions: Analytical and Computational Approaches. Monograph Series on Nonlinear Science and Complexity. Elsevier, Netherland.

APPENDIX

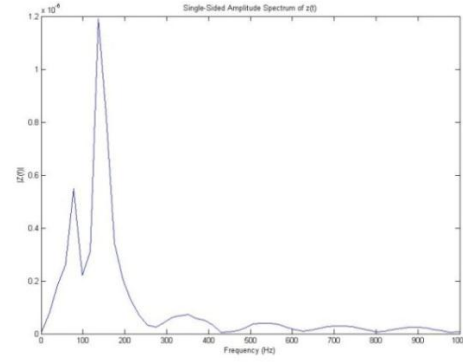
Appendix A: Notes on using ANSYS for FSI analysis

Our experience in using ANSYS for FSI analysis of hydrofoil blades indicates that more attention must be given to the convergence of the iterations on the interface loads. The default number of coupling iterations in the program is 10. However, it can be changed by user in the solver control. The risk of using the default number of coupling iterations (as recommended by ANSYS) is to get inappropriate numerical results without any warning and/or errors. In such cases, the program continues to run with no error and/or warning messages whereas the required convergence on the interface loads in each time step has not been reached because of insufficient number of coupling iterations. In turn, we will have numerical results from the program which seem to be correct but are not physically correct at all!

To explain this situation, we have already considered the influence of force application in section 5.3.2. In the case of using unit step force and with $t_f = 1 \times 10^{-3}$ s, if we leave the default value of number of coupling iteration (10) we get the z -displacement at midpoint of the trailing edge of the blade and FFT of the system response as given in Fig. 0-1. As can be seen from this figure, power spectral densities of the vibration amplitudes obtained by FFT analysis shows two dominant frequencies 73.2 Hz and 141.3 Hz which are close to the first two natural frequencies of the blade, respectively. However, if we look at the convergence of the interface loads (as shown in Fig. 0-2(a)), it is seen that the interface loads have not been converged with the default number of coupling iterations. Our experience showed that more than 30 number of iteration is needed to reach convergence in this case (as shown in Fig. 0-2(b)). Fig. 0-3 shows the z -displacement at midpoint of the trailing edge of the blade and FFT of the system response with the same unit step force and with 40 coupling iterations. This figure shows only one dominant frequency 73.1 Hz which is in contrast with two dominant frequencies 73.2 Hz and 141.3 Hz as we have already seen in Fig. 0-1.

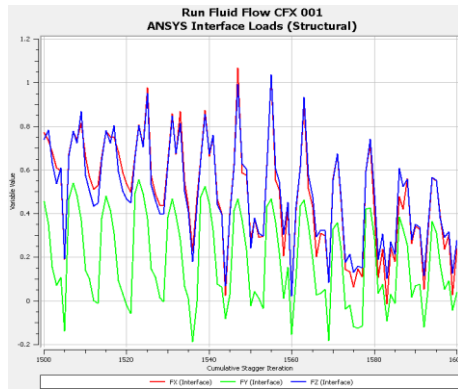


(a)

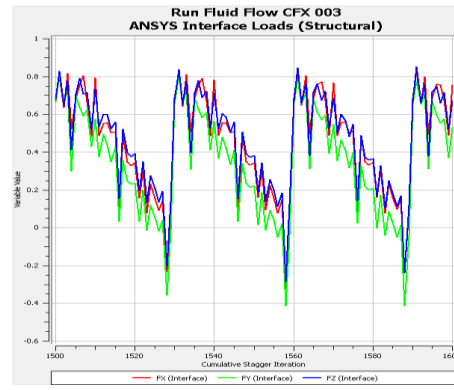


(b)

Fig. 0-1 (a) z -displacement at midpoint of the trailing edge of the blade (b) FFT of the system response for $t_f = 1 \times 10^{-3}$ sec

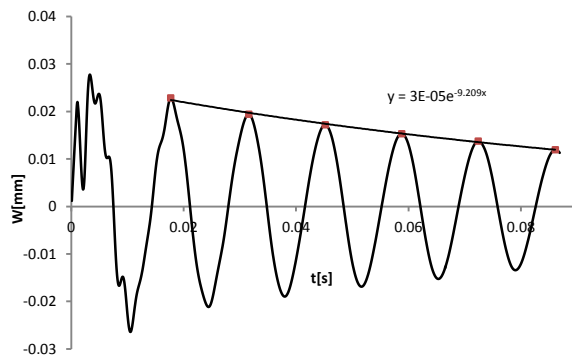


(a)

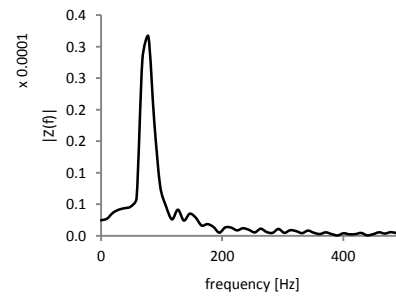


(b)

Fig. 0-2 ANSYS interface loads



(a)



(b)

Fig. 0-3(a) z -displacement at midpoint of the trailing edge of the blade (b) FFT of the system response for $t_f = 1 \times 10^{-3}$ sec